ABSTRACT

Title of Dissertation: SIMULATED DUST AEROSOL LIFECYCLE IN THE NASA GEOS-5 ATMOSPHERIC TRANSPORT MODEL AND SENSITIVITY TO SOURCE AND SINK MECHANISMS

Edward Paul Nowottnick, Ph.D., 2011

Directed By: Zhanqing Li
Department of Atmospheric and Oceanic Science

Understanding interactions of mineral dust aerosols with the Earth system remains a key uncertainty in assessing global climate change. A significant portion of this uncertainty arises due to an incomplete understanding of the source, transport, and loss processes that control the dust aerosol lifecycle.

Global aerosol transport models compliment traditional observational platforms to serve as useful tools for exploring aerosol-Earth system interactions. However, global models are limited by scale, requiring parameterizations to represent the lifecycle of dust. Here, the simulated dust lifecycle is explored in versions 4 and 5 of the NASA Goddard Earth Observing System (GEOS-4/5) model.

Different treatments of the mobilizing physics are first explored by considering two mobilization schemes in GEOS-4. Both schemes produced similar distributions of aerosol optical thickness (AOT) and extinction that become more comparable with observations downwind of the source region. Despite similarities in the optical comparisons, the schemes differ in mass loadings owing to differences in emitted particle

size distributions, suggesting that emission scheme choice is significant for mass budgets and particle size distributions.

The effect of spatial resolution on source processes was investigated in GEOS-5. Model spatial resolution had a significant impact on simulated dust distributions, as increased model spatial resolution resolves higher wind speeds used to parameterize dust emissions. Model spatial resolution had regional implications, as simulated dust distribution exhibited the greatest sensitivity over the Asian source region. The incorporation of sub-grid wind variability in a coarse resolution simulation led to improved agreement with observed AOT magnitude, but did not improve the timing of simulated dust events over the Asian source region.

GEOS-5 was used to investigate the cause of an observed barrier to dust transport across Central America into the Pacific. The baseline simulation did not develop as strong of a barrier when compared to observations. Better agreement was obtained when the parameterization for wet removal was treated as other hydrophilic aerosols. Analysis of the dust transport dynamics and loss processes suggest that while both mechanisms play a role in defining the barrier, loss processes by wet removal are about twice as important as transport.

SIMULATED DUST AEROSOL LIFECYCLE IN THE NASA GEOS-5 ATMOSPHERIC TRANSPORT MODEL AND SENSITIVITY TO SOURCE AND SINK MECHANISMS

by

Edward Paul Nowottnick

Dissertation submitted to the Faculty of the Graduate School of the
University of Maryland, College Park in partial fulfillment
of the requirements for the degree of
Doctor of Philosophy
2011

Advisory Committee:

Professor Zhanqing Li, Chair
Adjunct Professor Peter Colarco
Professor Robert Hudson
Professor Rachel Pinker
Professor Karen Prestegaard, Dean's Representative

Preface

The focus of this dissertation is on investigating the processes that influence dust distributions in the Earth system using the NASA GEOS modeling system: *sources*, *transport*, and *losses*. This dissertation is organized in six chapters. The first chapter outlines the current understanding and importance of mineral dust aerosol interactions with the Earth system and discusses the need for investigation into the processes that influence the dust aerosol life cycle in a global aerosol transport model. Chapter 2 presents the NASA GEOS modeling system and datasets used to evaluate simulated dust distributions. Chapter 3 discusses the physics of dust source and loss processes on Earth and how the equivalent processes are parameterized in the NASA GEOS modeling system. Chapter 4 is focused on source processes; particularly how mobilization parameterizations and model spatial resolution influence simulated dust distributions. Chapter 5 investigates dust transport and loss processes, and uses the NASA GEOS modeling system to explore the Central American dust barrier. Chapter 6 outlines future work to be carried out as part of a post-doc appointment.

The first half of Chapter 4 was published in the *Journal of Geophysical Research – Atmospheres* in 2010. The second half of Chapter 4 is currently in preparation for submission to a peer-reviewed journal. Chapter 5 has been accepted by *Atmospheric Chemistry and Physics* and is currently in the production process.

Dedication

To my mother, who always pushed education and to my father, who taught me to work hard in life.

Acknowledgements

Thank you to: Kelly, for her support over the past 10 years, particularly during the past few months. I eagerly await the "honey-do" list that I've accumulated since March. Mom and Dad, for encouragement and providing me with the means to do anything that I wanted to do in life. David, Michael, and Mary for their distractions. Me-Me for her advice and support. Pete and Prof. Li for giving me with the opportunity and tools to pursue my interests while providing constructive criticism along the way.

Table of Contents

List of Tables

List of Figures

List of Abbreviations

AEJ – African Easterly Jet
AEW –African Easterly Wave
AERONET – Aerosol Robotic Network
AGCM – Atmospheric General Circulation Model
AI – Aerosol Index
AOT – Aerosol Optical Thickness
APS – Aerodynamic Particle Sizer
ARM –Atmospheric Radiation Measurement
AVHRR – Advanced Very High Resolution Radiometer
CALIOP – Cloud-Aerosol Lidar with Orthogonal Polarization
CALIPSO – Cloud-Aerosol Lidar and Infrared Pathfinder Satellite Observations
CCM3 – Community climate model, Version 3
CCN – Cloud Condensation Nuclei
CERES – Cloud and the Earth's Radiant Energy System
CLM2 – Community Land Model, Version 2
CLSM – Catchment Land Surface Model
COMMIT – Chemical, Optical, and Micro-Physical Measurements of *In Situ* Troposphere
CPL – Cloud Physics Lidar
CTM – Chemical Transport Model
DAS – Data Assimilation System
DEAD – Dust Entrainment and Deposition
ECMWF – European Center for Medium-Range Weather Forecasts
GADS – Global Aerosol Data Set
GEOS-4 – Goddard Earth Observing System Model, version 4
GEOS-5 – Goddard Earth Observing System Model, version 5
GMAO – Goddard Modeling and Assimilation System
GSFC – Goddard Space Flight Center
GOCART – Goddard Chemistry, Aerosol, Radiation, and Transport Model
GPCP – Global Precipitation Climatology Project
ITCZ – Inter-Tropical Convergence Zone
LARGE – Langley Aerosol Research Group Experiment
LASE – Lidar Atmospheric Sensing Experiment
MERRA – Modern Era Retrospective Analysis for Research and Applications
MISR – Multi-angle Imaging Spectroradiometer
MODIS – Moderate Resolution Imaging Spectroradiometer
NAMMA – NASA African Monsoon Multidisciplinary Analyses
NASA – National Aeronautics and Space Administration
NCAR – National Center for Atmospheric Research
OMI – Ozone Monitoring Instrument
PDF –Probability Density Function
P – L – Production Minus Loss
PRIDE – Puerto Rico Dust Experiment

QA – Quality Assurance
SAL – Saharan Air Layer
SMART – Surface-Sensing Measurements and Atmospheric Radiative Transfer
SSA – Single Scattering Albedo
SSM/I – Special Sensor Microwave Imager
TC^4 – Tropical Composition Cloud and Climate Coupling
TOMS – Total Ozone Mapping Spectrometer
UHSAS – Ultra High Sensitivity Aerosol Spectrometer
UV – Ultraviolet

List of Symbols

α - Angstrom parameter
β_{523nm} – total attenuated backscatter at 532 nm
β_{1064nm} – total attenuated backscatter at 1064 nm
β_{ls} – large-scale precipitation duration
$\beta_{perpendicular}$ – perpendicular component to the total attenuated backscatter for a particular wavelength
$\beta_{parallel}$ – parallel component to the total attenuated backscatter for a particular wavelength
χ - dust mass flux velocity potential
C, C′ – tuning constant
C_{cunn} – Cunningham slip correction factor
c – size parameter for Weibull distribution
D – dust/soil particle diameter
F – emitted dust mass flux
F_u – convective updraft mass flux
f_{ls} – fraction of large-scale precipitating clouds within a grid box
$fwet_{conv}$ - scavenging efficiency for dust removal by convective precipitation
$fwet_{ls}$ – scavenging efficiency for dust removal by large-scale precipitation
γ - dust mass mixing ratio
Γ - Gamma function
g – acceleration due to gravity
k – shape parameter for Weibull distribution
λ - wavelength [nm]
L – dust mass flux from loss
μ - viscosity of air
Ψ - dust mass flux streamfunction
P – dust mass flux from production
p – atmospheric pressure
Q – dust mass flux
Q_{div} – divergent component of dust mass flux
Q_{rot} – rotational component of dust mass flux
q – column dust loading
ρ_a – density of air
ρ_p – dust/soil particle density
R^2 – correlation of determination
r – particle radius
r_a – aerodynamic resistance
r_b – sublayer resistance
r_s – surface resistance
S – source function
s, s′ – source fraction
τ - aerosol optical thickness
τ_{life} – aerosol lifetime

t –time
U – surface wind speed
U_t – threshold wind speed for dust emission for GOCART based emissions
U_{10m} – 10-meter wind speed
u – east-west component of wind field
u_* - surface friction speed
u_{*t} – threshold wind speed for dust emission for DEAD based emissions
v – north-south component of wind field
v_s – Sedimentation velocity
v_d – turbulent deposition velocity
w – gravimetric soil moisture

Chapter 1: Introduction

1.1 Background

Aerosols refer to particulate matter that has been suspended in the atmosphere and is of natural or anthropogenic origin. Natural aerosols refer to those inherent to the Earth system (e.g. dust, sea salt) and are typically entrained into the atmosphere by near-surface winds, while anthropogenic aerosols (e.g. sulfates, smokes) are associated with human activity (e.g. combustion). Individual species of aerosol are characterized by unique sources, physical properties, and lifecycles. Additionally, aerosols have atmospheric residence times that are on the order of weeks to months, generally much shorter that atmospheric trace gases. For these reasons, aerosols exhibit *heterogeneous* spatial and temporal distributions within the atmosphere. Aerosols can interact with the Earth system in a variety of pathways: absorption and scattering of light, modifying cloud properties and precipitation, influencing regional air quality, or serving as a nutrient source for ecosystems. In additional to variability in the distribution of aerosols in the atmosphere, the current lack of understanding of these interactions introduces many uncertainties in quantifying the role of aerosols in the Earth climate system. For this reason, the current understanding of the effects of aerosols on the Earth's climate remains low (Figure 1.1).

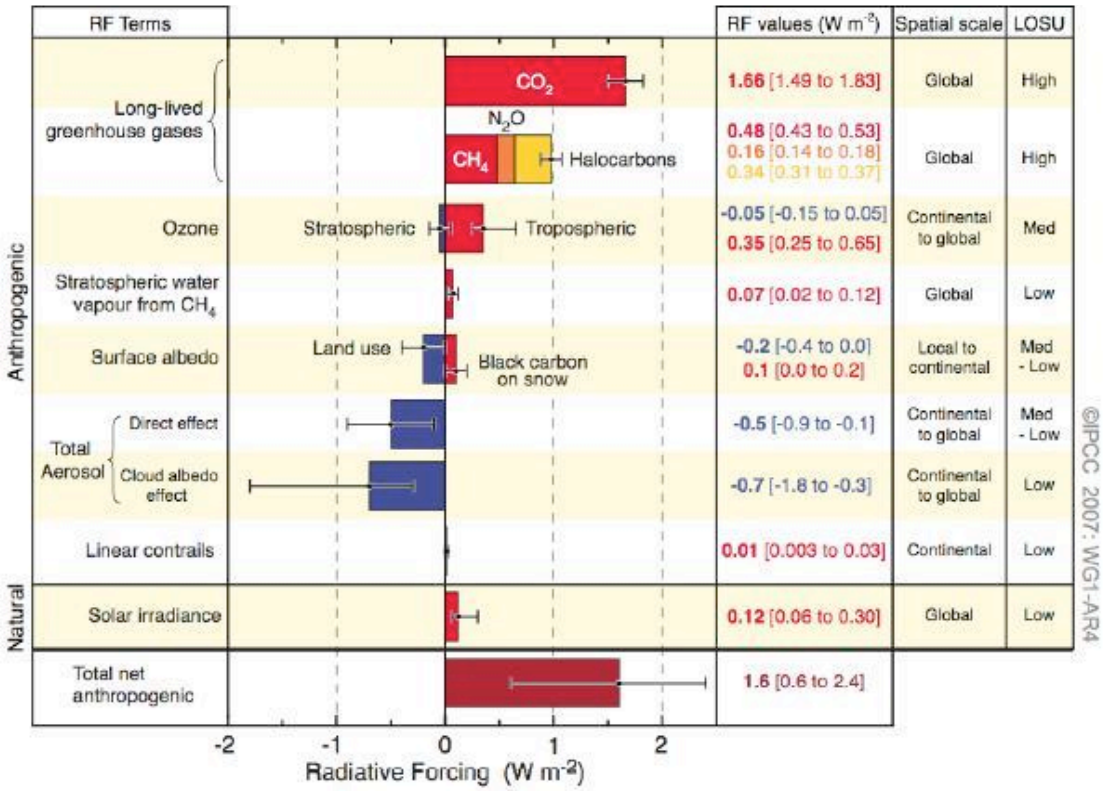

Figure 1.1. Global average radiative forcing estimates and uncertainty ranges relative to the pre-industrial climate. Image courtesy of the IPCC Fourth Assessment [Alley et al., 2007].

Natural aerosols that originate from the Earth's soil are known as mineral dust aerosols. On average, it is estimated that 1,000 – 3,000 Tg of dust is emitted annually from the Earth's soil [Huneeus et al., 2010], predominantly from the major desert regions of the world. Two of the world's largest sources of dust aerosols are the Saharan desert in North Africa and the Taklamakan and Gobi deserts in northern China. Dust events from these regions can span hundreds of kilometers (Figure 1.2) and can be transported long distances, having implications for local air quality. While the emission of dust is primarily of natural origin, human activities, such as cattle grazing and desertification resulting from improper agricultural practices, is thought to contribute less than 10% of the atmospheric dust load [Tegen et al., 2004]. However, the anthropogenic contribution

to the total dust loading is expected to change depending on future climate scenarios [Mahowald et al., 2003].

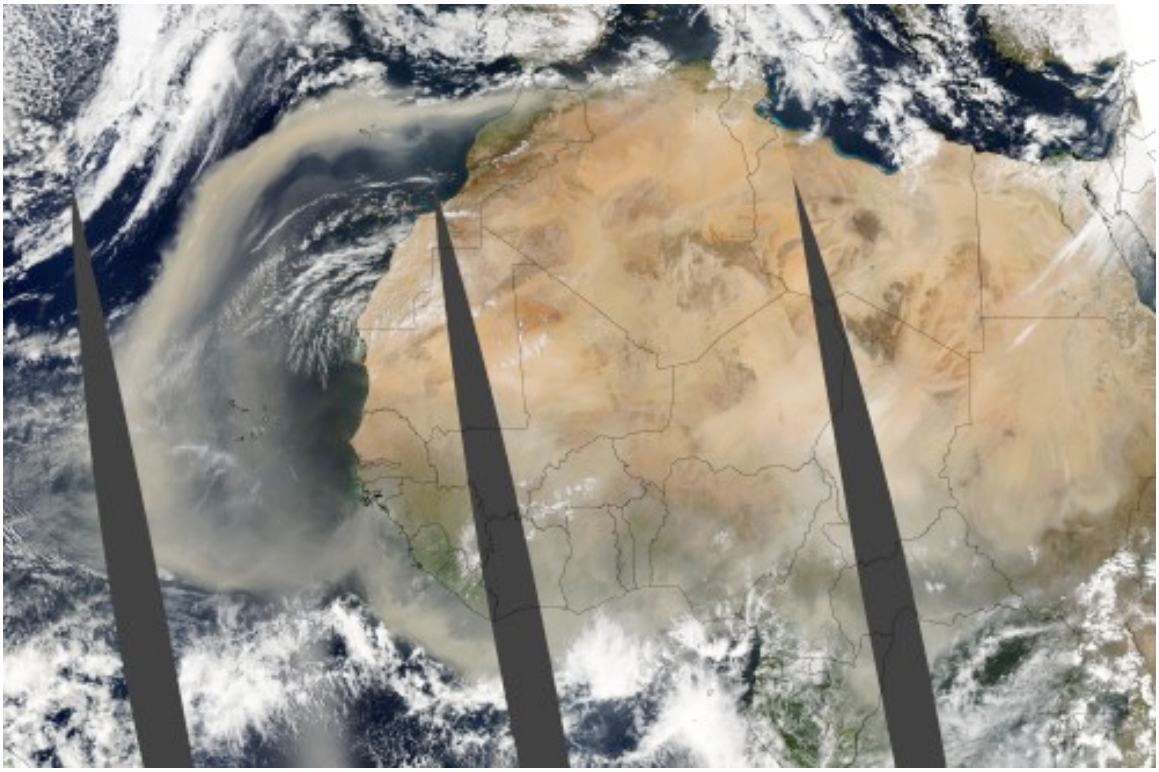

Figure 1.2. A dust event transported from the Saharan source region on March 11, 2004. Image was taken using the NASA MODIS-Aqua sensor.

Once suspended in the atmosphere, dust is known to interact with the Earth system. Dust aerosols directly influence the Earth's radiation budget through the scattering and absorption of light [Haywood et al., 2003; Sokolik and Toon, 1996]. Specifically, a suspended dust layer can act as an effective Earth surface, acting to absorb solar radiation, potentially causing a local warming as large as 10 W m^{-2} within the dust layer [Sokolik and Toon, 1996]. Absorption by dust within the atmosphere acts to reduce the available incident solar radiation at the Earth's surface, leading to a net cooling up to –60 W m^{-2} at the surface [Zhu et al., 2007; Tegen and Miller, 1998; Sokolik and Toon,

1996]. Locally, the net radiative forcing of dust can be comparable to clouds [Sokolik and Toon, 1996].

Koretsky et al., [1997] and Twohy et al., [2009] showed that dust aerosols readily attract water while suspended in the atmosphere. Therefore, dust aerosols can indirectly influence the atmosphere by serving as cloud condensation nuclei (CCN) [Kumar et al., 2007; Rosenfeld et al., 2001] and ice nuclei [DeMott et al., 2003], modifying the lifetimes of both the aerosols and clouds and the onset, duration, and location of precipitation [Yoshioka et al., 2007]. Specifically, dust serving as CCN has been shown to reduce the average cloud droplet size, reducing precipitation [Rosenfeld et al., 2001]. Furthermore, Jenkins [2008] showed that under unstable atmospheric conditions, the presence of dust aerosols could act to invigorate precipitation as ice nuclei.

The radiative effects of dust have been shown to influence the general circulation [Miller at al., 2004] and there has been a recent interest in understanding the effects of dust aerosols on tropical cyclogenesis. Over the tropical North Atlantic Ocean, dust is thought to reduce sea surface temperatures through the absorption of short wave radiation [Lau and Kim, 2007], creating a heating dipole with warming aloft and cooling below [Reale et al., 2009] acting to reduce available energy for cyclogenesis [Lau and Kim, 2007]. Additionally, absorption by dust aerosols is thought to modulate tropical cyclogenesis by increasing upper level wind shear during development [Dunion and Velden, 2004].

Dust aerosols have implications for biogeochemical cycling. Chemically, dust aerosols are comprised of both soluble and insoluble forms of iron. While the iron in dust aerosols is primarily insoluble, photochemical and cloud processing can convert it

into a soluble form [Hand et al., 2004; Kieber et al., 2003; Desbouefs et al., 2001; Zhu et al., 1997]. This is significant for biogeochemical considerations, as soluble iron in dust aerosols serves as a nutrient source for aquatic and terrestrial ecosystems, therefore influencing the carbon cycle [Mahowald et al., 2005; Jickells et al., 2005; Falkowski et al., 2003].

It is clear that dust has a significant role within the Earth System. However, despite the current level of understanding of the interactions between dust and the Earth System, the understanding of many of the interactions is incomplete. Therefore, mineral dust aerosols remain a key source of uncertainty in assessing the impact of aerosols on climate change [Alley et al., 2007].

1.2 Statement of the Problem

Traditionally, understanding the interactions of aerosols with the Earth system requires combining observational platforms with global modeling efforts. In general, observations are used to constrain aerosol distributions in global aerosol transport models, which are in turn used to simulate complex aerosol – Earth system interactions. Used this way, global aerosol transport models can serve as powerful tools for understanding aerosol – Earth system interactions. One advantage of global aerosol transport models is that they offer high spatio-temporal coverage. As an example, satellite observations of aerosols are frequently limited by sampling frequency and contamination from other phenomena (e.g. clouds or sun glint) that obstruct observations of aerosol. Global aerosol transport models can often compliment observations where data is missing. Additionally, processes are separable in way that an individual aerosols

contribution to a simulated quantity or phenomena can easily be determined. Conversely, quantifying the effects of an individual aerosol type using only satellite observations may be difficult, as isolating the effects from other aerosol types and clouds may be challenging. In practice, observational techniques are required to infer the effects from individual aerosol type. Similarly, processes can be explicitly modified within a global aerosol transport model. This is particularly useful for quantifying the effects of a specific process on simulated aerosol distributions (i.e. sensitivity studies).

However, global aerosol transport models are limited by how well the atmospheric and aerosol processes are represented in the model. A consistent limitation across all global models is that the *scale* of the model grid is typically significantly larger than the scale of the aerosol physics, requiring parameterizations to determine simulated distributions. These parameterizations may exhibit sensitivity to characteristics of the model, such as driving meteorology, model spatial resolution or and underlying physics (ex. convection), therefore having implications for the simulated dust aerosol lifecycle.

The central problem to be addressed in this thesis is understanding how the treatment of dust source, transport, and loss processes influence the dust aerosol lifecycle in a global aerosol transport model. More specifically, these processes will be explored in terms of their influence on the atmospheric dust loading. The current lack of understanding of processes associated with the dust aerosol lifecycle serves as a limiting factor in furthering our understanding of aerosol-Earth system interactions [Zender et al., 2004]. Therefore, using a global aerosol transport model as a tool, this thesis investigates how source, transport, and loss processes influence the dust aerosol lifecycle.

Specifically, the following scientific questions are addressed as they relate to the simulated dust aerosol lifecycle:

1. What are the impacts of different treatments of the physics of dust mobilization on simulated dust distributions in a global model?
2. How does model spatial resolution impact the magnitude of dust emissions?
3. Does model spatial resolution have implications for the timing of dust events?
4. How does the resolution of the dust source function impact dust emissions?
5. Are there different regional responses to perturbations to dust source processes?
6. How well does the model reproduce observed dust transport downwind of the source region?
7. What are the roles of dust transport and removal processes in maintaining and establishing the Central American dust barrier?
8. How are these roles influenced by perturbations to wet removal processes?

1.3 Scope of the Problem

While understanding the simulated aerosol lifecycle of all aerosol types is significant, this work provides an in-depth investigation of the simulated aerosol lifecycle specifically for mineral dust aerosols using the NASA Goddard Earth Observing System (GEOS) versions 4 and 5 atmospheric general circulation model (AGCM) and assimilation system.

In particular, efforts will be concentrated on the processes that influence simulated dust distributions: *sources*, *transport*, and *removal*. In addition to

understanding dust aerosol lifecycle sensitivities, a portion of this work highlights the capabilities of a global transport model by exploring the cause of an apparent barrier to dust transport located along the Central American coastline.

Throughout this analysis, several observational datasets are utilized to evaluate model performance and to test perturbations to the processes that influence the simulated dust life cycle. In particular, there is a focus during the time periods of several NASA field campaigns, which when combined with traditional satellite and ground-based observational datasets, form a suite of observations to thoroughly evaluate the timing, magnitude, and spatial distribution of simulated dust events.

Chapter 2: The NASA Goddard Earth Observing System Model and Data Sources

In this section the NASA GEOS modeling system is introduced and descriptions of the various satellite, ground-based, and aircraft observational datasets used to evaluate the performance of the modeling system are provided.

2.1 The Goddard Earth Observing System Model

The GEOS earth system model is an atmospheric general circulation model and data assimilation system developed at the NASA Global Modeling and Assimilation Office (GMAO). The GEOS modeling system contains components for atmospheric circulation and composition (including data assimilation), ocean circulation and biogeochemistry, and land surface processes. The GEOS earth system model serves as a state-of-the-art modeling tool for studying climate variability and change, and provides research quality reanalyses for use by NASA instrument teams and the scientific community. In addition to traditional meteorological parameters (winds, temperatures, etc.) [Reinecker et al., 2008], the GEOS earth system model includes modules representing the atmospheric composition, notably aerosols [Colarco et al., 2010] and includes their radiative impact on the atmosphere.

The GEOS earth system model can run in climate, data assimilation, or replay modes. In climate mode, initial conditions are set and the model provides a forecast for a specified time period. In assimilation mode, the model is run similarly to climate mode, but a meteorological assimilation is performed every 6 h to adjust the model temperature, wind, and pressure fields. For this study, the capability of the GEOS earth system model

to "replay" from a prior data assimilation run is utilized. This functions as a data assimilation run in that the model makes a forecast to the analysis time (typically every six hours). However, rather than performing the data assimilation step at that point, the model dynamical state (winds, pressure, temperature, and specific humidity) is simply replaced by the fields from a previously generated assimilation data set. The replay is similar to how an offline chemical transport model (CTM) operates, where dynamical fields are updated at specified time intervals. In contrast to an offline CTM, which interpolates the assimilated meteorological fields to the current model time step, the meteorology in the replay is generated consistently within the GEOS earth system model between updates from the assimilation.

During the timeframe of this work, the GEOS earth system model evolved from version 4 to version 5. The GEOS version 4 (GEOS-4) AGCM [Bloom et al., 2005] is based on the finite volume dynamical core [Lin, 2004] and contains physical parameterizations based on the National Center for Atmospheric Research (NCAR) Community Climate Model version 3 (CCM3) physics package [Kiehl et al., 1996]. The land model used by GEOS-4 is version 2 of the Community Land Model Version 2 (CLM2) as described by Bonan et al. [2002]. GEOS-4 has the capability to run with horizontal resolution ranging from 4° × 5° (latitude × longitude) to 1° × 1.25° and either 32 or 55 vertical hyrid-eta levels, where the vertical levels are terrain following near the surface and transforms to pressure coordinates near 180 hPa, with a model top at about 80 km. GEOS-4 replay simulations are run from GEOS-DAS CERES analyses [Bloom et al., 2005], available every six hours at 1° × 1.25° spatial resolution.

The release of the GEOS version 5 (GEOS-5) AGCM [Rienecker et al., 2008] offers improved physical parameterizations that treat planetary boundary layer turbulence, clouds and convection, radiation, and gravity wave drag [Reinecker, 2008]. These improvements include replacing the previous convective scheme with a version of Moorthi and Suarez [1992] and radiative transfer model with one that permits aerosol absorption and scattering [Chou and Suarez, 1999], developed at the NASA Goddard Space Flight Center (GSFC) [Reinecker, 2008]. Additionally, the land surface processes in GEOS-5 are treated with the Catchment Land Surface Model (CLSM) [Reinecker, 2008]. GEOS-5 has the capability to run at various horizontal spatial resolutions, from 4° x 5° latitude by longitude for long climate integrations to ~3 x 3 km^2 on 72 vertical hybrid-eta levels, with a model top at about 85 km. GEOS-5 uses the same finite-volume dynamical core [Lin, 2004] as previous incarnations of the model, but offers the cubed-sphere dynamical core [Putman and Lin, 2007] for resolutions higher than 0.5° x 0.625°. For replay simulations, GEOS-5 uses fields form the Modern Era Retrospective Analysis for Research and Applications (MERRA) [Rienecker et al., 2011], available every six hours at a spatial resolution of 0.5° x 0.625°.

The aerosol module in the GEOS-4/5 is a version of the Goddard Chemistry, Aerosol, Radiation, and Transport (GOCART) model [Chin, et al., 2002] that has been modified to run within the GEOS AGCM framework [Colarco et al., 2010]. The aerosol module simulates five non-interacting tropospheric aerosol species: dust, sea salt, black carbon, organic carbon, and sulfate. An in-depth discussion on the treatment of dust in the GEOS earth system model is provided in Chapter 3.

2.2 Data Sources

2.2.1 Satellite Datasets

2.2.1.1 Moderate Resolution Imaging Spectroradiometer

The Moderate Resolution Imaging Spectroradiometer (MODIS) was launched on December 12, 1999 aboard the Terra spacecraft. A second MODIS instrument was launched on the Aqua satellite as a part of the NASA A-Train on May 4, 2002. The MODIS instruments provide multispectral observations of the Earth system using 36 channels, crossing the equator at approximately 10:30 AM (Terra) and 1:30 PM (Aqua) local time. MODIS aerosol retrievals are made at a spatial resolution of at 10 x 10 km^2 using separate retrieval algorithms for ocean and land. Over oceans, the MODIS algorithm uses retrieved radiances from six channels (550, 660, 870, 1240, 1630, and 2130 nm) to provide aerosol information at seven wavelengths, using the six retrieved channels and an additional fitted wavelength at 470 nm [Remer et al., 2005]. Over land, an empirical relationship between radiance retrievals at two visible channels (470 and 660 nm) and one near-IR channel (2130 nm) is used to determine the surface reflectivity to provide aerosols properties at 470, 550, and 660 nm [Remer et al., 2005]. For comparisons to the model, the most recent version (collection 5.1) of the extinction aerosol optical thickness (absorption + scattering) (AOT) at 550 nm is used. MODIS provides semi-quantitative quality assurance (QA) flags, where QA ranges in integer from QA=0 (low confidence in aerosol retrieval) to QA=3 (high confidence in retrieval). Over land only the highest quality (QA=3) retrievals are aggregated, whereas over ocean

all retrievals are aggregated but weight them by their respective QA flag value, similar to the MODIS canonical Level 3 gridded product [Levy et al., 2009].

2.2.1.2 Multi-Angle Imaging Spectroradiometer

The Multi-Angle Imaging Spectroradiometer (MISR) was launched on NASA's Terra satellite on December 18, 1999 [Kahn et al., 2005], providing observations at approximately 10:30 AM local time. MISR contains nine push-broom cameras to observe the same point on Earth from nine different angles (nadir, ±26.1°, ±45.6°, ±60.0°, and ±70.5°) and in four spectral bands (446, 558, 672, and 866 nm). Aerosol retrievals are performed using a look-up table approach with retrievals provided at 17.6 x 17.6 km^2 horizontal resolution, where constraint of angular information from the multiangle viewing geometry is used to characterize the aerosols and also permits retrievals over bright surfaces [Diner et al., 1998; Abdou et al., 2005]. The MISR swath width along the ground is about 360 km, providing global coverage approximately every nine days. MISR Level 2 AOT values from the latest version of the MISR aerosol retrieval algorithm (v. F12_0022) are used at 558 nm.

2.2.1.3 Ozone Monitoring Instrument

The Ozone Monitoring Instrument (OMI) was launched as part of the A-Train onboard Aura on July 15, 2004, providing aerosol retrievals at 354 and 388 nm with a nadir horizontal resolution of 13 x 24 km^2, crossing the equator at approximately 1:30 PM local time [Torres, 2007]. The use of ultraviolet (UV) aerosol retrievals allows OMI to distinguish absorbing dust aerosols from both land and ocean surface, which are both

'dark' at UV wavelengths. Thus, unlike MODIS, OMI is able to provide aerosol retrievals over bright desert surfaces. OMI calculates a qualitative UV aerosol index (AI) at 354 nm using retrievals at 354 and 388 nm. AI values are sensitive to aerosols with a spectrally varying absorbing index of refraction and are positive for absorbing aerosols, such as dust.

2.2.1.4 Cloud-Aerosol Lidar with Orthogonal Polarization

The Cloud-Aerosol Lidar with Orthogonal Polarization (CALIOP) was launched onboard CALIPSO on April 28, 2006 as part of the NASA A-Train. CALIOP is a two-channel (532 and 1064 nm) spaceborne lidar that provides profiles of cloud and aerosol properties along the satellite subpoint [Vaughan, 2005]. CALIOP has a temporal resolution of 20.16 Hz and vertical resolution that varies from 30 m in the troposphere up to 60 m at higher altitudes. Because CALIOP is an active instrument, it provides both a daytime (approximately 1:30 pm local time at the equator) and nighttime (approximately 1:30 am local time at the equator) measurement. CALIOP sends out polarized light at 532 nm and is equipped with sensors that measure the parallel and perpendicular components of the total backscattered signal. The standard CALIOP retrieval provides measurements of total attenuated backscatter at each channel [Vaughan, 2005]. Polarization information and spectral variation of the backscatter is used to infer the presence of aerosols and their type [Vaughan, 2005] In the CALIOP algorithm, backscatter from aerosols is differentiated from clouds by the lidar color ratio (β_{1064nm} / β_{532nm}), where β_{1064nm} and β_{532nm} represent the total attenuated backscatter at 1064 nm and 532 nm, respectively. At visible wavelengths, aerosols exhibit spectral variation while

clouds do not, therefore a lidar color ratio that is approximately one is used to identify clouds [Vaughan, 2005]. Once aerosols are differentiated from clouds, polarization properties can be used to infer aerosol type. Non-spherical aerosols such as dust are depolarizing and contribute to signal return in both the perpendicular and parallel planes. Spherical aerosols are not strongly polarizing and scatter predominantly in the parallel plane. Therefore, a depolarization ratio ($\beta_{perpendicular}$ / $\beta_{parallel}$) can be defined to identify the presence of non-spherical aerosols.

2.2.2 Ground Based Datasets

2.2.2.1 Aerosol Robotic Network

Since 1993, The Aerosol Robotic Network (AERONET) of ground-based network of over 500 sunphotometers have provided measurements of direct solar beam extinction every 15 minutes at 340, 380, 440, 500, 670, 870, and 1020 nm to provide AOT measurements at 440, 670, 870, and 1020 nm with an accuracy of +/-0.015 [Holben et al., 2001]. AERONET utilizes principle plane and almuncantar scans to invert aerosol properties and to determine size information [Dubovik and King, 2000]. To determine the AERONET AOT at 550 nm for comparison to our model, we first determine the 470-870 nm Angstrom parameter α, defined:

$$\tau_1 = \tau_2 \left(\frac{\lambda_1}{\lambda_2} \right)^{-\alpha} \qquad \text{Eq. 2.1}$$

where τ_1 and τ_2 are AERONET AOT values at λ_1 = 470 nm and λ_2 = 870 nm, respectively. Once the Angstrom parameter is determined, we use Equation 2.1 to

determine τ at λ = 550 nm. AERONET version 2, Level 2 cloud-screened and quality-assured daily averaged AOT values [Smirnov et al., 2000] are used to evaluate the GEOS modeling system.

Aircraft and *In Situ* Datasets

2.2.3.1 Langley Aerosol Research Group Experiment

The Langley Aerosol Research Group Experiment (LARGE) provides airborne *in-situ* measurements of aerosol microphysical properties. Particle size distributions are determined using a Droplet Measurement Technologies Ultra High Sensitivity Aerosol Spectrometer (UHSAS) for the 0.1 to 0.7 μm diameter range and a TSI Aerodynamic Particle Sizer (APS) for the 0.7 to 10 μm range [Chen et al., 2010]. The APS mass-based sizes were converted to geometric diameters using the procedures described in Chen et al., 2010. While in air, sampled air is drawn to the instruments through a forward facing, isokinetic inlet probe that is mounted to a window plate just ahead of the aircraft starboard wing. During the NASA African Monsoon Multidisciplinary Analyses (NAMMA) field campaign (August - September, 2006), LARGE flew on the NASA DC-8 aircraft.

2.2.3.2 Lidar Atmospheric Sensing Experiment

The airborne Lidar Atmospheric Sensing Experiment (LASE) measures vertical profiles of aerosol and water vapor at 815 nm [Browell et al., 2005]. LASE measurements of aerosol extinction are retrieved by using the lidar extinction to backscattering ratio values

for the aerosol layers from other measurements or using layer aerosol extinction measurements, where available, from LASE [Ferrare et al., 2000a,b; Ismail et al., 2009]. Nominal aerosol extinction ratios are derived with a vertical resolution of 60 m and horizontal resolution of 2.1 km. LASE aerosol extinction profiles have been shown to have very good agreement with aerosol extinction profiles derived from simultaneous *in* situ LARGE data [Ismail et al., 2009]. During NAMMA, LASE also flew on the NASA DC-8 aircraft.

2.2.3.3 Cloud Physics Lidar

The Cloud Physics Lidar (CPL) is an airborne multi-pulse lidar that has provided observations during several NASA field campaigns [McGill et al., 2004; McGill et al., 2000]. CPL provides profiles of total attenuated backscatter by measuring backscatter at 3 wavelengths (355, 532, and 1064 nm) with a frequency of 5 kHz and depolarization ratio at 1064 nm [McGill et al., 2002]. Processed CPL data is available with a temporal resolution of 1 s and has a spatial resolution of 30 m in the vertical and 200 m in the horizontal [McGill et al., 2002]. As part of the NASA Tropical Composition Cloud and Climate Coupling (TC^4) field campaign (July – August, 2007), CPL flew on the NASA ER-2 aircraft.

2.2.3.4 Surface-Sensing Measurements and Atmospheric Radiative Transfer and Chemical, Optical, and Micro-Physical Measurements of *In Situ* Troposphere

SMART (Surface-sensing Measurements and Atmospheric Radiative Transfer) and COMMIT (Chemical, Optical, and Micro-physical Measurements of In situ Troposphere) are two NASA mobile observatories used to measure physical, chemical, and optical properties of atmospheric composition and particles in the field. Included in the suite of instruments is a TSI Aerodynamic Particle Sizer spectrometer (APS) that provides particle size distributions between 0.5 and 20 μm in diameter and a Cimel sunphotometer that provides measurements of AOT similar to AERONET [Li et al., 2007; Li et al., 2010].

Chapter 3: The Lifecycle and Physical Properties of Dust Aerosols

This chapter describes the physics associated with dust aerosol production and removal and provides a brief discussion of the basic physical properties of dust. Additionally, a description of how the equivalent processes and properties are treated in GEOS-4/5 is provided.

3.1 Source Processes

Dust aerosols originate from erodible soil surfaces that are characteristically dry and free of vegetation. Natural dust sources primarily consist of topographic depressions that have accumulated sediment during the Quaternary Period [Prospero et al., 2002]. Accumulated particles can have a wide range of diameters, spanning from a few microns up to several millimeters [Hillel, 1982]. Soil particles are mobilized by surface winds. Large particles are too heavy to be mobilized by typical surface winds, and the smallest particles are bound to the surface by cohesive forces. Particles with diameters nearly 100 μm are large enough for cohesive forces relative to the wind stress to be small, but are light enough to become mobilized into a bouncing motion along the surface called saltation [Iversen and White, 1982]. During saltation, these soil particles are lifted several centimeters by the wind but quickly fall back to the surface, moving in a bouncing motion. Saltating particles impart their kinetic energy back to soil aggregates at the surface, displacing tiny non-spherical fragments which become *dust aerosol*s, that otherwise were immobile due to cohesive forces. This process is called sandblasting, and

serves as the dominant mechanism for dust aerosol injection into the atmosphere [Gomes et al., 1990]. A conceptual model of dust source processes is provided in Figure 3.1.

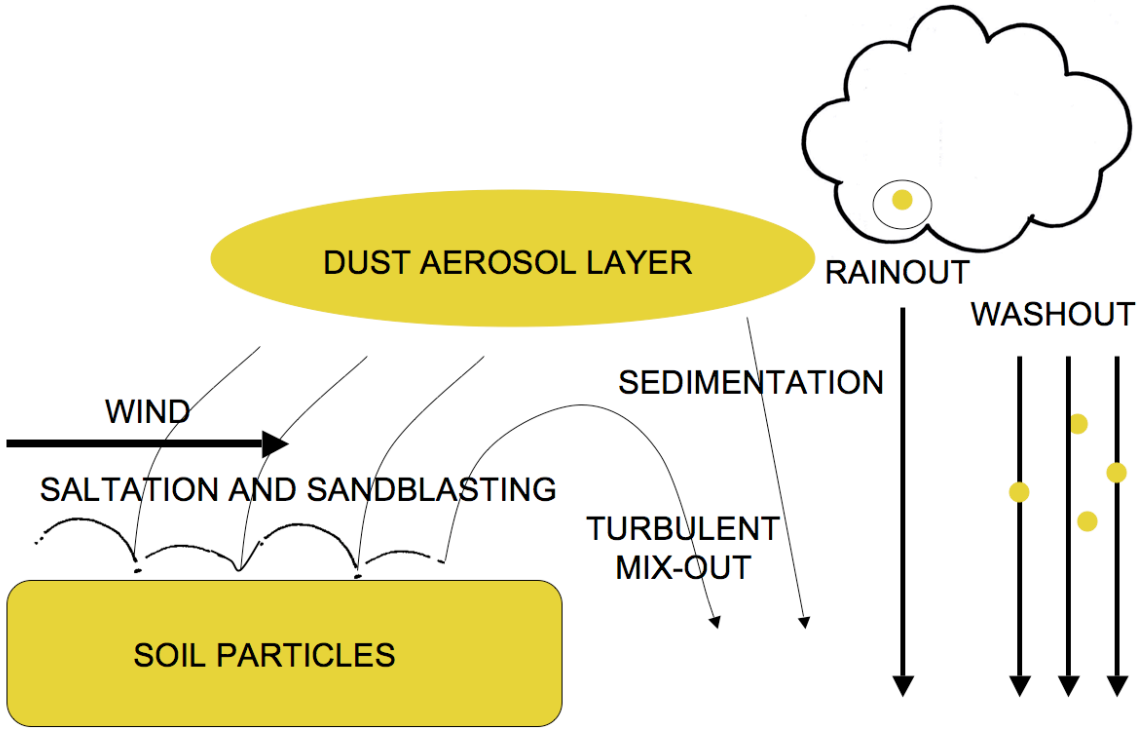

Figure 3.1. Conceptual model of dust source and loss processes.

Reproducing the dust emission process within the framework of a global aerosol transport model is challenging and serves as a major source of uncertainty in models. A dust emission scheme for a global model requires (1) a dust source function that represents the location and relative erodibility or strength of dust sources and (2) a parameterization of the mobilization process. The source function is essentially a map of possible dust source regions based on surface characteristics (e.g., soil type, topography) and specifies the efficiency with which a given surface can emit dust for a given set of meteorological parameters. The mobilization function relates the dust emission to those various meteorological parameters (i.e., wind speed, soil moisture) and involves choices

in how the physics of dust mobilization is parameterized. Dust emission in a model is the convolution of the source function and mobilization function.

The source function used by GEOS-4/5 follows from Ginoux et al. [2001] and Prospero et al. [2002], where bare soil regions are identified as potential dust sources from a 1° × 1° vegetation data set constructed from the advanced very high resolution radiometer (AVHRR) [Defries and Townshend, 1994]. For each grid box, the efficiency for emitting dust is parameterized in terms of its local topography relative to the surrounding grid boxes. Grid boxes that are in relative topographic depressions are assumed to have preferentially collected erodible sediments and serve as stronger dust sources than topographically elevated grid boxes. This approach has shown good consistency between the resulting global dust source function map (Figure 3.2) and dust aerosol locations observed with the Total Ozone Mapping Spectrometer (TOMS) Aerosol Index product [Ginoux et al., 2001] and highlights the major desert regions of the world: the Sahara, the Arabian, the Gobi, and the Taklamakan. Although intra-annual variability in desert cover has been documented [Mahowald et al., 2003] it should be noted that the dust source function used in GEOS-4/5 is invariant in time, as a major portion of this work is on perturbing the dust mobilization process. By assuming a fixed source function, feedbacks between transported particles and topography are neglected. Source region topography (e.g. sand dunes) is both spatially and temporally dynamic, as surface winds may influence the location and strength of dust aerosol sources through sediment transport. Dynamic surface topography also has implications for near-surface meteorology, as changes to topography will influence roughness heights used to determine surface wind speeds that drive dust emission. However, these effects are likely

not significant for dust aerosols, which have a significantly longer atmospheric residence time than larger sand-sized soil particles once mobilized. Using a fixed source function also neglects intra-annual variability and seasonal anthropogenic land practices that may influence the location and strength of dust sources.

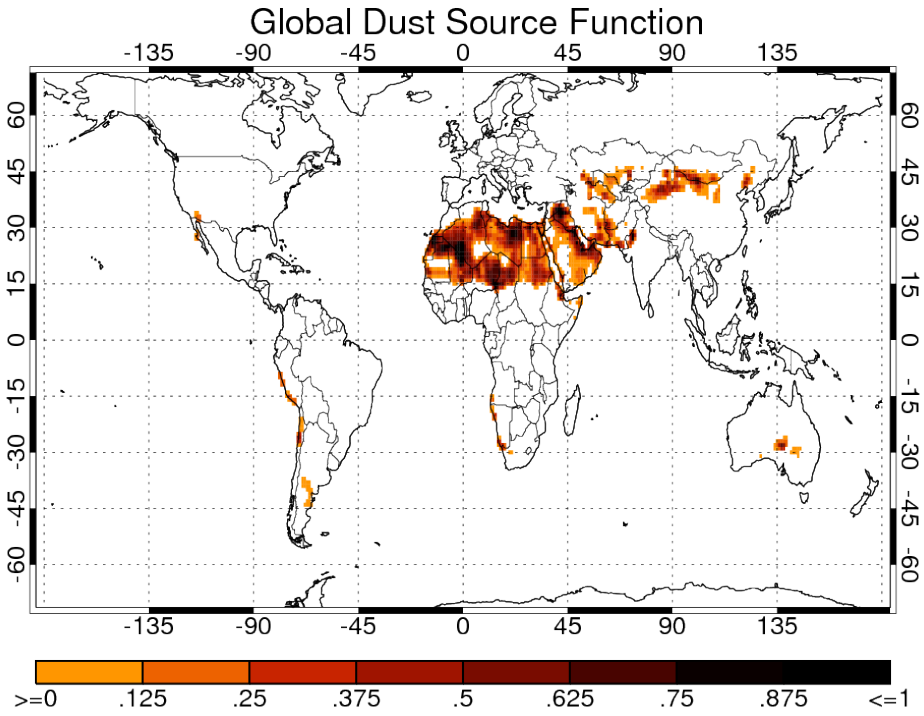

Figure 3.2. Global dust source function map used in the NASA GEOS-4/5 model.

One of the major focuses of this work is investigating the effects of varying the dust mobilization process on simulated dust distributions. In this work, several variations of the mobilization parameterization are considered and described in depth in Chapter 4. Here, the basic components of a mobilization parameterization are presented.

All mobilization schemes considered in this work parameterize dust emission as being proportional to the cube of the surface wind speed relative to a pre-determined

threshold wind speed and distribute the emitted aerosol over a size distributions discretized by several aerosol size bins.

$$F(r) = \begin{cases} C \cdot S \cdot s(r) \cdot U^2 \cdot (U - U_t) & \text{if } U > U_t \\ 0 & \text{otherwise} \end{cases} \qquad \text{Eq. 3.1}$$

where F(r) is the mass flux of aerosol emitted into a size bin of radius r, C is a tuning constant in units of kg m^2 m^{-5} used to set global dust emissions to a desired value, S is the spatial dust source function shown in Figure 3.1, s(r) represents that efficiency of soil at emitting particles of size r, U is the surface wind speed used to drive the emissions relative to a threshold U_t wind speed. Equation 3.1 is only representative of the natural emission of dust aerosols by surface winds. When combined with the spatially invariant source function, the current dust emission model in the GEOS modeling system ignores any anthropogenic contribution, which have been estimated to comprise 10% of the emitted dust mass [Tegen et al., 2004].

It should be noted that the tuning constant C, arises due to the challenge of reproducing the physics associated with the dust aerosol lifecycle within a global aerosol transport model. As discussed in Chapter 1, one challenge of using a global aerosol transport model to simulate aerosol processes is that the grid of the model is significantly greater than *scale* of the physics associated with the dust aerosol lifecycle. Additionally, deficiencies in the parameterizations (i.e., not properly representing a specific process) may also require adjustment to the simulated dust mass flux. Finally, due to the lack of global dust emission observations, models are typically not validated in terms of

emissions. Instead, dust emissions in models are adjusted to give either a specified annual emission rate or, more pragmatically, a specified dust burden that can be compared with observations (e.g., satellite derived AOT retrievals).

3.2 Loss Processes

Once mobilized, dust can be lifted several kilometers in the atmosphere by dry convection and turbulent eddies where it can be transported by upper-level winds. During transport, dust aerosols are subject to removal from the atmosphere through several pathways. These pathways can be characterized in terms of either dry or wet removal processes.

Dry removal processes include sedimentation and turbulent deposition. Sedimentation refers to the settling of dust particles due to the Earth's gravitational force, while turbulent deposition is defined as the transfer of dust aerosols back to the surface of the Earth by turbulent eddies within the planetary boundary layer [Seinfeld and Pandis, 1998]. Dry removal is significant near the dust source regions, as the larger, more massive dust particles will fall from the atmosphere first.

Dust aerosols may also be removed from the atmosphere by wet processes. As previously mentioned, dust aerosols may act as CCN (Chapter 1.1). If a dust CCN is activated to form a cloud droplet, it may coagulate with other cloud droplets to form a hydrometeor. If the hydrometeor falls to the Earth's surface, the dust aerosol has said to be removed by rainout [Seinfeld and Pandis, 1998]. A similar wet removal process is washout [Seinfeld and Pandis, 1998], where a falling hydrometeor may collide and coagulate with dust aerosols, depositing the aerosol at the Earth's surface. Because dry

removal processes dominate near the dust source regions, wet removal processes become more significant downwind of the source region. Figure 3.1 also provides a conceptual model of the various loss processes associated with dust aerosol removal.

These dry and wet removal processes are parameterized in the GEOS-5 model. In GEOS-4/5, both sedimentation and dry deposition are parameterized as size dependent processes. Following Ginoux et al. [2001] and Chin et al. [2002], Stokes law is used to calculate the size-dependent fall velocity $v_s(r)$ for sedimentation:

$$v_s(r) = \frac{2}{9} \cdot \frac{\rho_p \cdot g}{\mu} \cdot r^2 \cdot C_{cunn} \qquad \text{Eq. 3.2}$$

where ρ_p is the density of the dust particle, g is the acceleration due to gravity, μ is the viscosity of air, r is the radius of the dust particle, and C_{cunn} is the Cunningham slip correction factor for determining the opposing drag force on the particle [Seinfeld and Pandis, 1998].

Ginoux et al. [2001] and Chin et al. [2002] also define the deposition velocity for turbulent deposition. The turbulent deposition velocity, v_d is related to exchange of heat and moisture between the atmosphere and the Earth's surface and is parameterized as the inverse of sum of the aerodynamic, sublayer, and surface resistances of the lowest model layer:

$$v_d = \frac{1}{r_a + r_b + r_s} \qquad \text{Eq. 3.3}$$

where r_a is the aerodynamic resistance of the surface layer and is a function of surface heat and moisture fluxes, r_b is the resistance due to quasi-laminar sublayer resistance above the surface, and r_s it the resistance from the surface.

Particles that are deposited at the surface may be re-suspended if the surface soil moisture is low and the wind speed is sufficiently high. To account for this, v_d is modified as follows:

$$v_d(r) = \begin{cases} v_d \cdot (w + (1 - w) \cdot \exp[-(U_{10m} - U_t(r))] & \text{if } U > U_t \\ v_d & \text{otherwise} \end{cases} \quad \text{Eq. 3.4}$$

where w is the surface soil moisture, U_{10m} is the 10-meter wind speed, and $U_t(r)$ is the size-dependent dry threshold speed for dust mobilization as described in Ginoux et al. [2001]. In this formulation, the dry deposition velocity, v_d will be reduced under conditions when the wind speed is high and the soil is dry.

Wet removal processes in GEOS-4/5 are size independent and include removal by rainout (in-cloud scavenging) and washout (below-cloud scavenging) by large scale and convective precipitation determined by the model. It should be noted that GEOS-4/5 does not currently have the capability for dust aerosols to explicitly serve as CCN. Following Chin et al. [2000], the large-scale removal by rainout is parameterized in terms of the precipitation frequency and fraction of the model grid box covered by precipitating clouds:

$$\Delta\gamma(k) = fwet_{ls} \cdot \gamma(k) \cdot f_{ls}(k) \cdot (1 - \exp^{\beta_{ls}(k)\Delta t}) \quad \text{Eq. 3.5}$$

where $\Delta\gamma$ is the change in the dust mass mixing ratio, $fwet_{ls}$ is the scavenging efficiency of dust removal (i.e., hygroscopicity), γ is the mass mixing ratio of dust, f_{ls} is the fraction of large-scale precipitating clouds within the grid box, β_{ls} is the large-scale precipitation frequency for duration Δt at each model level k. Convective removal by rainout follows from Balkanski et al. [1993] and is proportional to the convective updraft mass flux:

$$\Delta\gamma(k) = fwet_{conv} \cdot \gamma(k) \cdot F_u(k) \cdot g \cdot p(k)^{-1} \qquad \text{Eq. 3.6}$$

where $\Delta\gamma$ is the change in the dust mass mixing ratio, $fwet_{conv}$ is the convective scavenging efficiency of dust removal, γ is the mass mixing ratio of dust, F_u is the convective updraft mass flux, g is the acceleration due to gravity, and p is the atmospheric pressure at each model level k.

For both large-scale and convective precipitation, washout is parameterized similar to rainout, but occurs only for grid boxes below the largest fraction of precipitating clouds (f) [Chin et al., 2000].

3.3 Physical Properties

Dust aerosols are non-spherical and have a size range that typically spans 0.1 – 10 μm in radius [Kok, 2011]. Compared to particle size distributions of anthropogenic aerosols, the dust particle size distribution has a greater contribution from particles in the coarse mode (i.e., greater than 1 μm) (Figure 3.3).

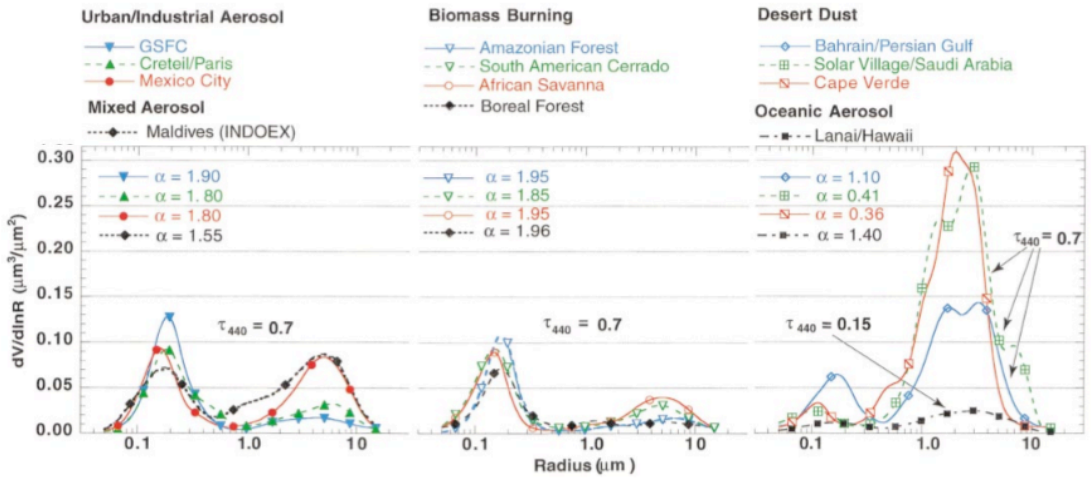

Figure 3.3. AERONET observed particle size distributions from urban/industrial, biomass burning, dust, and sea salt dominated sites from Dubovik et al., 2002.

Dust aerosols are treated as spheres in GEOS-4/5 and are distributed across five transported size bins. Based on Tegen and Lacis [1996] and Ginoux et al. [2001], the following radius bins are chosen: 0.1-1, 1-1.8, 1.8-3, 3-6, and 6-10 μm. The sub-bin particle size distribution of each bin follows from Tegen and Lacis [1996] in that dMass/(dln r) is assumed to be constant. This determines an effective radius for each bin, which is used in emission and sedimentation calculations: 0.73, 1.4, 2.4, 4.5, and 8 μm. However, sub-micron particles are significant for optical calculations and therefore, the first (smallest) size bin is further divided into four sub-bins, following Tegen and Lacis [1996]. Dust optical properties used in GEOS-4/5 follow from the Global Aerosol Dataset (GADS) [Köpke et al., 1997], providing mass extinction coefficients for converting the simulated dust mass to AOT.

Chapter 4: Investigation of Dust Source Processes

4.1 Introduction

To reiterate, simulating dust aerosol emissions in a global model requires (i) a source function that represents the relative strength of individual dust sources regions and (ii) an emission scheme that parameterizes dust emissions, usually as a function of wind speed, surface properties, and soil moisture. One key area of uncertainty in simulated dust distributions lies in the treatment of source processes, where emission scheme choice and identification of source regions can have implications for emitted dust fluxes [Zender et al., 2004].

In this chapter, the effect of varying the dust emission scheme in the NASA GEOS modeling system is explored by considering two dust emission schemes that initiate emission and treat the emitted particle size distribution differently. The simulations were run at the same model spatial resolution with identical source functions and loss processes as described in Chapter 3.

Additionally, this chapter explores the effect of model spatial resolution on both the mobilization and source processes. In particular, the capability of the NASA GEOS modeling system is utilized to simulate dust emissions at various spatial resolutions. Specifically, in a set of experiments, the source function is allowed to vary with model spatial resolution for various considerations of the mobilization process. The source function is then held constant to understand the effect of source function resolution on simulated dust emissions.

Throughout this chapter, many observational datasets are employed to validate simulated dust distributions. In particular, the investigations exploit two data-rich time periods centered on the NASA NAMMA and SMART - COMMIT field campaigns.

4.2 Investigation of Dust Mobilization Process

Here, the sensitivity of simulated dust distributions to dust mobilization function choice is explored in the NASA GEOS-4 Earth system model (see Chapter 2.1). Two different dust mobilization functions are considered: The GOCART scheme based on Ginoux et al. [2001] and the Dust Entrainment and Deposition (DEAD) scheme from Zender et al. [2003]. To evaluate the simulated dust distributions, the period of the NASA African Monsoon Multidisciplinary Analyses (NAMMA) (August – September, 2006) provides a suite of *in situ* and remotely sensed aircraft observations, as well as remote sensing observations from the space-based MISR, MODIS-Aqua, OMI, and CALIOP instruments and ground-based observations from AERONET sunphotometers in North as described in Chapter 2.2.

Previously, Cakmur et al. [2006] showed that for a single choice of mobilization function, simulated dust distributions are sensitive to a varying source function. On the other hand, Luo et al. [2003] showed that the choice of mobilization function influence simulated dust concentrations, but their analysis was on longer climate scales and did not focus on specific events. Colarco et al. [2003] examined the role of source and mobilization function choice on transported dust distributions during the Puerto Rico Dust Experiment (PRIDE), but did not unravel separately the effect of mobilization function for a given source function. This work builds upon Colarco et al. [2003] and Luo

et al. [2003] by evaluating the mobilization function choice for a well-observed case study (NAMMA) and is the first to do so with particular attention to the impact of mobilization function choice on dust vertical dust distributions, which have been evaluated with airborne and space-based lidar observations.

4.2.1 Description of Dust Emission Parameterizations

Wind tunnel experimentation has long been used to obtain an empirical expression for the relationship between the surface wind speed and horizontally saltating mass flux of soil particles [Greenley and Iversen, 1985]. These experiments found a cubic relationship between the horizontally saltating mass flux and the surface friction speed relative to a threshold speed. Iversen and White [1982] found a semi-empirical parameterization (Equation 4.1) for the dry threshold speed (u_*) required for particle saltation as a function of soil particle diameter (Figure 4.1):

$$u_{*_t} = 0.13 \cdot \sqrt{\frac{\rho_p \cdot g \cdot D}{\rho_a}} \cdot \sqrt{\frac{1 + 6e^{-7}}{\rho_p \cdot g \cdot D^{2.5}}} \cdot \frac{1}{\sqrt{1.928 \cdot (1331 \cdot (100 \cdot D)^{1.56+0.38})^{0.092-1}}} \qquad \text{Eq. 4.1}$$

where ρ_p is the soil particle density, g is the acceleration due to gravity, D is the soil particle diameter, and ρ_a is the atmospheric density.

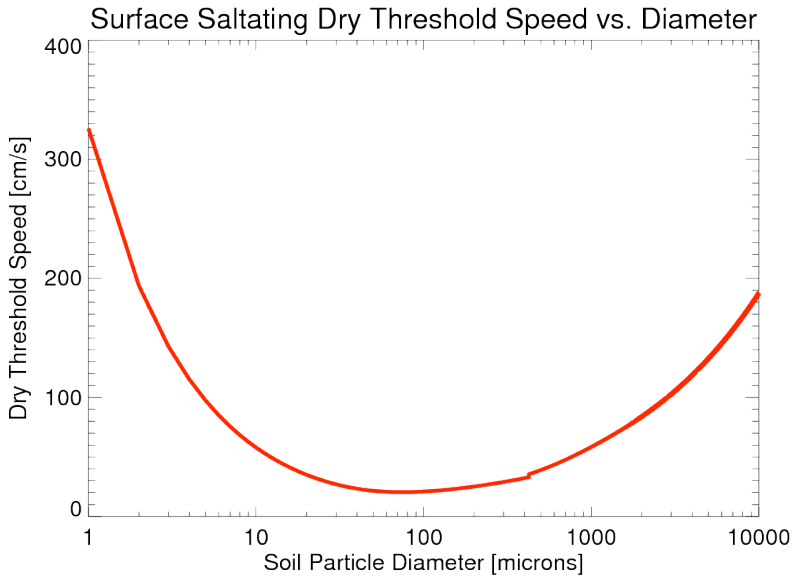

Figure 4.1. Marticorena and Bergametti [1995] surface dry saltating threshold speed vs. soil particle diameter.

Marticorena and Bergametti [1995] combined the observed cubic relationship between particle saltation and the surface wind speed with theoretical assumptions regarding the characteristic pathlength of particle saltation to formulate a mass flux equation for horizontally saltating particles as a function of the surface wind speed relative to a threshold, which serves as basic structure of the parameterization of the dust mobilization process in global aerosol transport models. In this study, two different mobilization parameterizations are considered. The first emission scheme is based on the GOCART scheme from Ginoux et al. [2001] and has been serving as the standard dust mobilization scheme in the GEOS modeling system. As an alternative, a version of the DEAD scheme based on Zender et al. [2003] has been implemented. Both schemes parameterize dust emission in terms of the surface wind speed and distribute the emitted aerosol over a size distributions discretized by several size bins.

Both the GOCART and DEAD schemes use the parameterization of the dry threshold wind speed for mobilization developed by Iversen and White [1982] (Eq. 4.1), but diverge at this point. In the GOCART scheme, the dry threshold wind speed is computed as a function of *aerosol particle size* according to the size bins chosen and emissions are then parameterized in terms of the 10 m wind speed, where U_{10m} has become U in Equation 3.1:

$$F(r) = \begin{cases} C \cdot S \cdot s(r) \cdot U_{10m}^2 \cdot (U_{10m} - U_t(r,w)) & \text{if } U_{10m} > U_t \\ 0 & \text{otherwise} \end{cases} \qquad \text{Eq. 4.2}$$

where F(r) is the mass flux of aerosol emitted into a size bin of radius r, C is a tuning constant in units of kg m^2 m^{-5} used to set global dust emissions to a desired value, S is the spatial dust source function shown in Figure 3.2, s(r) represents the efficiency of soil at emitting particles of size r, U_{10m} is the 10 m wind speed, and U_t is the size dependent threshold wind speed from Iversen and White [1982] (Figure 4.1) that has been modified for the presence of soil moisture w (m^3 m^{-3}) following Ginoux et al. [2001].

By contrast, the DEAD scheme connects the threshold wind speed to the initiation of saltation rather than direct aerosol injection. Sandblasting caused by saltation is the main dust entrainment mechanism for sustained emission [Shao and Raupach, 1993] and makes the emissions physics of the DEAD scheme more satisfying. Unfortunately, determining soil grain saltation requires knowledge of the particle size distributions of the parent soil bed, which is not well known on global scales. Following Zender et al. [2003] for the implementation of DEAD, the parent soil is assumed to contain a fixed

monomodal soil particle size distribution of optimally sized particles of 100 μm in diameter with a corresponding dry mobilization threshold u_t^*=0.209 m s^{-1} (Figure 4.1) for the computation of the horizontal saltating mass flux. In this fashion, the threshold formulation from Iversen and White [1982] is used to determine the initiation of soil particle saltation as a function of surface properties and friction speed. The aerosol mass injected is proportional to the horizontal saltation flux, which is computed in terms of the threshold wind speed and the wind friction speed (as opposed to the 10 m wind speed used by the GOCART scheme):

$$F(r)' = \begin{cases} C' \cdot S \cdot s(r)' \cdot u^{*3} \cdot \left(1 - \frac{u_t^*(w)}{u^*}\right)\left(1 + \frac{u_t^*(w)}{u^*}\right) & \text{when } \frac{u_t^*}{u^*} < 1.0 \\ 0 & \text{otherwise} \end{cases} \qquad \text{Eq. 4.3}$$

where F(r)′ is the mass flux of aerosol into a size bin of radius r, C′ is a global tuning constant that incorporates the efficiency with which the horizontal saltation flux translates to a vertical aerosol mass flux, S is the same dust source function used in Equation 4.2, and s(r)′ is the aerosol particle size distribution. The surface friction speed from the land surface model, u* is used to drive dust emissions and it has been increased to account for the transfer of momentum to the surface from saltating particles, known as the Owen effect [Gillette et al., 1998]. The threshold surface friction speed, u_t* is increased to account for the loss of atmospheric momentum to nonerodible objects within the soil (e.g., rocks, vegetation) by assuming a fixed drag efficiency for all model grid cells, following Marticorena and Bergametti [1995] and is increased for the presence of soil moisture following Fécan et al. [1999].

Comparing Equations 4.2 and 4.3, the dust emission fluxes in both schemes have a cubic dependence of the surface wind speed relative to some threshold. Because this is an empirical relationship based on observations, it serves as a potential source of error in the mobilization parameterization. The relationship between particle saltation and the surface wind speed may exhibit variability under different atmospheric conditions or between global source regions. However, a change to the power relationship (e.g. cubic vs. quadratic dependence) would have implications for the magnitude but not the timing of dust events. Moreover, because simulated dust distributions are tuned to match observed AOT magnitude, tuning constant may compensate for errors parameterized relationship between particle saltation and the surface wind speed. Perhaps a more significant source of error in the dust emission parameterization is the surface wind speed and how it is related to the threshold, which will have implications for both the timing and the magnitude of simulated dust events. In the GOCART scheme, the relevant wind speed is the 10-m wind speed U_{10m}, while in the DEAD scheme the relevant wind speed is the surface friction speed u^*. Both schemes use the same threshold speed parameterization of Iversen and White [1982], but apply it differently. The formulation in the GOCART scheme implies that $U_t = u_t^*$, with modifications for soil moisture content. This simplification captures observed dust aerosol distributions by requiring higher surface wind speeds to mobilize smaller aerosol particles, but neglects the physics of saltation and assumes that the parent soil particle distribution is only comprised of aerosol sized particles. This assumption has implications for the simulated mass of emitted aerosol, but has been shown to have good agreement with observed AOT values, which are used to constrain simulated dust distributions [Ginoux et al., 2001]. The

parameterization for mobilizing physics in DEAD is more physically satisfying in that it explicitly accounts for saltation and sand-blasting, but it is itself a simplification in that it neglects variability in soil particle size distributions, distributions of erodible surfaces within grid cells, and differences in the efficiency of horizontal to vertical mass flux transfer that depend on soil type. By assuming a monomodal soil particle distribution of optimally sized particles (100 μm), saltation may occur for the lowest wind threshold (Figure 4.1). However, in reality, soil particles may span a wide range of diameters with a range of mobilization thresholds. This assumption will act to initiate dust events more frequently and with a greater saltating mass flux magnitude when compared to a simulation where a range of soil particle diameters is considered. Grini and Zender [2004] modified DEAD to evaluate the effects of sub-grid scale winds and different soil bed particle size distributions, showing that these modifications affect simulated dust mass concentrations, optical depths, and the fraction of coarse particles, but not the timing of dust events.

It should be noted that both mobilization parameterizations neglect certain feedbacks to the physical environment. Anderson and Haff [1988] found that saltating mass fluxes influence roughness heights, which in turn modify the wind profile of the surface layer, which influences surface winds used to drive dust emissions. Currently, this effect cannot be represented in the model because neither scheme actually simulates a horizontally saltating mass flux. To reiterate, in the GOCART scheme, aerosol-sized soil particles are emitted directly into the atmosphere, thereby neglecting the physics of saltation. In the DEAD scheme, the horizontal mass flux is only computed, rather than simulated, of which a fraction is emitted in the vertical.

For both emission schemes, dust aerosols are removed by dry and wet removal processes as described in Chapter 3.2. Both schemes distribute the emitted aerosol mass across the five transport size bins as described in Chapter 3.3. For the GOCART scheme, the mass emitted to each bin is computed independently, based on how the wind speed exceeds the threshold for that bin. The soil particle size distribution enters as *s(r)* as in Equation 4.2 (following Tegen and Fung [1994]), where the mass of emitted clay particles ($0.1 < r < 1$ μm) is assumed to be 1/10 of the total mass of emitted silt (particles of radius > 1 μm), that is $s = 0.1$ for the smallest bin. The four silt bins (1-1.8, 1.8-3, 3-6, and 6-10 μm) are each assigned a mass fraction of $s = 0.25$. The emitted particle size distribution is dynamically determined in the GOCART scheme in that the threshold is computed for each size bin independently. In contrast, the DEAD scheme imposes a fixed tri-modal lognormal distribution on the emitted aerosol that is based on the observed background dust particle size distributions near Saharan dust sources [D'Almeida, 1987]. Dust optical properties are as described in Chapter 3.3.

Table 4.1 summarizes the GOCART and DEAD emission schemes. Aside from the difference in winds used to parameterize the emission process, the major difference in the two schemes is that the emitted particle size distribution is fixed in the DEAD scheme, while it is dynamically generated in the GOCART scheme depending on the difference between the surface wind speed and the size-dependent threshold wind speed. However, because of how the threshold wind speed is applied in the GOCART scheme, the threshold speeds are generally much smaller than the 10 m wind speed ($U_t << U_{10m}$), so that in practice there is little dynamical variation in the emitted size distribution. Both schemes have a drawback in that they are both *in situ* parameterizations that have been

applied to a model grid. Box-averaged parameters (i.e., wind speed and soil moisture) are used to represent the micro-scale processes that modulate dust emissions and cannot account for sub-grid variability. Because of this, global tuning constants are required to set the total global emissions for both schemes when they are applied to the model grid.

SCHEME	GOCART	DEAD
Source Function	Bare Topographical Depressions - Ginoux [2001]	Bare Topographical Depressions - Ginoux [2001]
Dry Emission Threshold Speed	Wind Tunnel Experiments - Marticorena and Bergametti [1995]	Wind Tunnel Experiments - Marticorena and Bergametti [1995]
Threshold Speed Modifications	Soil Moisture Content – Ginoux [2001]	Soil Moisture Content – Fecan [1999] & Non-Erodible Objects – Marticorena and Bergametti [1995]
Wind Parameter Used to Determine Emitted Mass Flux	10-meter Wind Speed	Surface Friction Speed
Flux Equation [F(r), F(r)′]	$F(r) = C * s(r) * u10m^2 * (u10m - ut(r,w))$	$F(r)' = C' * S * s(r)' * u^{*3} * \left(1 - \frac{u_t^*(w)}{u^*}\right)\left(1 + \frac{u_t^*(w)}{u^*}\right)$
Size Distribution	Dynamic	Static
Bin Depedendent Mass Fractions [s(r), s(r)′] Bin: r_{eff} = .73μm (.1-1μm) r_{eff} = 1.4μm (1-1.8μm) r_{eff} = 2.4μm (1.8-3μm) r_{eff} = 4.5μm (3-6μm) r_{eff} = 8μm (6-10μm)	s(r) Tegen and Fung [1994]: 0.1 0.25 0.25 0.25 0.25	s(r)′ D'Almeida [1987] 0.112 0.232 0.296 0.277 0.064
Constants [C, C′]	C = 0.375e-9 kg s^2 m^{-5}	C′ = C′′*α = 1.780e-5 kg s^2 m^{-5} where C′′ = 3.716-4 kg s^2 m^{-5} and α=0.0479 is the sandblasting mass efficiency after assuming a globally uniform mass fraction of clay particles of 0.2

Table 4.1. GOCART and DEAD emission scheme comparison.

4.2.2 Results

From August 19th to September 12th, 2006, the NASA African Monsoon Multidisciplinary Analyses (NAMMA) field experiment was conducted from the Cape

Verde Islands to help understand the evolution of African easterly waves (AEWs), precipitation systems, and Saharan dust events over western Africa. Saharan dust events are primarily initiated by dry convection caused by intense solar heating [Carlson and Prospero, 1972; Karyampudi et al., 1999]. Atmospheric mixing induced by dry convection leads to the formation of a deep boundary layer mixed with dust aerosol and can be transported over the Atlantic Ocean to the Caribbean as the Saharan Air Layer (SAL) [Karyampudi et al., 1999; Wong et al., 2009]. The SAL is stable, bound by a low-level temperature inversion atop the marine boundary layer near 1.5 km and radiative cooling at the top near 3.7 km [Carlson and Prospero, 1972]. As solar intensity peaks during the Northern Hemisphere summer, thermal wind balance leads to the formation of the African Easterly Jet (AEJ), which acts to transport the SAL westward on the north side of the jet axis [Carlson and Prospero, 1972; Karyampudi et al., 1999]. During transport, the thickness, and upper and lower bounds of the suspended dust aerosol layer are determined vertical turbulent mixing that transports dust particles upward and sedimentation, which transports dust particles toward the surface.

NAMMA observations included 13 science flights made with the NASA DC-8 aircraft. Here, only observations of the SAL obtained with lidar measurements of vertical structure [Ismail et al., 2008; 2009] and *in-situ* measurements of particle size distributions [Chen et al., 2009; Clarke et al., 2007; McNaughton et al., 2007] taken aboard the DC-8 are considered. In addition to the airborne observations of dust, correlated observations from ground-based sun photometers and several space-based remote-sensing platforms are utilized. These data sets are used to evaluate the performance of the GOCART and

DEAD emission schemes and to identify differences between their simulated dust distributions.

The model results presented below come from two sets of GEOS-4 simulations of global aerosol distributions for the year 2006. In both simulations, the model was run at 1^o x 1.25^o horizontal resolution on 32 hybrid eta vertical levels, with aerosol fields output every 6 hours. The simulations are made in replay mode, driven by the GEOS-4 analysis products. Due to the lack of mass-based observations, global transport models are typically constrained in terms of observed column AOT distributions. For these simulations, GOCART emissions have been tuned to match the mass budget of emissions from Ginoux [2001], which were shown to produce reasonable AOT values as described in Colarco et al. [2010]. DEAD emissions were scaled so that the resultant regionally averaged AOT over North Africa was the same as the regionally averaged GOCART AOT over North Africa during the NAMMA period. Both simulations were run with the full complement of GOCART aerosols, but we vary the dust emission scheme in each. Thus, differences in simulated dust distributions can be directly attributed to the varying parameterizations of the dust emission process.

4.2.2.1 Emission and Aerosol Optical Thickness Distributions

Figure 4.2 shows the August-September average dust emissions and 550 nm AOT for the GOCART and DEAD emission schemes. Displayed in the bottom left corner of each panel is the August-September average total dust emissions or mean AOT over North Africa, depending on the quantity of interest. The distinct difference between the

emission schemes is that the DEAD emissions are more geographically sparse in their distribution over the continent than the GOCART emissions.

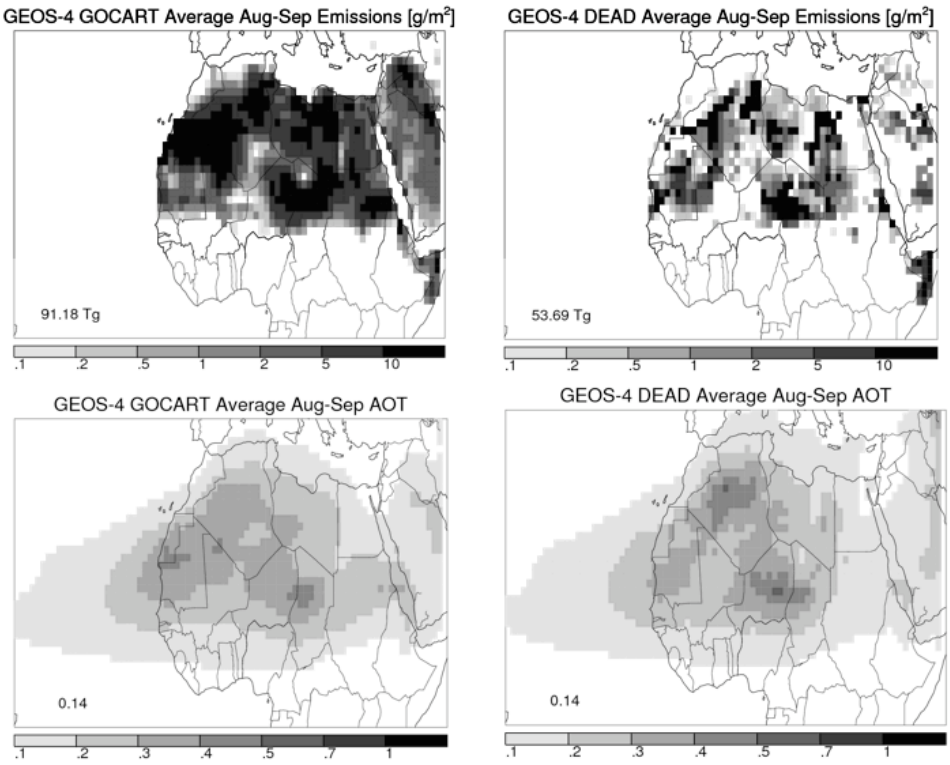

Figure 4.2. August – September (top) average emissions and (bottom) AOT for (left) GEOS-4 GOCART and (right) GEOS-4 DEAD emission schemes. Total region emissions (Tg) and average AOT are displayed in the bottom left of each plot.

GOCART emissions typically occur wherever the source function is non-zero, because the 10-meter wind speed can be an order of magnitude greater than the bin-dependent threshold speeds. Typical NAMMA August-September average 10-meter wind speed values over the source region are about 3.5 ms^{-1}, while the GOCART size-dependent dry threshold speeds range from 2.45 ms^{-1} (smallest transport bin) to 0.41 ms^{-1} (largest transport bin). In contrast, because typical August-September average surface friction speeds and the dry threshold speed are comparable in magnitude (about 0.23 ms^{-}

[1]), the spatial distribution of DEAD emissions is sparse. Additionally, when the confounding effect of soil moisture on the threshold speeds is considered (Figure 3.4), DEAD emissions are more likely to be modulated by the presence of soil moisture. The GOCART scheme emits a greater average mass of dust (91 Tg) when compared to DEAD (54 Tg) during the NAMMA period. We recall that the magnitude of emissions in each scheme was tuned to yield a comparable, regional-average AOT (τ_{550} = 0.14, Figure 3.3) that is consistent with Colarco et al. [2010].

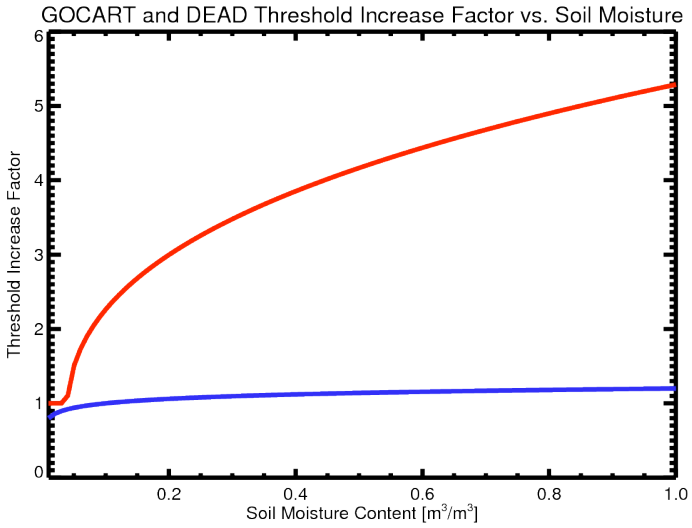

Figure 4.3. GOCART (blue) and DEAD (red) dry threshold increase factor vs. soil moisture content.

Despite the large difference in the emission magnitude, the same regional AOT value is obtained because the two schemes emit particles of different sizes, with differing optical efficiencies. Figures 4.4a and 4.4b show the August-September averaged values of size-dependent dust emissions (solid), dry deposition (dashed), and the fractional dust AOT contribution over North Africa. The GOCART scheme emits a greater mass of particles than the DEAD scheme in all but the first size bin. This is a consequence of

how the threshold equation is applied to determine direct aerosol injection in the GOCART scheme instead of to determine the initiation of saltation as in the DEAD scheme. Here, the threshold wind speed is relatively low for large particles (bins 4 and 5). However, these large particles settle quickly from the atmosphere (as evidenced by the high dry deposition values) and have little contribution to the total AOT. In contrast, in the DEAD scheme the threshold equation determines the onset of saltation, and a static aerosol particle size distribution is assumed such that the peak aerosol emission occurs in the 3rd transport bin (Table 4.1). Similar to the GOCART scheme, the fifth transport bin has comparable values of emissions and dry deposition, indicating that nearly all emitted particles at this size are removed rapidly. The DEAD scheme emits relatively more optically efficient particles in the first transport size bin. Figure 4.4b shows how this corresponds to a larger contribution to the total dust AOT from these particles than in the GOCART scheme, and is the explanation for the comparable regional AOT values obtained despite the large difference in the emitted aerosol mass.

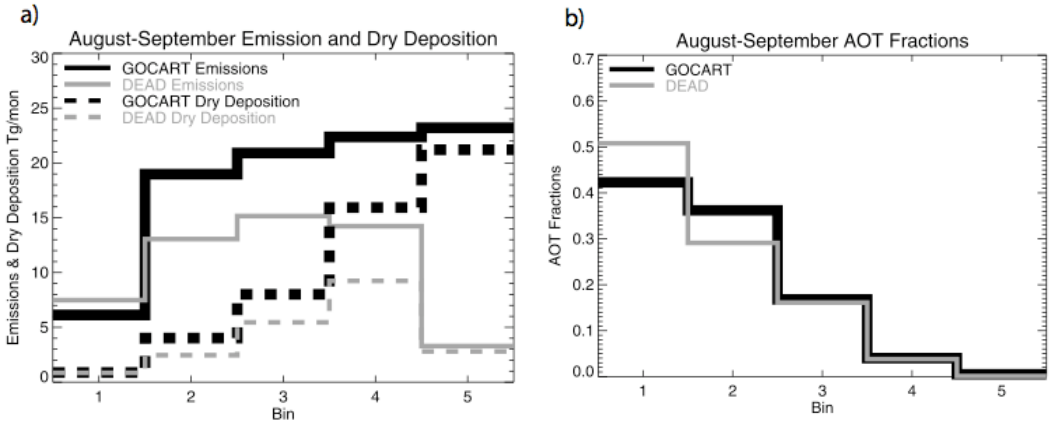

Figure 4.4. (a) August – September average total emissions (solid), total dry deposition (dashed). (b) August – September average fraction of dust AOT for each transport bin over North Africa for the GOCART (black) and DEAD (gray) emission schemes.

4.2.2.2 Comparisons of Aerosol Optical Thickness

To help validate simulated spatiotemporal dust distributions using the GOCART and DEAD emission schemes during NAMMA, comparisons are made to measurements of AOT from the space-borne MISR instrument and ground-based AERONET sunphotometers. When making comparison between simulated and observed distributions, it is useful to discuss the different methods used to obtain the quantity of interest. In the model, aerosol mass loadings are converted to AOT using a look-up table of mass extinction efficiencies provided by aerosol models and are a function of particle type, radius, and relative humidity. For satellite based observations such as MISR and MODIS, observed reflectances are used to indirectly determine AOT values. However, this method relies first on removing the surface reflectance in order to determine the contribution from aerosols. The method for determining the surface reflectance is unique for each satellite, but in general employs using reflectances from multiple channels to estimate the surface reflectance. Once the aerosol contribution is determined, aerosol models that are reflective of the regional aerosol type are used to determine the AOT. For AERONET sunphotometer observations, AOT is directly observed by measuring direct sun extinction. While AERONET may provide the purest measurement of AOT for model validation, it limited by providing a point measurement that may observe local features that are impossible to resolve in a global model. However, when used together, satellite observations are useful to validating simulated spatial aerosol distributions, while AERONET is most useful for evaluating the timing of aerosol events.

4.2.2.2.1 Multi-Angle Imaging Spectroradiometer

Figure 4.5 shows monthly mean MISR [555 nm], GEOS-4 GOCART [550 nm], and GEOS-4 DEAD [550 nm] AOT from all aerosols during August and September. For a consistent comparison, GEOS-4 AOT values have been sampled from grid cells at the synoptic time nearest the MISR retrieval. On each plot, white areas correspond to regions where MISR was unable make any retrieval at all (e.g. due to clouds) and therefore did not sample the model. In August, MISR reports moderate AOT values (~0.6) over most of the southern Saharan desert, with two AOT hot spots (>1.0) over Mauritania and Mali (Box 1) and Lake Chad (Box 2). Over the tropical North Atlantic Ocean, AOT values are moderate off the coastline, but drop off quickly west of 30W (Box 3). In comparison, both GEOS-4 simulations have AOT values that are 30-50% less than MISR over the southern Saharan desert and at least 50% less over the hot spots (Boxes 1 and 2). Just off the coastline, GEOS-4 AOT magnitudes are comparable to MISR, but drop off more quickly toward the west near 22.5W (Box 3). Over the tropical North Atlantic Ocean, the MISR dust plume extends all the way to the Caribbean, while both GEOS-4 plumes are not as pronounced. Comparing the GEOS-4 simulations, both emission schemes simulate comparable AOT distributions of North Africa, with the GOCART scheme matching MISR better over Mauritania and Mali (Box 1) and the DEAD scheme having slightly better agreement with MISR over the Lake Chad region (Box 2). During September, MISR retrieves moderate AOT values (~ 0.6) over the southern Saharan desert again, but only has one hot spot over Lake Chad (Box 2). Over the tropical North Atlantic Ocean in September MISR shows somewhat lower AOT near the African coast than in August. In both months, MISR shows long-range transport of high dust AOT into the western Atlantic and Caribbean. Although the dust transport

appears to carry further west in August, the peak of the AOT is higher (~ 0.4 – 0.5) and appears further west (at about 50° W) than in August (Box 3). Both GEOS-4 simulations capture the lower values near the coastline, but not the apparent extended long-range transport in September. Comparison of the MISR observations to MODIS Aqua AOT (not shown) suggests that the pattern of transport MISR shows in September is somewhat a sampling artifact. The MODIS observations provide daily near-global AOT retrievals, compared to the MISR narrower swath observations, which obtain global coverage approximately every nine days. In short, the MISR observations emphasize a particular event that the model underestimated. Over North Africa, both GEOS-4 simulations produce AOT distributions that are more comparable in magnitude to one another than to MISR. Both schemes simulate maximum AOT values over the Lake Chad region, where the DEAD scheme is more comparable with MISR (Box 2). Again, both schemes simulate AOT values that are 50% less than values retrieved by MISR over Mauritania and Mali (Box 1). Over the tropical North Atlantic Ocean, neither scheme captures the magnitude and westward extent of the MISR dust plume over the tropical North Atlantic Ocean (Box 3).

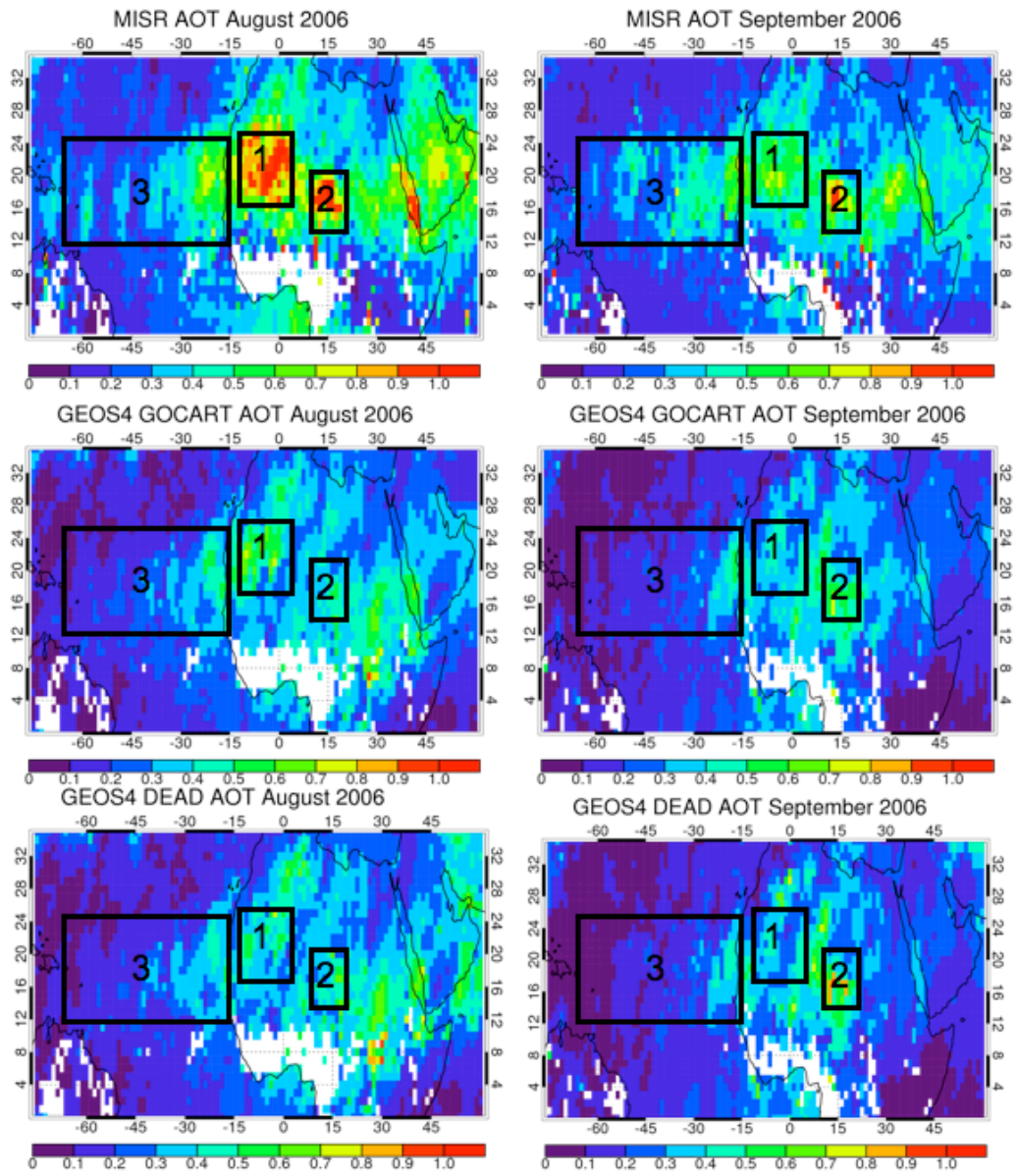

Figure 4.5. (top) MISR AOT, (middle) GEOS-4 GOCART AOT, and (bottom) GEOS-4 DEAD AOT during (left) August and (right) September. Boxes 1 – 3 are regions of interest for model evaluation.

Figure 4.6 shows the day-to-day variation of the MISR and simulated AOT as averaged within each of the three boxes illustrated in Figure 4.5. When compared to MISR, both model simulations consistently underestimate the magnitude of AOT in all three boxes. The coefficient of determination correlation (R^2) of the model and MISR AOT is worst for both simulations in the region of Lake Chad (Box 2: GOCART R^2 =

0.058, DEAD $R^2 = 0.259$). Correlation is more modest over Mali and Mauritania (Box 1: GOCART $R^2 = 0.410$, DEAD $R^2 = 0.395$) and also over the Tropical North Atlantic (Box 3: GOCART $R^2 = 0.560$, DEAD $R^2 = 0.377$). It is evident that the model has difficulty with the timing of dust events over Lake Chad, but improves downwind. While Box 1 correlates moderately well with MISR, both simulations underestimate the AOT magnitude by nearly 50% throughout August. The simulations compare best over the Tropical Atlantic Ocean (Box 3) where AOT magnitudes are most similar to MISR and have modest correlations.

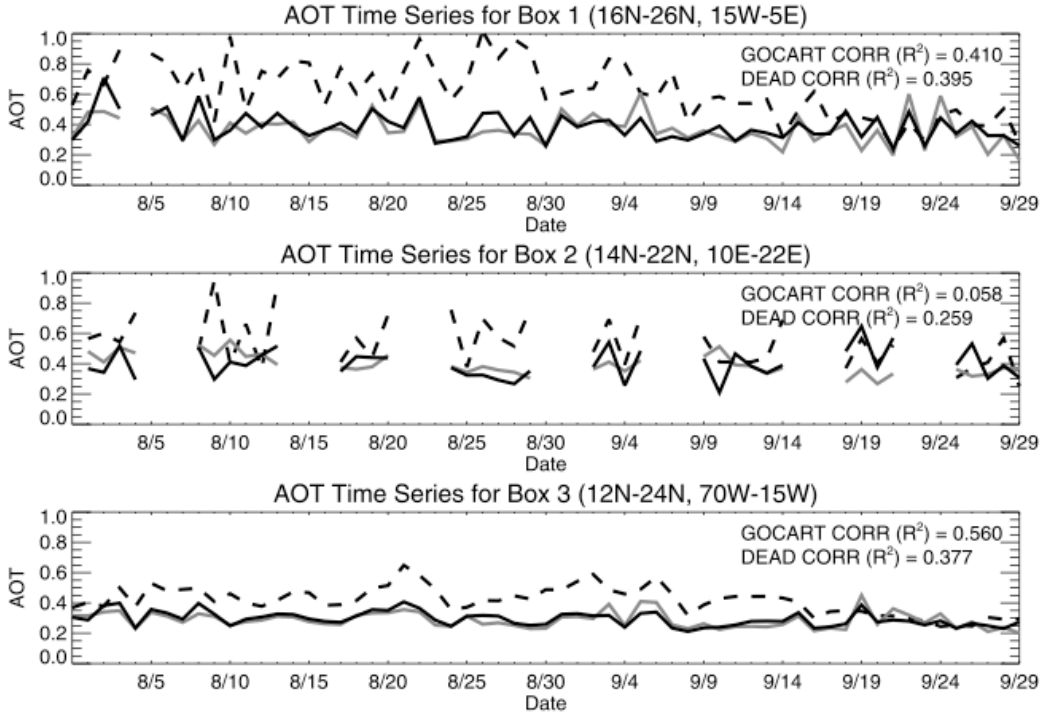

Figure 4.6. MISR (dashed) and sampled GOCART (black) and DEAD (gray) daily AOT for boxes 1 – 3. Coefficients of determination are displayed on the top right of each plot.

4.2.2.2.2 Aerosol Robotic Network

Four AERONET sites are located near the dust source regions in North Africa during the NAMMA period (Figure 4.7). Sites were chose based on their proximity to the source region and availability during the NAMMA period.

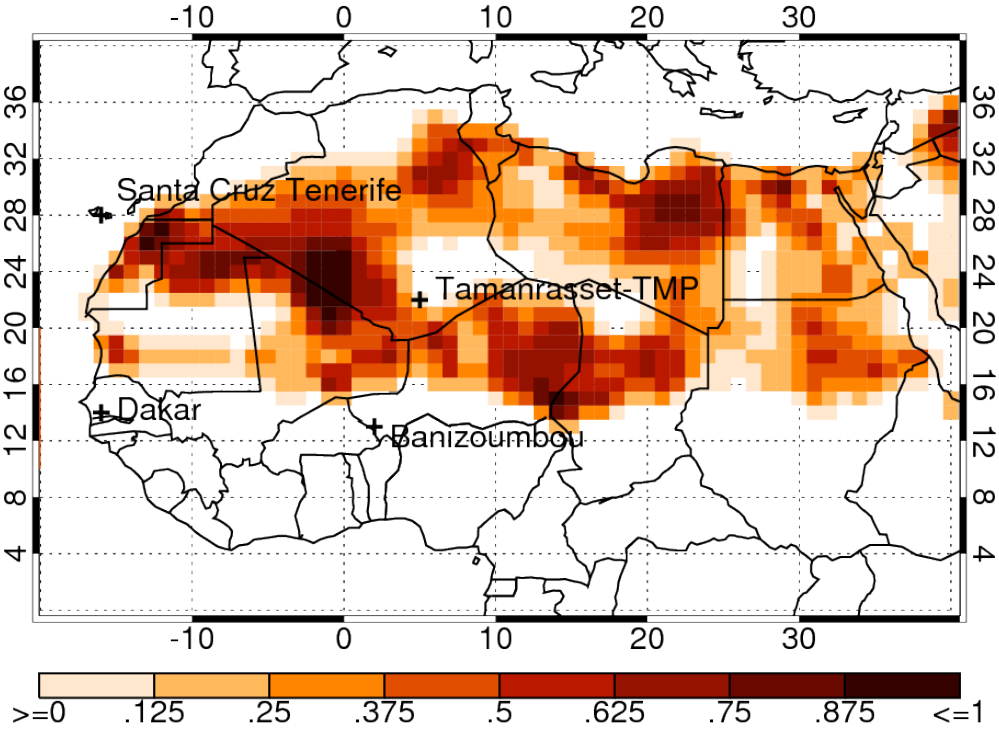

Figure 4.7. AERONET site locations and their proximity to the dust source region (contour).

Figure 4.8 compares daily averaged GEOS-4 GOCART and DEAD AOT values from all aerosols to AERONET AOT. For each site, the mean AOT for AERONET, GOCART, and DEAD on days when AERONET provides retrievals is displayed in the upper left corner and the coefficient of determination (R^2) correlation of the AERONET AOT time series with GOCART and DEAD is displayed in the upper right corner. In general, the two model simulations are well correlated with each other. At Tamanrasset-

TMP (nearest to the large-scale dust source regions) we have a generally low correlation between the model AOT and the AERONET observations (GOCART $R^2 = 0.278$, DEAD $R^2 = 0.333$). Both simulations fail to capture dust events that occur on 8/10, 8/15, and 8/28, artificially simulate a dust event from 9/21 - 9/24, but are able to accurately capture a dust event that occurred from 9/2 - 9/5. These results are consistent with MISR in that the model has difficulty with the timing of dust events near the source region.

Dakar and Banizoumbou are sites peripheral to the dust source region. Similar to Tamanrasset-TMP, the mean AOT is comparable between the model simulations and the AERONET observations at both sites. At Dakar, AERONET reports high AOT values from 8/15 - 8/20, 8/25, 9/5 - 9/9, and 9/21, while GEOS-4 values are never higher than 0.7. Despite the differences in magnitude, the timing of GEOS-4 AOT events has moderate agreement with AERONET (GOCART $R^2 = 0.454$, DEAD $R^2 = 0.387$). At Banizoumbou, there is poor agreement between AERONET and GEOS-4 AOT time records (GOCART $R^2 = 0.101$, DEAD $R^2 = 0.018$). Often there is a lag between simulated and observed AOT values (e.g. 8/20 - 8/25), which result in low correlation coefficients.

Santa Cruz, Tenerife, is downwind of the dust source region and AOT magnitudes are correspondingly lower, yet the periodic passing of dust events is evident. Here, there is relatively high correlation in the timing of events between the model and the observations (GOCART $R^2 = 0.583$, DEAD $R^2 = 0.644$), but mean AOT values are somewhat higher in the model than in the observations.

The simulations have their greatest correlation with AERONET observations downwind of the source region (Santa Cruz, Tenerife), have moderate agreement near the

source region at the Tamanrasset-TMP site and peripheral site Dakar, and poor agreement at Banizoumbou. Over the source region, meteorological observations to constrain the model are scare, so the wind fields that drive the dust emissions are based on the model physics more than on observations. Further from the dust sources, however, it is generally the case that more meteorological observations are available for assimilation into the analyses driving the model, and hence the simulated loadings have better agreement with the observations. Additionally, although there are limitations in the dust emissions schemes, errors in accurately simulating other aerosol types will play a role in the overall fidelity of the simulated AOT with observations. In particular, at Dakar and Banizoumbou inspection of the Angstrom parameter determined from AERONET observations suggests that some significant aerosol events are due to aerosols other than dust (not shown). Alternatively, errors in the timing of events may be attributed to either model spatial scale or (and related) transport errors. AERONET observations are essentially point measurements, while the model grid-boxes are approximately 100 km x 100 km in size. Therefore, the model may not be resolving sub-grid scale plumes that may be driving the AERONET observations. This explanation is plausible, as for each AERONET site, comparisons to the were made once again by averaging the model over the nine grid boxes encompassing and surrounding the site (so considering a box of approximately 300 x 300 km^2 area) and achieved essentially the same results at all four sites (not shown). Therefore, the differences between the model and observations are not simply the result of plume misplacement, but are either a reflection of real errors in the model aerosol parameterization or missing sub-grid scale aerosol plumes. Mean AOT comparisons to AERONET are consistent with MISR in that both GEOS-4 simulations

have better agreement with one another than with the observations during August and September. However, unlike comparisons to MISR, mean simulated AOT values are not consistently low when compared to AERONET. We see that mean AOT values are very comparable to AERONET at Dakar, have good agreement at Tamanrasset-TMP (DEAD) and Banizoumbou (GOCART), and are slightly biased high at Santa Cruz Tenerife.

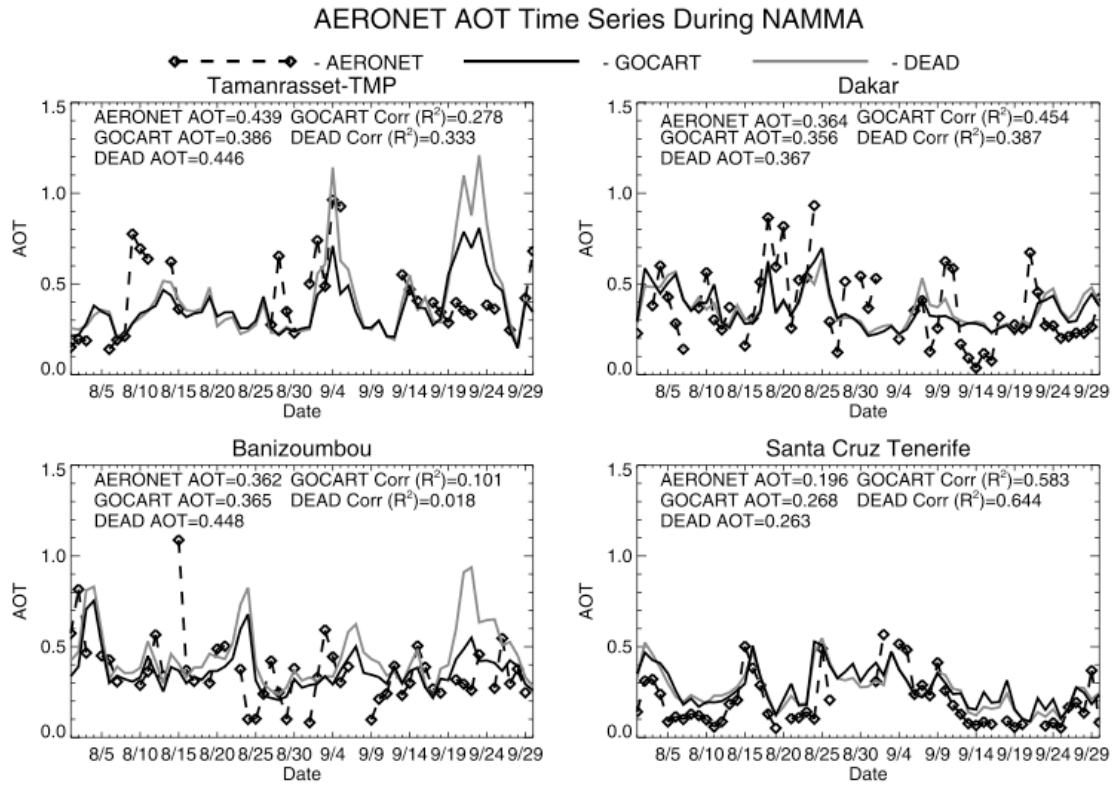

Figure 4.8. AERONET AOT (dashed-diamond), GEOS-4 GOCART AOT (solid black), and GEOS-4 DEAD AOT (solid gray) during August and September. Mean AOT values and coefficients of determination are displayed in the top left and right, respectively.

4.2.2.3 Particle Size Distributions

In this section, modeled dust particle size distributions are evaluated in the context of observations from AERONET and airborne measurements. Recall that the initial particle size distribution is dynamically generated for simulations with GOCART

emissions (wind – speed dependent) but is prescribed for simulations with the DEAD emission scheme. For both schemes, the particle size distributions will evolve during transport as particles are removed via dry and wet removal processes.

4.2.2.3.1 Aerosol Robotic Network

To measure the ability of each emission scheme to simulate dust particle size distributions, simulated size distributions were compared to those retrieved at the Tamanrasset-TMP, Santa Cruz Tenerife, Dakar, and Banizoumbou AERONET sites (Figure 4.7). Here, *only* simulated dust particle distributions are compared to AERONET retrievals. At each site during August and September, the daily averaged AERONET size distribution is constructed from observations where the AOT is greater than 0.4 at 440 nm [Dubovik and King, 2000]. From the daily averaged size distributions, a mean size distribution is constructed for the August-September period at each site. The simulated particle size distributions were computed at each vertical level in the model from the simulated mass distributions, and the values were integrated in the vertical to produce a column-integrated volume distribution, consistent with the AERONET retrieval.

Shown in Figure 4.9 are the mean August-September volume distributions for AERONET and the two model simulations at each site. On each AERONET volume distribution, the standard deviation of each particle size bin is indicated. In addition to the volume distributions, the mean total AOT, coarse mode AOT, and the coarse mode volume median diameter (retrieved in AERONET, from the dust mode in the model) are shown for the AERONET observations and the GEOS-4 GOCART and DEAD simulations, as well as the number of days used to determine the averages. At

Tamanrasset-TMP only one day was available, and both simulations underestimate the AOT, and therefore the overall particle volume. Additionally, the simulations underestimate the relative contribution of large particles to the overall volume and the model coarse mode median diameter is underestimated relative to the AERONET retrieval. Because there is only one valid day during our time of interest, it is difficult to tell if this large discrepancy between the AERONET and GEOS-4 volume distributions is a common occurrence. Moving away from the source region to the Santa Cruz Tenerife, Dakar, and Banizoumbou sites, there is better agreement between simulated and AERONET coarse-mode distributions. Due to their location downwind of the dust source region, AERONET distributions are narrower and AERONET coarse mode median diameters are smaller (at Dakar and Santa Cruz) as larger particles settle preferentially from the dust plume. However, the model coarse mode median diameters do not exhibit much variability from one site to the other, which could indicate that the simulated removal processes are not reflective of the regional atmospheric environment.

In the submicron range, AERONET volume distributions have a second mode that is not seen in the simulated dust volume distributions at all locations. This feature is due to the presence of smaller, non-dust aerosols (e.g. smoke) that are not being considered in the comparison to simulated dust volume distributions. Regardless of the aerosol type, this comparison suggests the current range of aerosol diameters be extended below 0.2 μm in diameter in future simulations, as this mode will have important implications for simulated optical quantities. Comparing the two simulations in the submicron range, there are a greater number of particles in the DEAD volume distributions when compared to the GOCART volume distributions, a feature consistent with Figure 4.4. At all three

sites, the AERONET volume distributions peak near 4μm. Both emission schemes have comparable coarse mode volume median diameters, but the DEAD volume distributions consistently result in larger median diameters that are more comparable to AERONET.

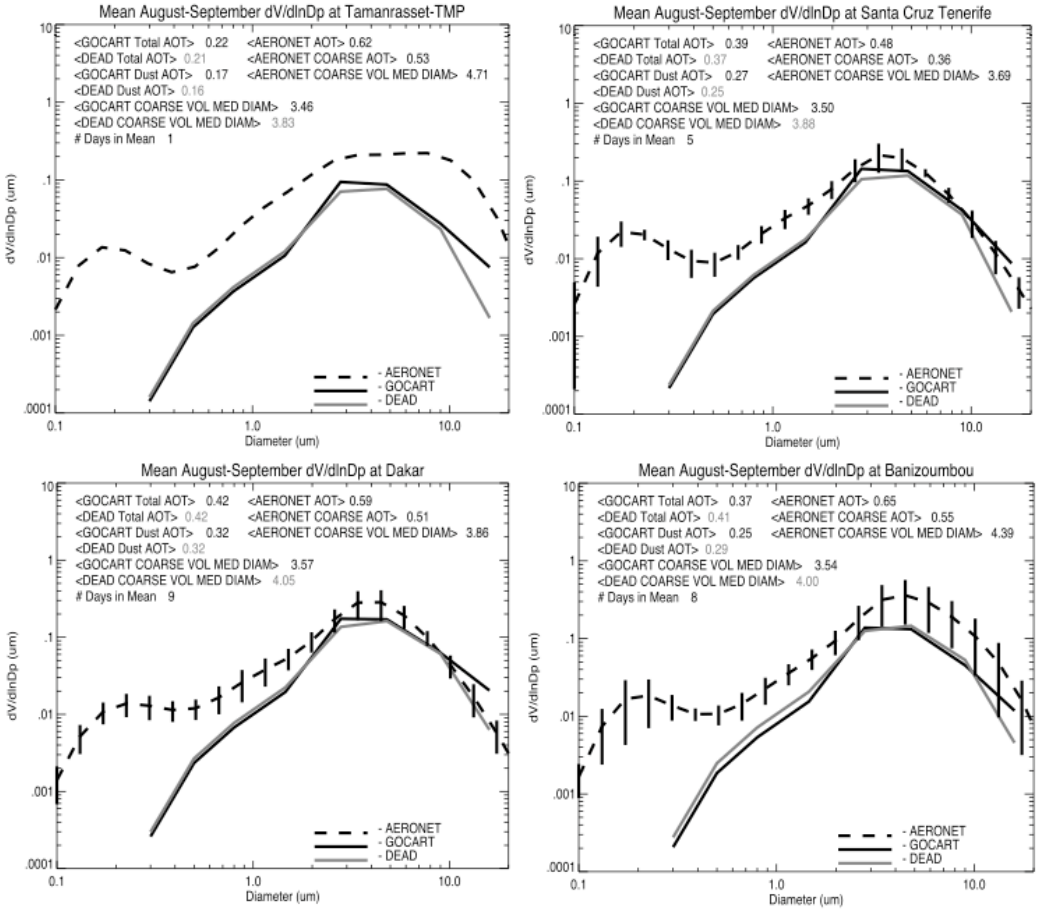

Figure 4.9. Mean August – September AERONET (dashed), GEOS-4 GOCART (solid black), and GEOS-4 DEAD (solid gray) size distributions.

4.2.2.3.2 Airborne *In Situ*: Langley Aerosol Research Group Experiment

During NAMMA, the Langley Aerosol Research Group Experiment (LARGE) airborne payload provided *in situ* measurements (Chapter 2.2.3.1) of particle size distributions while flying on the NASA DC-8 aircraft. The observed dust size

distributions exhibited a bi-modal structure that was fitted with two lognormal curves to produce the smoothly varying size distributions. For our analysis, our simulated volume distributions are compared to 28 in-situ volume distributions at varying altitudes and locations during NAMMA.

Figure 4.10 shows volume distributions from LARGE and both GEOS-4 simulations (dust-only) on 8/19/2006 and 8/25/2006. On each day, the locations of the sampled distributions along the DC-8 track and their proximity to the MODIS-Aqua and GOCART AOT are shown. Additionally, the mean fitted distribution as well as the range of distributions possible based on the standard deviations of the fitted size parameters for a range of altitudes (1.5-2.25, 2.25-3, 3-3.75 km) are shown. On 8/19/2006, while descending into a dust plume, several volume distributions were collected over the tropical North Atlantic Ocean in the area of 14-16.5° N, 21-27° W. With increasing altitude, the *in situ* volume distributions become narrower as the number of large particles decrease with altitude. Both GEOS-4 distributions exhibit little variability in the vertical, hinting again that the removal processes may be too relaxed in the model. Additionally, in contrast to the comparison to AERONET, both simulations have peak volumes at larger diameters ($D \sim 4$ μm) than the measurements ($D \sim 2$ μm). Because only the dust contribution to the total volume distribution is compared to the LARGE data, it is not surprising that both simulations do poorly in the submicron range. However, a significant discrepancy exists between all LARGE distributions and the simulated distributions in the range of $1 < D < 2$ μm, where the DEAD scheme is only marginally better. On 8/25/2006, *in situ* volume distributions were collected during aircraft ascent in the vicinity of 18.5-20° N, 18.5-23° W. On this day, both model simulations better

capture the variations in particle size with altitude and show an improved agreement with the airborne measurements in the 1 μm < D < 2 μm diameter range, but exhibit modal diameters that are about 2 μm greater than seen in the LARGE distributions. It should be noted that the *in situ* measurements were not corrected for hygroscopic growth or for losses within the sample inlet, possibly accounting for a part if not all of the observed differences in the coarse mode size range.

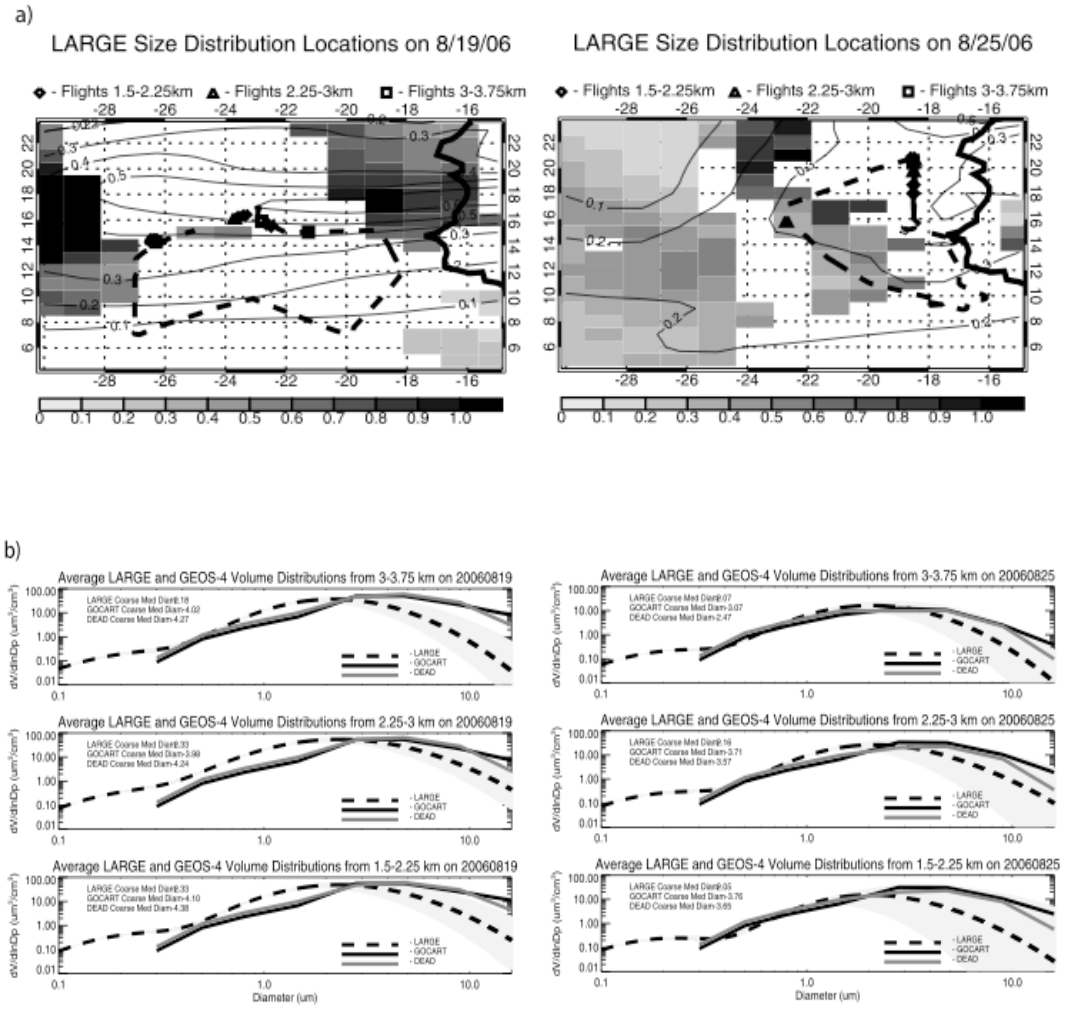

Figure 4.10. (a) *In situ* volume distribution locations along the NASA DC-8 track (dashed line) over daily averaged MODIS Aqua (shaded) and GOCART (contoured) AOT on 19 August 2006 and 25 August 2006. Mean *in situ* (dashed), GOCART (solid black), and DEAD (solid gray) volume distributions as a function of altitude on (b) 19 August 2006 and 25 August 2006.

4.2.2.4 Aerosol Vertical Profiles

During NAMMA, the LASE lidar also flew onboard the NASA DC-8 aircraft. LASE operated during all 13 NAMMA flights and obtained aerosol measurements where cloud attenuation effects were not significant. LASE aerosol extinction profiles have been shown to have very good agreement with aerosol extinction profiles derived from simultaneous *in* situ LARGE data [Ismail et al., 2009]. LASE, along with observations from the space-based CALIOP, are used to evaluate the simulated dust vertical profiles during the NAMMA field campaign. The horizontal distribution of aerosols is additionally considered in the context of correlated aerosol observations from the MODIS-Aqua and OMI satellite sensors. The CALIOP, MODIS-Aqua, and OMI observations are near coincident in time, with all three instruments operating on separate satellites flying within a coordinated satellite constellation (the so-called A-Train). Here two case studies are considered where the satellite and airborne observations are correlated.

The NAMMA flight on 8/26/06 (Figure 4.11) is representative of other NAMMA flights, as observations are made over the ocean under similar synoptic conditions while the NAMMA flight on 9/5/06 (Figure 4.12) is unique as the DC-8 aircraft made way over the African continent. For each NAMMA flight presented, the DC-8 track is shown in the top left plot by the black line. The '□' marks the beginning of the flight and an 'X' marks the end. In addition to the flight track, the Lidar Atmospheric Sensing Experiment (LASE; Chapter 2.2.3.2) extinction [815 nm] is compared to sampled GEOS-4 GOCART and DEAD extinction from all aerosols [815 nm] in the left column. GEOS-4 grid cells were sampled at the nearest model synoptic time along the DC-8 track. The DC-8

altitude is indicated in the LASE and GEOS-4 curtain plots with a solid black line. Also shown on the top left plot is the CALIOP nighttime pass (solid red line) that is nearest the DC-8 flight track. The beginning of each CALIOP track is marked by a '□' and the end is marked by an 'X'. In each center column, CALIOP total attenuated backscatter [532 nm], CALIOP depolarization ratio [532 nm], GEOS-4 GOCART from all aerosols extinction [532 nm], and GEOS-4 DEAD extinction from all aerosols [532 nm] are shown. Both GEOS-4 simulations are sampled along the CALIPSO track similar to the DC-8 sampling. In the right column, OMI aerosol index [354 nm], MODIS-Aqua AOT [550 nm], GEOS-4 GOCART AOT from all aerosols [550 nm], and GEOS-4 DEAD AOT from all aerosols [550 nm] are plotted to identify spatial distributions of observed and simulated dust plumes.

4.2.2.4.1 26 August 2006

At 1300Z on August 26, the NASA DC-8 encountered an intense low-level dust plume (Figure 4.11). The aircraft ascended to 10.5 km as it headed in a northwest direction. Upon reaching 20° N, the aircraft maintained a steady altitude of 10.5 km and changed course to follow a counterclockwise path above a low-level dust plume over the tropical North Atlantic Ocean. Near 18° N, the aircraft briefly dipped down to 7 km but quickly ascended to 11 km for the second half of the flight before returning to Capo Verde.

On this day, simulated extinction profiles from both emission schemes are nearly identical. Both GEOS-4 simulations are very similar and match well with LASE extinction beneath 4 km. Above 4 km, model extinction values continue to be high up to

6 km, where LASE is generally capped at 4 km. While CALIOP appears to show an elevated dust plume on its transit, both instances of the model show a dust layer that extends to the surface and situated somewhat more to the south. On the other hand, the peak AOT in the model appears to be near the surface and coincident with marine stratus clouds CALIOP observations (high backscatter and modest depolarization below about 2 km altitude extending along the northern portion of the transit), indicating that the model is able to capture swelling by hygroscopic aerosols within the humid marine environment. Although the OMI and MODIS observations are not time coincident with the CALIOP data and apparently miss the DC-8 flight on this day, both instances of the model place dust plumes consistently with their observations over North Africa and the Canary Islands, but underestimate the AOT.

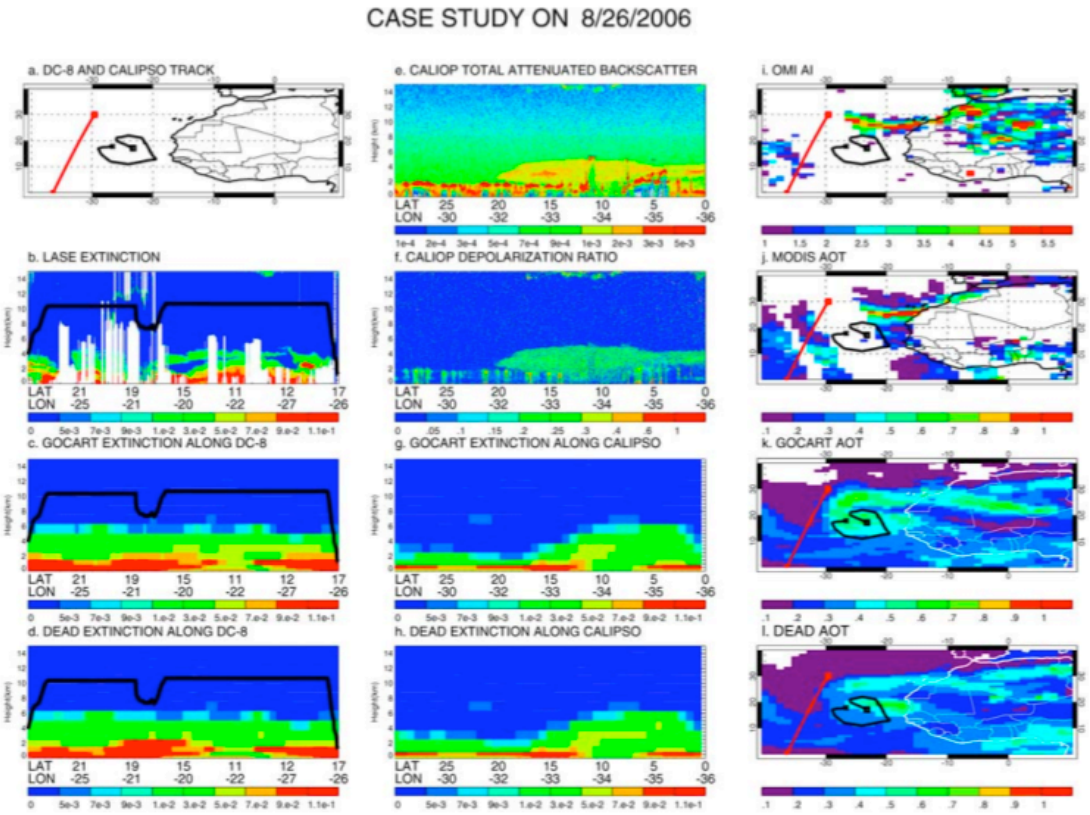

Figure 4.11. NASA DC-8 (black) and CALIOP (red) (a) tracks, (b) LASE extinction, (c) GEOS-4 DC-8 sampled GOCART extinction, (d) GEOS-4 DC-8 sampled DEAD extinction, (e) CALIOP total attenuated backscatter, (f) CALIOP depolarization ratio, (g) GEOS-4 CALIOP sampled GOCART extinction, (h) GEOS-4 CALIOP sampled DEAD extinction, (i) OMI Aerosol Index, (j) MODIS-Aqua AOT, (k) GEOS-4 GOCART AOT, and (l) GEOS-4 DEAD AOT on 26 August 2006.

4.2.2.4.2 5 September 2006

On September 5, the NASA DC-8 began a flight at 1200Z (Figure 4.12). During the flight, the aircraft increased altitude to a steady 11 km as it flew northeast to 19° N and then maintained constant latitude as it flew over the continent to 10° W over an intense dust plume. The aircraft then spiraled down into the dust plume to 1 km, then turned around and followed the same path back Capo Verde while slowly ascending to 8 km. This flight is unique because it is one of the few NAMMA flights that were conducted over land.

On this day, both schemes have excellent agreement with the LASE extinction profile. Unlike the previous case study illustrated, both emission schemes transport dust to altitudes comparable to those retrieved by LASE. CALIOP total attenuated backscatter and depolarization ratio show a strong elevated dust plume extending from 30° N to 10° N. We note that the strong backscatter signals seen above 5 km are indicative of ice clouds due to their high altitude, heterogeneous structure, polarization of the backscatter signal at the feature altitude, and complete attenuation below. These clouds are not shown in the model results. Both schemes capture the elevation and latitudinal extent of the dust plume observed by CALIOP. OMI AI and MODIS AOT show dust plumes over northern Africa and off the coast of Mauritania. Both simulated plumes are positions slightly to the north and east of each observed plume. MODIS tropical North Atlantic AOT spatial distributions and magnitudes are comparable to both schemes.

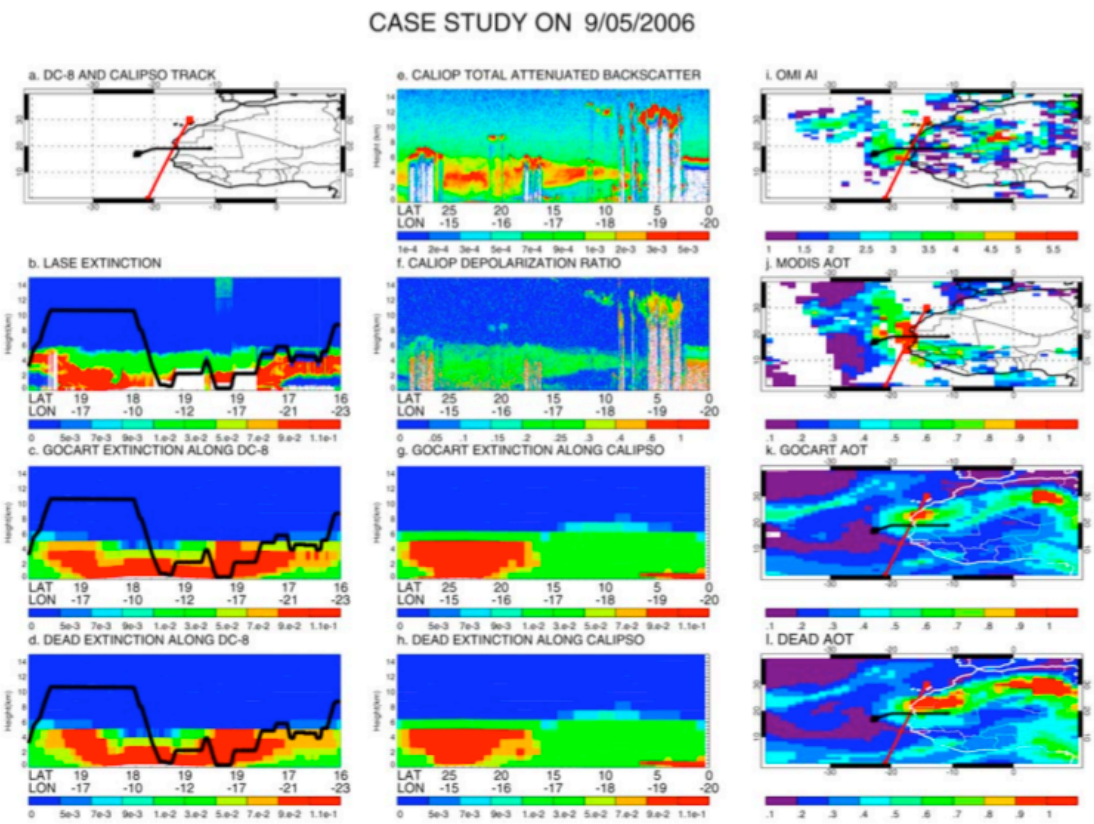

Figure 4.12. NASA DC-8 (black) and CALIOP (red) (a) tracks, (b) LASE extinction, (c) GEOS-4 DC-8 sampled GOCART extinction, (d) GEOS-4 DC-8 sampled DEAD extinction, (e) CALIOP total attenuated backscatter, (f) CALIOP depolarization ratio, (g) GEOS-4 CALIOP sampled GOCART extinction, (h) GEOS-4 CALIOP sampled DEAD extinction, (i) OMI Aerosol Index, (j) MODIS-Aqua AOT, (k) GEOS-4 GOCART AOT, and (l) GEOS-4 DEAD AOT on 5 September 2006.

4.2.3 Summary and Conclusions

In this chapter, comparisons of simulated dust distributions to several observation data sets obtained during the NAMMA field experiment were presented. GEOS-4 simulations were conducted with two different dust aerosol emission schemes. Both schemes used the same source function map to locate dust source regions but differed in their underlying parameterization of the emission process. The emission schemes were tuned so that the regionally averaged dust AOT over North Africa during the August—September 2006 period was the same for each.

The impact of the emission scheme choice is most clearly seen in the mass distributions of emitted dust. The GOCART scheme more broadly distributes emission over the source region, whereas the emissions in the DEAD scheme are more localized (Figure 4.2). This difference is related to the differences in the treatment of the dust mobilization processes in the schemes. In the DEAD scheme, emissions are highly sensitive to the presence of soil moisture and are driven by the wind friction speed, which is comparable in magnitude to the wind speed threshold for emissions, and therefore emissions are more episodic. In contrast, the GOCART scheme drives emissions by the 10-m wind speed, which even when the effects of soil moisture are considered, is typically an order of magnitude greater than the threshold wind speed, and so the wind speed threshold is more frequently exceeded throughout the domain. Additionally, although the two schemes were tuned to yield the same regional AOT values, differences in the choice of emitted particle size distribution result in different emission magnitudes (91 Tg/month for GOCART scheme vs. 54 Tg/month for DEAD scheme). More mass in the GOCART scheme is emitted into larger particle sizes that have shorter residence times because of removal by gravitational settling, while the DEAD scheme has relatively more mass emitted into smaller, more optically efficient particles and fewer large particles (Figure 4.4). Despite these differences in the emitted particle size distribution, both schemes evolve similar particle distributions during transport (Figures 4.9 and 4.10). Comparing simulated particle size distributions to AERONET measurements (Figure 4.9) there is poor agreement between the simulated and retrieved distributions near the source region (Tamanrasset-TMP), and the observed relationship between smaller particle sizes and the coarse mode with distance downwind of the source

regions was not accurately captured. The DEAD scheme had somewhat larger coarse mode median diameters, which agreed slightly better with AERONET. In general, both schemes maintained fairly constant particle size distributions during transport.

Comparisons of GOCART and DEAD AOT values to observations from MISR (Figure 4.5) show that both schemes produce similar spatial distributions of dust downwind of source regions, but different distributions over the source region. The implication is that while the downwind distributions may evolve similarly in both schemes, the radiative forcing due to the dust over the source region might be quite different.

In comparison to AERONET AOT observations (Figure 4.8), GOCART and DEAD AOT are highly correlated with each other in time, but differ somewhat in magnitude, especially during high AOT events, which is not inconsistent with the MISR observations discussed above. Both MISR and AERONET show that neither emission scheme performs especially well over the source region at capturing specific events. To the south of the source region, daily AERONET AOT correlations with each scheme are also poor, but MISR monthly mean AOT values are comparable. This suggests that the timing of specific dust transport episodes to the south of the source region may not be correct, but the mean pattern is comparable to the observations. Both schemes have their best agreement with MISR and AERONET AOT farther downwind of the source region (Santa Cruz, Tenerife) and over the tropical North Atlantic Ocean. This suggests that the meteorology over the source regions may not be sufficiently accurate to capture specific dust lifting events, but that once dust is entrained in the large-scale flow downwind of sources the model is adequate to resolving dust transport episodes. This result is

consistent with Colarco et al. [2003], who showed that the timing of dust events is more sensitive to transport dynamics rather than the dust model chosen.

Simulated vertical profiles from both schemes were compared to NAMMA airborne observations and space-based CALIOP observations for two case studies. To our knowledge, this is the first time that dust vertical distribution has been explored in the same model running with different dust emission schemes. In both cases, the model did a reasonable job of placing the dust plumes from Africa over the tropical north Atlantic, and in general there was no apparent difference in the vertical plume placement between the schemes. In one of the cases examined (August 26, Figure 9), although the model had located the main dust plume correctly below 4 km altitude, there was considerable transport of dust at higher altitudes as well. There are well known issues of excessive vertical diffusion in numerical transport models that result from limited vertical resolution. Further sensitivity studies will be required to isolate that possible cause from errors in the vertical mixing by dry convection over the source region or even long-range transport of dust from distant source regions as explanations for simulated dust at too high an altitude and are outline in Chapter 6.2.

The GOCART and DEAD emission schemes produce similar AOT distributions during the timeframe of the NAMMA field experiment. From a physical standpoint, the DEAD emission scheme poses a more realistic representation of dust emission by correctly comparing the surface friction speed to the threshold speed and simulating particle saltation. However, emitted dust distributions are dependent on several unknowns such as soil particle size distributions, soil clay content, and model assumptions that are used to compute the surface friction speed. Additionally, the 10-

meter wind speed used by the GOCART scheme to parameterize dust emission is typically is observed more frequently than the surface friction speed, though observations over the Saharan source region are sparse.

Despite the differences in the emission schemes, both simulations become more comparable to observations with distance from the source region. Because observations are limited within the source region and dust production is subject to the accuracy of the assimilated meteorology, it is not surprising that the largest discrepancies exist in this region. Therefore, for this set of model simulations, errors in the simulated meteorology may be more significant than the differences between the emission schemes. From the analysis of observed and simulated dust distributions, emission scheme choice makes a small difference when considering the particle size distributions of the load. Based on the available AERONET and airborne *in situ* size distributions during the NAMMA experiment, the fixed particle size distribution chosen for the DEAD scheme produces a particle size distribution that is slightly more comparable to observations. Using optical measurements over North Africa during the NAMMA experiment, there were not any significant advantages or disadvantages of using either scheme. However, the significant difference in emitted particle size distributions and corresponding mass between the emission schemes over the source region may be useful to identify which scheme is more preferable for global model use if there are sufficient observations of mass concentrations during NAMMA. Additionally, while changing the region or time period of interest may help to differentiate the schemes, it is expected that the most significant difference will be seen if the model resolution is increased. If the micro-scale processes and meteorology that control dust emission are better resolved, there can be a large effect on simulated

emitted dust distributions owing to the subtle differences of the emission schemes. These effects will be further explored in the next section.

4.3 Sensitivity of The Mobilization Process to Model Physics

One of the major findings from Section 4.2 was that modifying the physics of the dust mobilization process did not have a significant impact on downwind distributions in GEOS-4. This was true despite large differences in the spatial distribution of dust emissions and the emitted particle size distributions. Here, the sensitivity of these conclusions to model spatial resolution is explored using the NASA GEOS-5 model (Chapter 2.1). GEOS-5 can be run for various applications at a range of spatial resolutions from relatively coarse resolutions typical of long integration climate simulations (2°×2.5° and 1°×1.25° latitude by longitude) to higher resolutions more useful in data assimilation and short-term operational forecasting (0.5°×0.625° and 0.25°×0.3125°), hereby referred to as 2°, 1°, 0.5°, and 0.25°.

Here, the objective is to investigate the sensitivity of dust emissions and the dust aerosol lifecycle to spatial resolution in order to homogenize simulations across this range of spatial scale. Ultimately, the simulated dust aerosol lifecycle will influence AOT distributions, which are compared to satellite observations to determine appropriate tuning constants (see Chapter 3.1).

In this section, the effects of changes to the driving dynamics, source function resolution, and model spatial resolution on simulated dust emissions, particle size distributions, lifetime, and AOT are explored in GEOS-5. These effects are explored globally, as well as over the African (13° N - 35° N, 18° W - 35° W) and Asian (36° N -

44° N, 77° W - 109° W) source regions (Figure 4.13). This analysis is focused on the month of April 2008, in order to utilize data provided by the NASA SMART-COMMIT field campaign near the Gobi Desert in Zhangye, China (Chapter 2.2.3.4) in addition to AOT observations from MISR and AERONET (Chapter 2.2.1.2 and 2.2.2.1).

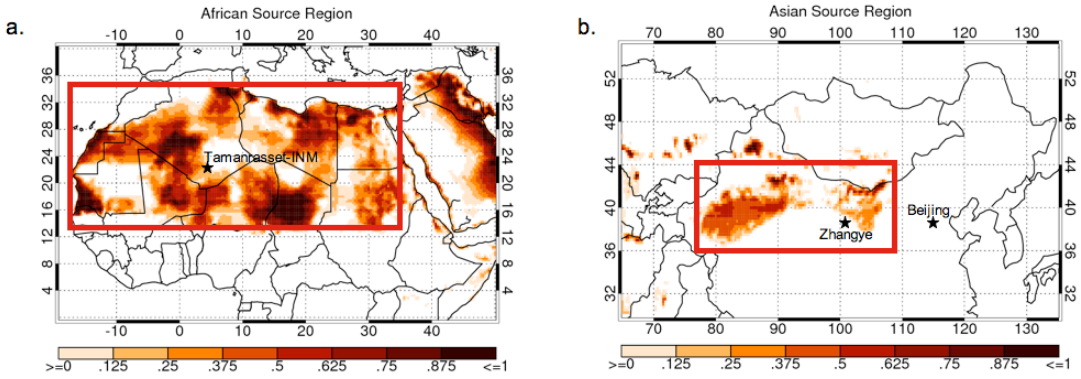

Figure 4.13. African (a) and Asian (b) source regions indicated by red boxes.

4.3.1 Experiment Setup

To explore the sensitivity of dust emissions, lifetime, and AOT, three different mobilization schemes are considered: GOCART, DEAD, and a version of the GOCART scheme that uses a constant threshold speed (hereby referred to as GOCART-threshold). Both the GOCART and DEAD scheme setups are as described in Chapter 4.2.1. The GOCART-threshold setup follows from [Grini and Zender, 2004] and is a somewhat more physically based version of the GOCART scheme. The GOCART-threshold scheme extrapolates the surface dry threshold speed of a 100 μm soil particle as used by the DEAD scheme (0.2 m s^{-1}, Figure 4.1) to 10 meters (6.5 m s^{-1}), assuming neutral atmospheric stability. In this way, the GOCART-threshold scheme attempts to connect dust emissions parameterized in terms of the 10-meter wind speed to the surface by

extrapolating the threshold speed required for saltation to the altitude of the driving meteorology. Additionally, using this method, the order of magnitude of the winds that drive dust emission is the same as the threshold. The constant dry threshold speed is then modified for the presence of soil moisture and uses the same source fractions as the original GOCART scheme (Chapter 4.2.1).

The three different mobilization schemes (GOCART, GOCART-threshold, and DEAD) were run at four different spatial resolutions in order to investigate sensitivity of emissions to model spatial scale. It should be noted that the model time step is a function of spatial resolution, as shorter time steps are required at higher spatial resolution in order to satisfy stability in physics algorithms used in the model. Dust emissions and meteorological parameters needed to compute dust emissions offline were output at the model native time step for each resolution (Table 4.2). Table 4.2 also shows the number of global grid boxes (latitude by longitude) at each, as well as the number of 0.25° grid box within a single grid box at each resolution. In all simulations, a higher resolution (0.25°) version of the dust source from Section 3.1 is used, although it is conservatively interpolated to the appropriate resolution for each.

Resolution	**2°**	**1°**	**0.5°**	**0.25°**
Time Step	30 minutes	30 minutes	20 minutes	15 minutes
Number of Grid Boxes (latitude by longitude)	144 x 91	288 x 181	576 x 361	1152 x721
# of 0.25° Grid Boxes Contained	64	16	4	1

Table 4.2. Model spatial resolutions, output frequency, total number of grid boxes, and number of 0.25° grid boxes within a single grid box at each resolution.

To summarize, three different simulation setups (GOCART, GOCART-threshold, and DEAD) are considered at four different spatial resolutions. As a baseline, each of the mobilization schemes was run for all of 2008 at 2° resolution. The simulations were tuned (see Chapter 3.1) a posteriori so that each had the same global, annually averaged dust AOT as the baseline GOCART run. Emissions for simulations at higher spatial resolution were determined using the same tuning constants, so that only the resolution of driving dynamics, soil moisture, and source function would cause variations in the simulated dust emission as the model spatial resolution was increased. Because simulations at higher resolutions require more computational resources, only April 2008 was simulated at 1°, 0.5°, and 0.25° resolutions to encompass the time period of the SMART-COMMIT field campaign in Zhangye, China (Chapter 2.2.3.4). It should be noted that for all sensitivity simulations, only the dust emission process was modified and that removal processes and optics for all schemes are the same as described in Chapter 3.2 and 3.3.

4.3.2 Results

4.3.2.1 Annual Dust Emission and Aerosol Optical Thickness Cycle

Shown in Figure 4.14 are monthly mean global dust emissions and average AOT for the three mobilization schemes. Globally, emissions from the GOCART and GOCART-threshold setups produce the same seasonal cycle, but the GOCART-threshold

emissions are lower in magnitude and exhibit slightly more month-to-month variability. This is a direct result of the differences in the mobilization parameterizations between the two schemes. Recall that in the GOCART scheme, the threshold speeds required for mobilization have a dependence on size. From Figure 4.1, within the range of simulated dust aerosol diameters (0.1 – 10 μm), the dry threshold wind speed decreases with particle diameter, therefore favoring the emission of heavier, less optically efficient dust aerosols in the GOCART scheme. Additionally, instances may occur where the emission threshold was met for larger particles, but not in the sub-micron range, resulting in emission in only a few of the bins. However, in the GOCART-threshold scheme, the threshold does not have a dependence on size and once it is met, emission occurs for all dust particle sizes. Because the dust emissions of each scheme were constrained to obtain the same dust AOT, the GOCART scheme must emit more mass in order to achieve the same optical efficiency as the GOCART-threshold scheme.

In contrast, the DEAD scheme has a very different annual cycle of dust emissions when compared to the GOCART and GOCART-threshold simulations. Aside from April – June, the DEAD scheme has a very different dust emission seasonal cycle and generally emits significantly less mass when compared to the GOCART formulations. The lower magnitude of the DEAD emissions is not surprising as a major result from Chapter 4.2 was that the DEAD scheme emits a lower magnitude of dust than GOCART for the same AOT. What is more surprising is the large monthly variability in the DEAD emissions, ranging from almost 250 Tg in April to less than 10 Tg in November. However, owing to the differences in the treatment of the emitted particle size distributions, the seasonal

cycle of dust AOT in each simulation is much more comparable, though the DEAD scheme exhibits the most variability.

Figure 4.14 also shows the 2008 seasonal dust emission and AOT cycles over the African and Asian source regions. From this breakdown, it is clear that the global dust emission and AOT cycle is dominated by the African source region and again the DEAD scheme exhibits the most seasonal variability. However, over the Asian source region, all simulations have very similar seasonal emission cycles, though at different magnitudes, reflecting differences in the emitted particle size distributions leading to nearly identical seasonal cycles of dust AOT.

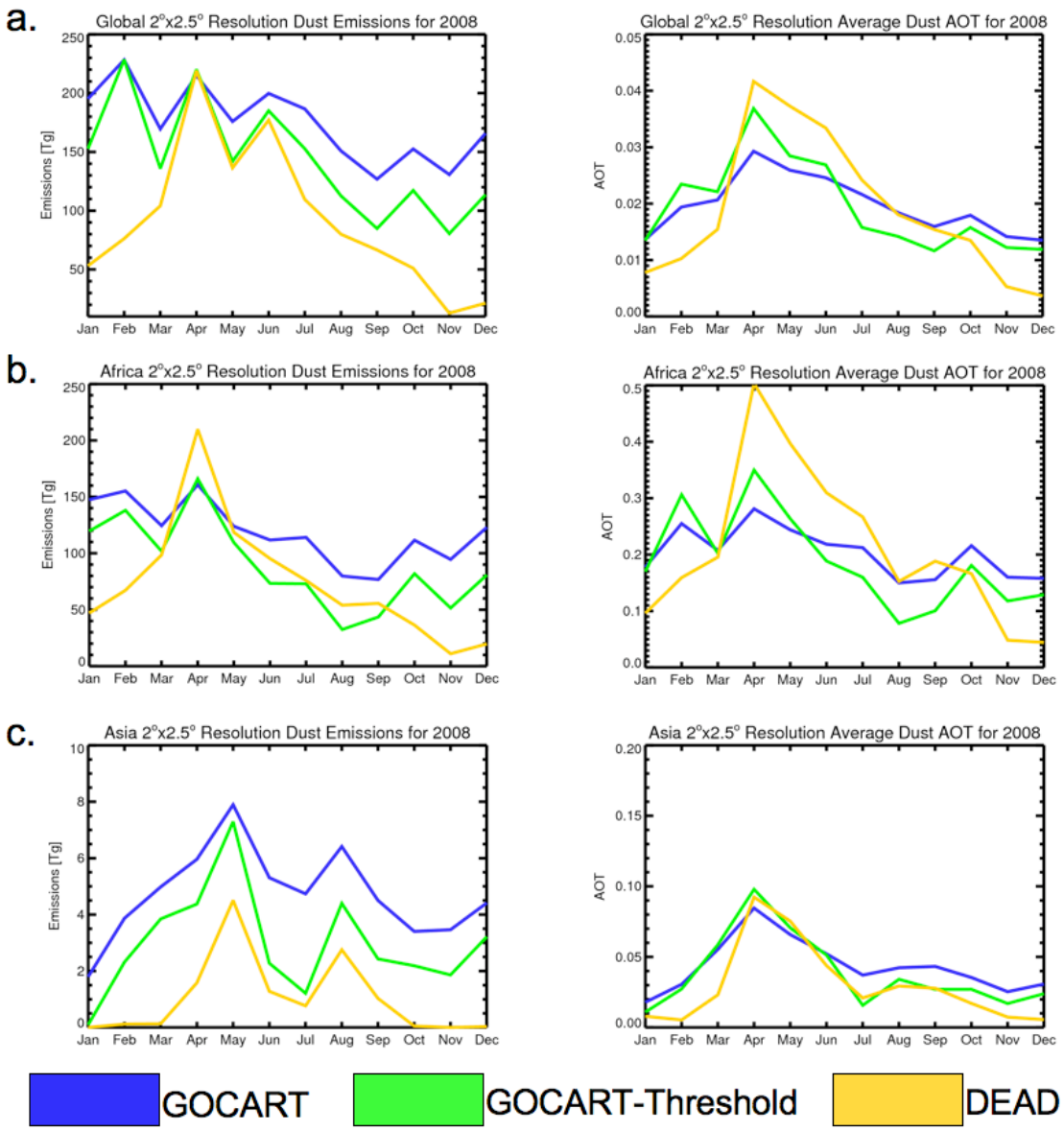

Figure 4.14. (a) Global, (b) African, and (c) Asian monthly mean dust emissions and AOT for 2008 at 2°×2.5° resolution.

4.3.2.2 The Effect of Spatial Resolution on Simulated Dust Distributions

In this section, the effects of model spatial resolution on simulated dust emissions, lifetimes, and AOT distributions are explored during April 2008. At different spatial resolutions, the simulated parameters that are used to parameterize the dust mobilization process (e.g., driving winds) will be resolved differently, potentially having implications

for the simulate dust lifecycle. To illustrate this, Figure 4.15a shows the reverse cumulative distribution function for all GEOS-5 10-meter wind speeds outputted during April 2008, which would be used to parameterize GOCART-based dust emission over the African source region (Figure 4.13). It is clear that as model spatial resolution is increased, simulated wind speed extend to higher magnitudes. Interestingly, the wind speed distribution converges at higher spatial resolutions, as the 0.5° and 0.25° distributions are nearly identical, possibly due to limitations of the native resolution of the MERRA renanalyses (0.5°) or land surface processes that influence simulated surface winds. The reverse cumulative distribution of the surface friction speed over the African source region used to parameterize DEAD emissions is shown in Figure 4.15b. Similar to distribution of the 10-meter wind speed, the surface friction speed distribution extends to higher magnitudes as the spatial resolution is increased and converges at higher spatial resolutions.

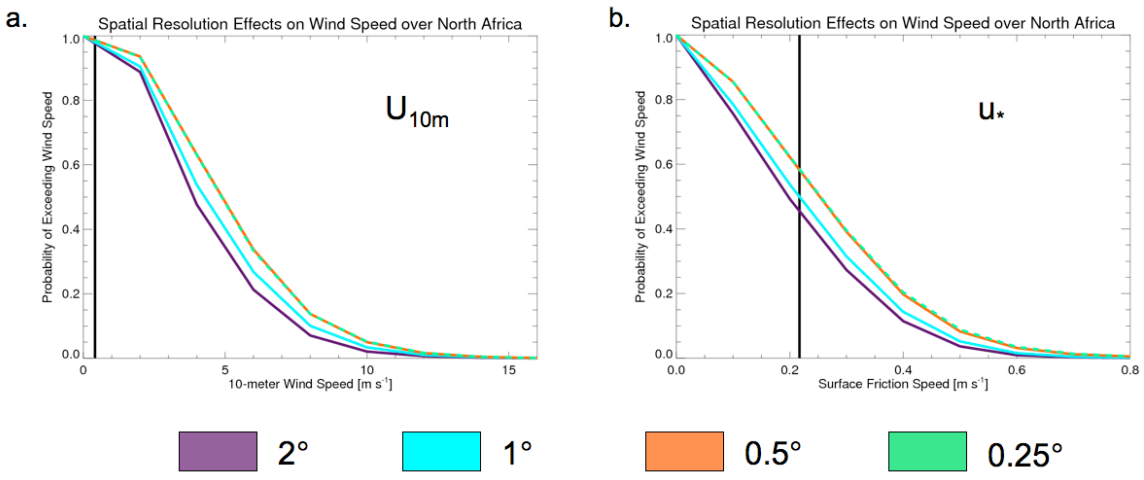

Figure 4.15. April 2008 reverse cumulative distribution functions for the 10-meter wind speed (a) and surface friction speed (b) for all spatial resolutions. Minimum dry threshold wind speeds for dust mobilization in the GOCART and DEAD schemes are indicated by a solid black line on each plot on (a) and (b), respectively.

The relationship between the driving wind speeds and spatial resolution is significant as both dust emission parameterizations have a cubic dependence on the driving winds once the mobilization threshold is met, marked by the solid black line to indicate the minimum wind speeds required for GOCART and DEAD dust emission in Figures 4.15a and 4.15b, respectively. Therefore, based on this example, it is expected that dust emissions will be sensitive to model spatial resolution and will have implications for the simulated dust aerosol lifecycle.

To this point, sensitivity experiments have focused on modifications to the mobilization scheme component of dust emissions. As a subsequent sensitivity experiment, the effect of dust source function resolution on dust emissions is explored. In this setup, a coarse (2°) version of the dust source function is used with original GOCART mobilization scheme to drive dust emissions at all four spatial resolutions, hereby referred to as GOCART-source. Even though GEOS-5 grids the dust source function to the spatial resolution of the model, this is essentially equivalent to using a fixed source function that is insensitive to spatial resolution. In this way, the effect of source function resolution can be quantified by comparing the GOCART and GOCART-source experiments. Additionally, if dust emissions exhibit a strong response due to differences in source function resolution, it will highlight the need for using a source function PDF to capture the effects of strong sources that are not present at coarser resolutions.

To reiterate, all tuning constants for each simulation were set so that each setup had the same 2008 global dust AOT at 2° resolution. Therefore, for a given setup,

differences only will arise from how parameters within each mobilization parameterization are resolved as the model spatial resolution is modified.

4.3.2.2.1 Monthly Emissions

Figure 4.16 shows the April 2008 global total dust emissions for each experiment. It is clear that for all simulation setups, the model spatial resolution has a significant effect on the total emissions. An interesting result is that dust emissions from GOCART-based simulations are highly sensitive to model spatial resolution as it is increased from 2° to 0.5°. However, consistent with Figure 4.15a, GOCART based emissions at 0.25° are comparable to those at 0.5°, as there is a convergence in the 10-meter wind speed distribution. Interestingly, despite nearly identical distributions of the surface friction speed at 0.5° to 0.25° resolutions, the DEAD scheme does not exhibit this convergence, despite a converge of the global surface friction speed (Figure 4.15) and exhibits a linear dependence on model spatial resolution. This suggests that this difference is due to controls on emissions other than the friction speed (e.g. soil moisture). Of all the simulations, the GOCART-threshold setup exhibited the most sensitivity to model spatial resolution. This is a result of the higher threshold being met by higher wind speeds as the model spatial resolution is increased. Finally, the spatial resolution of the dust source function has little impact of dust emissions. Globally, as the model spatial resolution is increased, the GOCART simulation emits more dust than the GOCART-source scheme, though the difference is small and never exceeds 10 Tg.

Also shown in Figure 4.16 are the total dust emissions for April 2008 over the African (4.13a) and Asian (4.13b). It should be noted that other source regions contribute to the total global emissions, but are not considered in this analysis. Because the global emissions are dominated by African dust emissions, it is not surprising that the African results are similar to the global results. Again, the GOCART based simulations exhibit little sensitivity to model spatial resolution beyond 0.5°, the GOCART-threshold setup is the most sensitive to model spatial resolution, and the resolution of the dust source function has little effect on the dust emissions.

Over Asia, all setups exhibit a strong response to model spatial resolution. All setups have a moderate increase in emissions as the resolution is increased from 2° to 1°, but are significantly greater and converge at 0.5° to 0.25°. This indicates that emissions over the Asian source region are more sensitive to model spatial resolution than over the African source region and exhibit non-linear behavior from coarse to high spatial resolution.

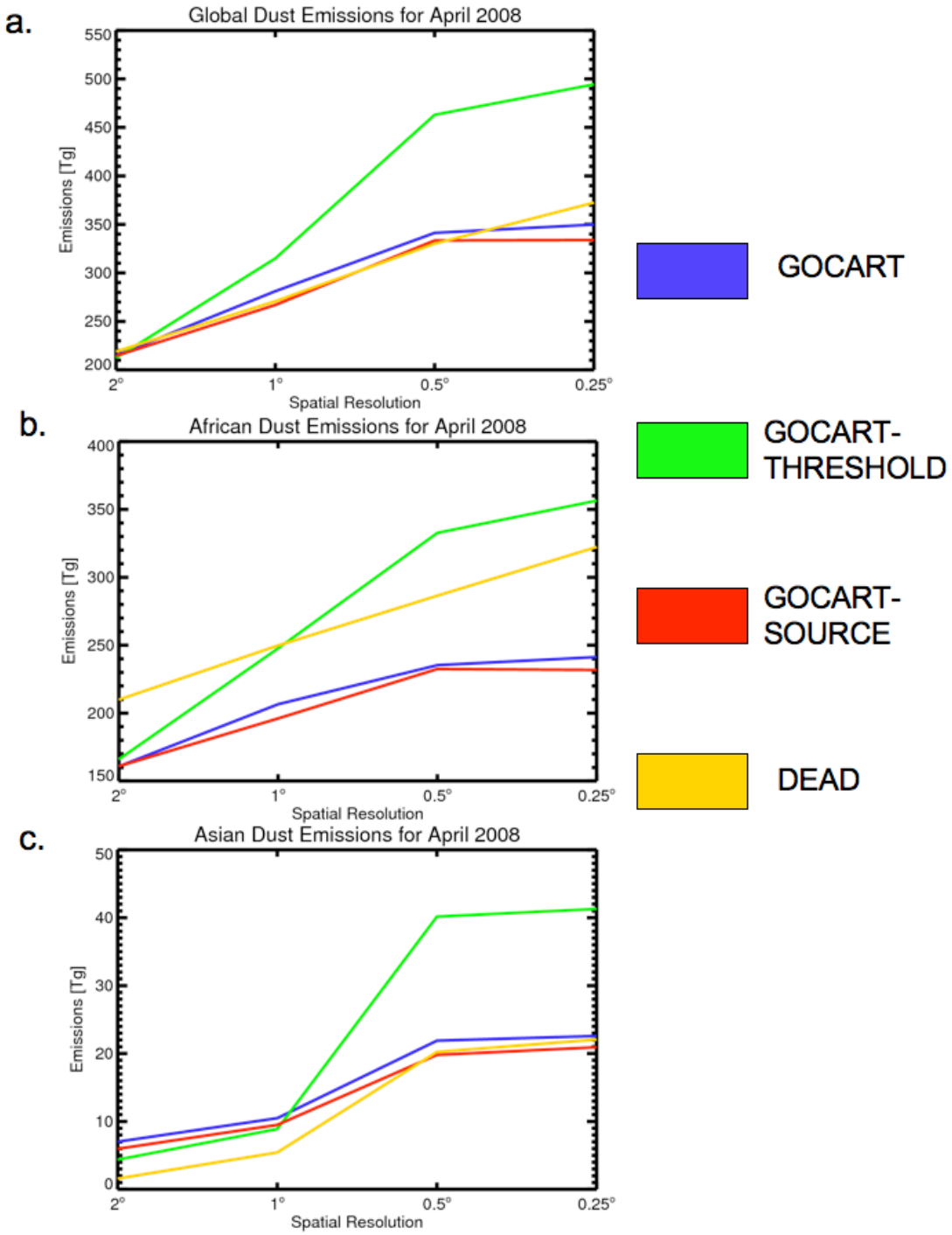

Figure 4.16. (a) Global, (b) African, and (c) Asian monthly mean dust emissions for April 2008 at 2°, 1°, 0.5°, and 0.25° resolutions.

4.3.2.2.2 Diurnal Emission Cycle

Figure 4.17 shows the April 2008 mean diurnal cycle of African dust emissions. For this month, the GOCART (4.17a) and GOCART-source (not shown) simulations simulate similar diurnal cycles of dust emission. Similarly, the DEAD (4.17b) and GOCART-threshold (not shown) simulated diurnal cycles of dust emission are comparable. All schemes are similar in that dust emission peaks just before local noon and have relative minima around midnight.

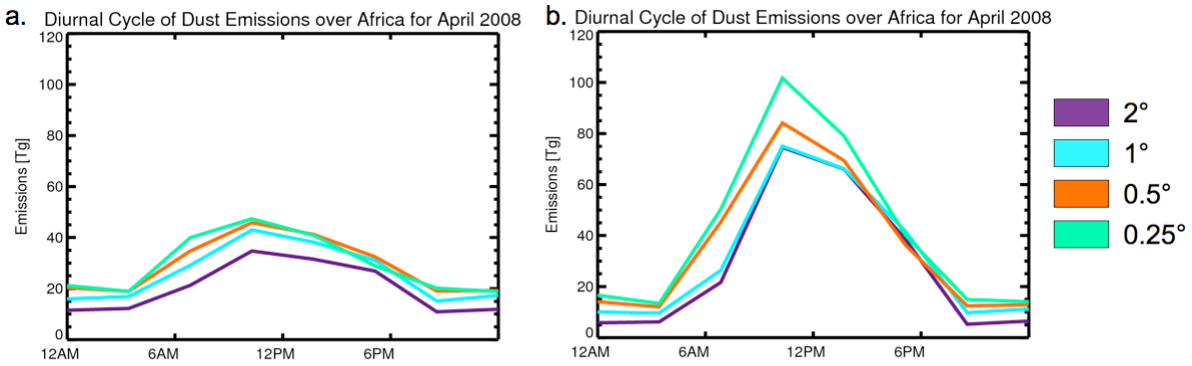

Figure 4.17. April 2008 mean diurnal emission cycle over the African source region for (a) GOCART and (b) DEAD schemes

However, owing to the different formulations of the mobilization process, the GOCART and GOCART-source simulations produce different amplitudes of the diurnal dust emission cycle when compared to the DEAD and GOCART-threshold simulations. This feature is due to the relatively higher thresholds required for emission in the DEAD and GOCART-threshold simulations. Overnight, when winds are generally calmer, the DEAD and GOCART-threshold simulations emit very little dust. Then, during the day, dry convection increases the surface winds, allowing for the mobilization of dust. Conversely, the GOCART and GOCART-source simulated diurnal dust emission cycles

are relatively flat and emit dust overnight, as the 10-meter wind speed easily exceed the required threshold for mobilization (Figure 4.15a). These results are confirmed in Table 4.3, which shows the ratio of the diurnal dust emission maxima to minima for each simulation. Clearly, the DEAD and GOCART-threshold simulations exhibit the greatest diurnal variability. Additionally, the ratio decreases with model spatial resolution for all simulations, indicating that increases to the surface winds are mobilizing dust particles at times when the coarse resolution surface winds were too low to meet the threshold.

AFRICA	**2°**	**1°**	**0.5°**	**0.25°**
GOCART	3.19	2.85	2.54	2.42
DEAD	14.2	7.86	7.60	6.98
GOCART-THRESHOLD	10.51	7.3	6.03	5.35
GOCART-SOURCE	3.42	2.94	2.90	2.45
ASIA				
GOCART	7.71	5.44	2.04	1.99
DEAD	9.17	7.08	5.13	4.01
GOCART-THRESHOLD	8.28	6.78	4.36	3.86
GOCART-SOURCE	6.48	5.70	2.69	2.18

Table 4.3. Ratio of diurnal emission cycle maxima to minima for all simulations and resolutions over the African and Asian source regions.

Over the Asian source region, all simulations exhibit similar diurnal cycles of dust emission. Figure 4.18 shows the diurnal cycle of dust emissions for the GOCART scheme over the Asian dust source region for April 2008. Compared to the African diurnal cycle, Asian dust emissions begin later in the morning and extend through the early evening. As the model spatial resolution is increased, the diurnal cycles are consistent with Figure 4.17. The 2° and 1° diurnal cycles are comparable to one another and have a significantly lower magnitude when compared to the 0.5° and 0.25° diurnal cycles.

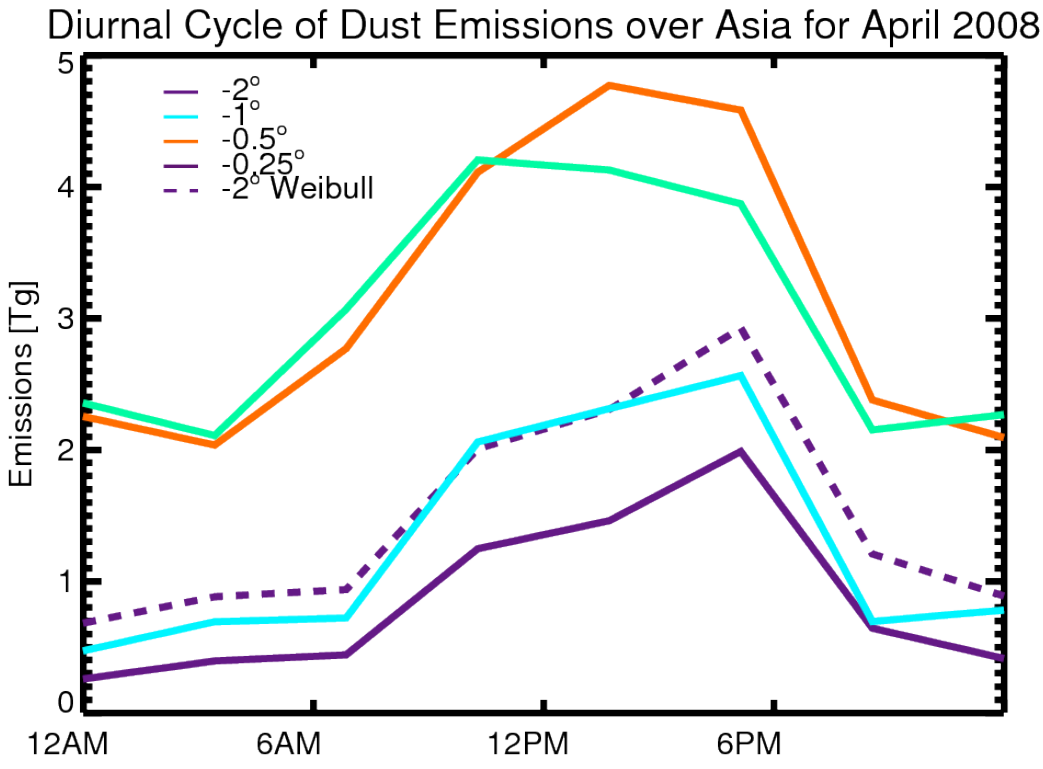

Figure 4.18. April 2008 mean diurnal emission cycle over the Asian region for the GOCART emission scheme.

Table 4.3 shows the ratio of dust diurnal emission maxima to minima over the Asian source region. For all simulations, the ratio significantly decreases with model spatial resolution, indicating that model spatial resolution has a significant effect on dust emissions over the Asian source region. When combined with Figure 4.16, this result suggests that simulated dust emissions in GEOS-5 have a greater sensitivity to model spatial resolution over the Asian source region when compared to the African source region. Additionally, over the Asian source region, a significant discrepancy exists between dust emissions simulated at coarse and high spatial resolutions, which is further explored in Section 4.4.

4.3.2.2.3 Lifetime

The previous section showed that model spatial resolution has a strong effect on simulated dust emissions for the various treatments of the dust mobilization process. Differences in the emitted dust mass will affect the mass of dust entrained into the atmosphere, and therefore the lifetime τ of the dust aerosol, defined by Textor [2006]:

$$\tau_{life} = \frac{Burden}{Sink_{wet+dry}}$$

Eq. 4.3

where the burden is defined as the total mass of dust suspended in the atmosphere and the sinks represent the total (wet + dry) mass removal rates.

Table 4.4 shows the April 2008 mean dust aerosol lifetime for each of the four sensitivity experiments at 2° resolution. The GOCART and GOCART-source

simulations have very similar and shorter dust lifetimes when compared to the GOCART-threshold and DEAD simulations. This result is a reflection of the differences in how the emitted particle size distributions are handled between the different simulations. To reiterate, the GOCART-threshold and DEAD simulations will emit a greater fraction of sub-micron sized particles when compared to the GOCART and GOCART-source simulations. Sub-micron particles have a longer atmospheric residence time when compared to larger particles and increasing their relative contribution to the dust loading will act to extend the simulate dust aerosol lifetime.

Experiment	GOCART	DEAD	GOCART-threshold	GOCART-source
τ_{life} (days)	4.31	5.70	4.55	4.32

Table 4.4. April 2008 dust aerosol lifetimes (days) for the 2° GOCART, DEAD, GOCART-threshold, and GOCART-source simulations.

Table 4.5 shows the sensitivity of the simulated dust aerosol lifetime to model spatial resolution for the GOCART simulation. Surprisingly, increasing the model spatial resolution acts to reduce the dust aerosol lifetime, despite increasing the emissions (see Figure 4.16). This suggests that while increasing the model spatial resolution increases the mass of emitted dust, dust removal increases at a greater rate, acting to reduce the simulated dust aerosol lifetime. Offline analysis showed that of the removal processes, sedimentation exhibited the most sensitivity to model spatial resolution. This result has implications for dust transport, as it suggests that downwind dust distributions may be less sensitive to model spatial resolution despite significant increases in emissions as sedimentation is the dominant removal process near the source regions. This is effect is

further explored in the following section where the effect of model spatial resolution on AOT is presented.

Resolution	2°	1°	0.5°	0.25°
τ_{life} (days)	4.31	4.29	3.90	3.42

Table 4.5. The effect of model spatial resolution on April 2008 simulated dust aerosol lifetimes (days) for the GOCART simulation.

4.3.2.2.4 Aerosol Optical Thickness

Ultimately, differences in simulated dust emissions and lifetimes resulting from model spatial resolution will affect the simulated dust loading. Global models rely on look-up tables of mass extinction efficiency to convert simulated dust loadings to determine an AOT, which is used to tune the model's emissions to match observed values. Here, the effect of model spatial resolution on AOT magnitude and timing is explored over the African and Asian source regions using ground-based observations from AERONET and satellite observations from MISR. It should be noted that while model spatial resolution might have implications for simulated distributions of other aerosol species, this analysis is performed over the African and Asian source to limit the contribution from other aerosol species so that the effect of model spatial resolution on simulated dust distributions may be isolated.

To evaluate the effect of model spatial resolution on the timing of Saharan dust events, simulated GOCART AOT values are compared to all observations from the Tamanrasset-INM AERONET site (Figure 4.13) during April 2008 (Figure 4.19). Due to its location within the African source region and number of observations, the AERONET

record clearly has diurnal variability. At 2°, simulated AOT values are well correlated (R^2=0.535) with AERONET and the mean simulated AOT is comparable in magnitude. As the model spatial resolution is increased, simulated AOT values increase, but are better correlated, indicating that increasing model spatial resolution improves the timing of simulated dust events and the representation of the diurnal emission cycle at this location, despite having a high bias in AOT magnitude. It should be noted that if the tuning constant were adjusted, the best representation of AOT would be achieved at higher resolutions. On April 4, a dust event was simulated at all resolutions that was not observed by AERONET. This event is seen in the Level 1 (not cloud screened) AERONET AOT product, indicating that it was thought to be a cloud. A similar comparison was made for the DEAD simulations (not shown). Simulated DEAD AOT values were significantly higher than those observed by AERONET and simulated by GOCART. Interestingly, despite having differences in the simulated dust emission cycle, there were not any substantial differences in the correlations between the GOCART and DEAD simulations at each resolution.

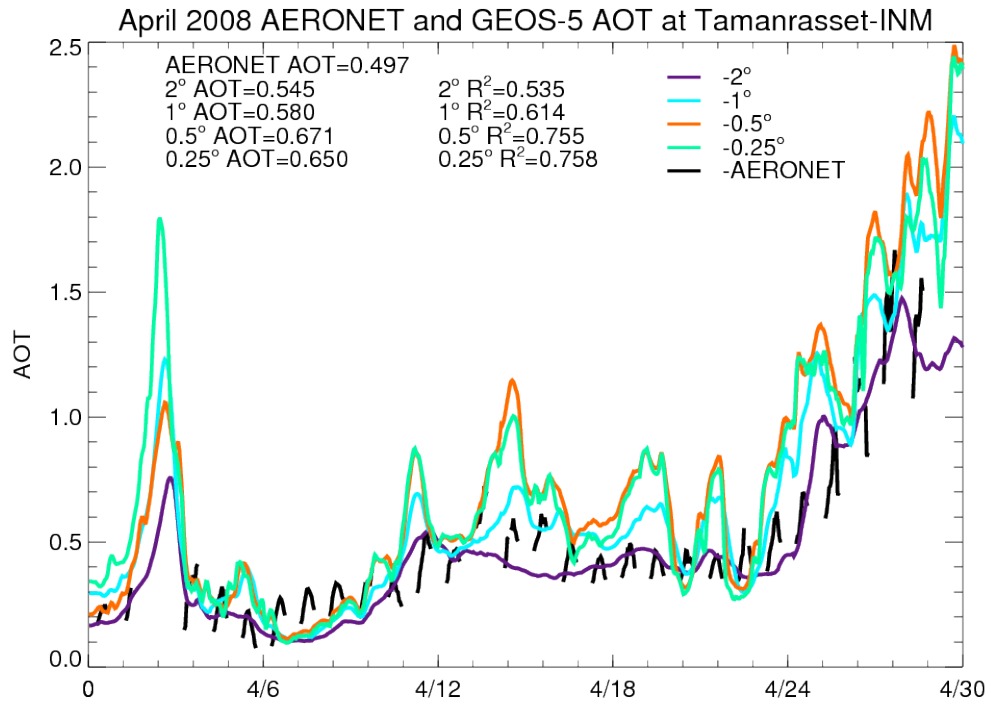

Figure 4.19. AERONET and GOCART April 2008 AOT at Tamanrasset-INM at 2°, 1°, 0.5°, and 0.25° resolution.

Figure 4.20 compares the April 2008 MISR AOT to the standard GOCART simulation over the African source region as the model spatial resolution is increased from 2° to 0.25°. At 2°, the GOCART scheme has good agreement with MISR over the Saharan source region, though the model is slightly lower in magnitude. The simulated AOT is also slightly lower in magnitude off North African coast and is not transported as far west as observed by MISR. As the model spatial resolution is increased, the model picks up the observed dust AOT hot spots, though at a greater magnitude. In particular, some regions of high AOT that were not evident in the 2° and 1° simulations are resolved at higher resolutions. Additionally, as the model spatial resolution is increased, simulated AOT values have better agreement with MISR off the North African coast but gains a

slight high bias north of 12° N. The simulated magnitude and extent of transported AOT from the Saharan source region across the tropical North Atlantic Ocean also improves, though still at a slightly lower magnitude. Due to effect of model spatial resolution on the simulated aerosol lifetime (Table 4.5), transported dust AOT position and magnitude is comparable at all resolutions.

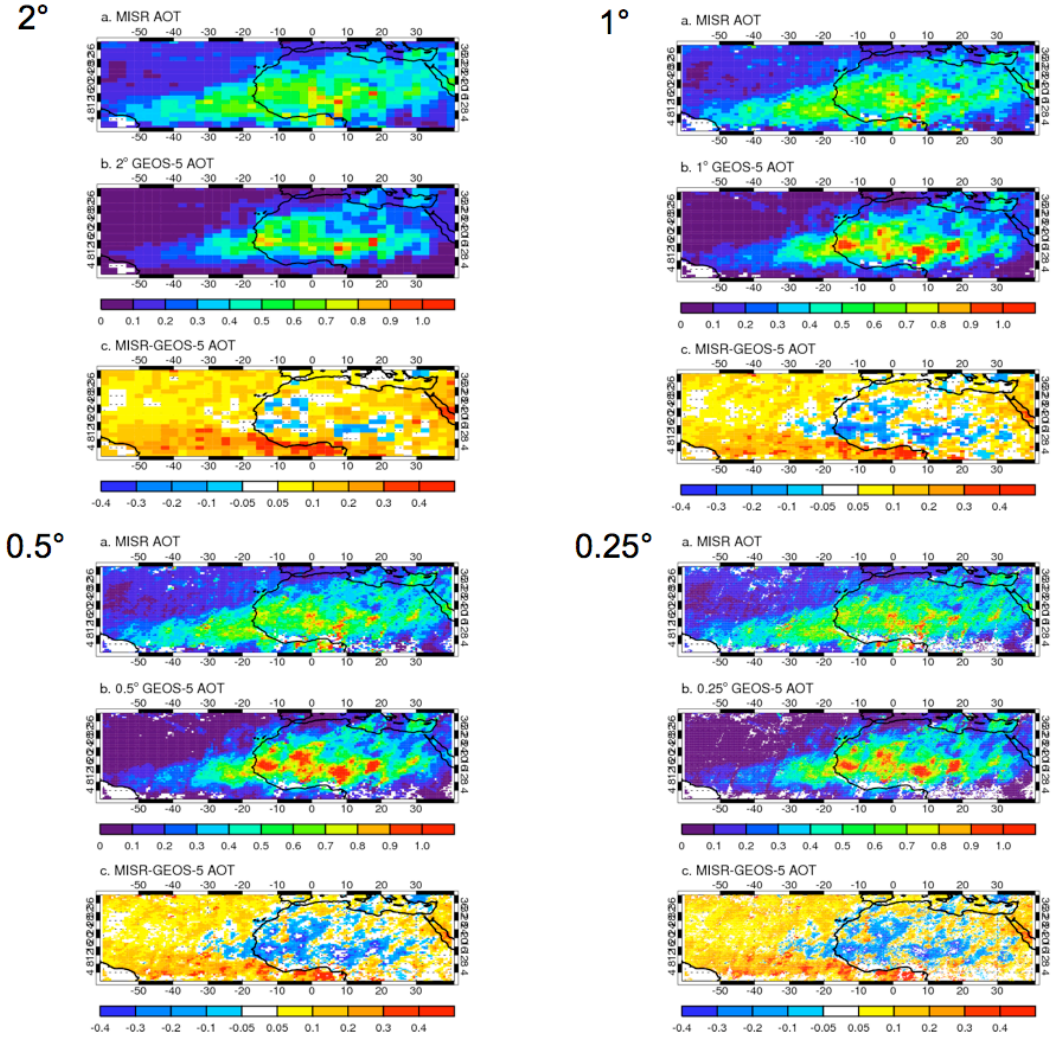

Figure 4.20. MISR and GOCART April 2008 AOT over North Africa at 2°, 1°, 0.5°, and 0.25° resolution.

Unfortunately, there are not any permanent AERONET sites located within or near the Asian source region. However, from April 17 - June 18, the SMART-COMMIT

mobile laboratories were deployed at the Zhangye National Climate Observatory (39° N, 100° E), 100 km from the edge of the Gobi Desert (Figure 4.13) as part of the U.S. Department of Energy's Atmospheric Radiation Measurement (ARM) Mobile Facility deployment [Li et al., 2007; Li et al., 2011], providing sunphotometer observations of AOT. Figure 4.21 compares the observed AOT time series to the GOCART simulations as the model spatial resolution is increased. While the observed record is somewhat sparse, it is clear that the higher resolution simulations are better correlated and have better agreement with the magnitude of the observed AOT. A similar comparison was made for the DEAD simulations (not shown). The DEAD simulation exhibited a stronger sensitivity to increases to the model spatial resolution, but correlations were slightly lower compared to GOCART simulations.

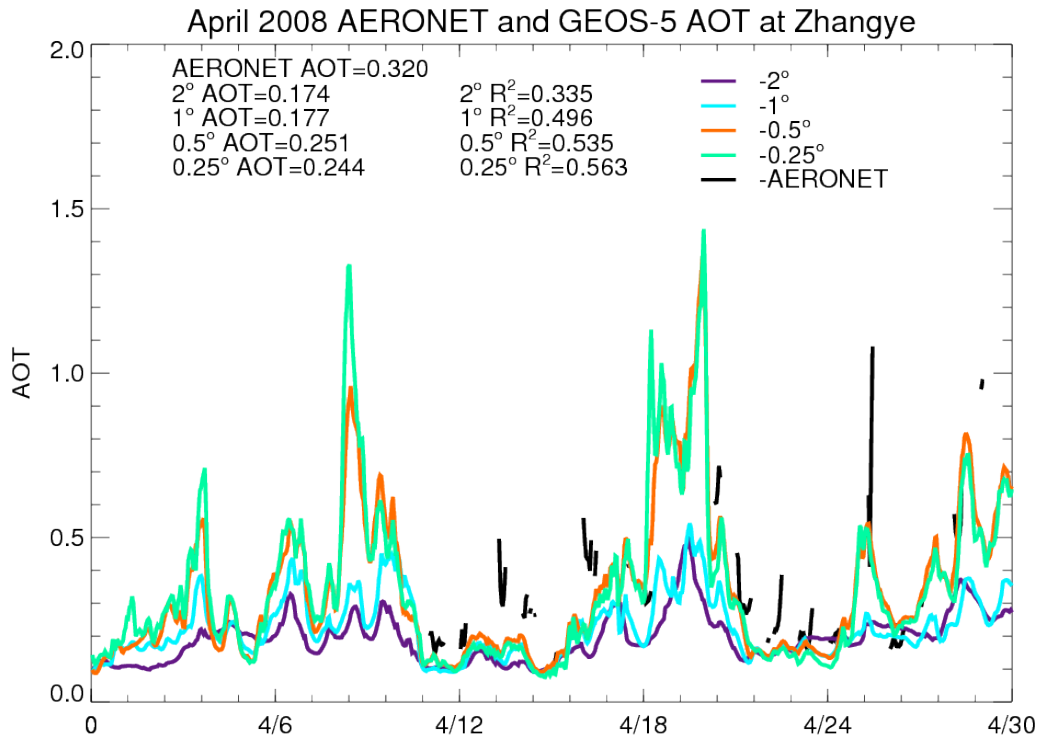

Figure 4.21. AERONET and GOCART April 2008 AOT at Zhangye at 2°, 1°, 0.5°, and 0.25° resolution.

Figure 4.22 shows the effects of increasing model spatial resolution on simulated AOT distributions over the Asian source region. At 2°, the simulated AOT is essentially non-existent over the Taklamakan and Gobi deserts when compared to MISR. As the spatial resolution is increased to 0.5° and 0.25°, the model becomes much more comparable with MISR over the deserts, though the model obtains a slight high bias. Downwind from the Asian deserts the model is biased low at all resolutions. However, in these regions, urban aerosols have a significant contribution to the AOT, suggesting that tuning of other simulated aerosols might be considered. Regardless, it is clear that model spatial resolution has a significant effect on simulated dust AOT distributions and reaffirms that low resolutions simulations do not provide an accurate representation of the dust aerosol lifecycle over the Asian source region. Additionally, this identifies a need for regional dust emission tuning as model spatial resolution clearly has a greater effect on simulated AOT distributions over the Asian source region than over the African source region.

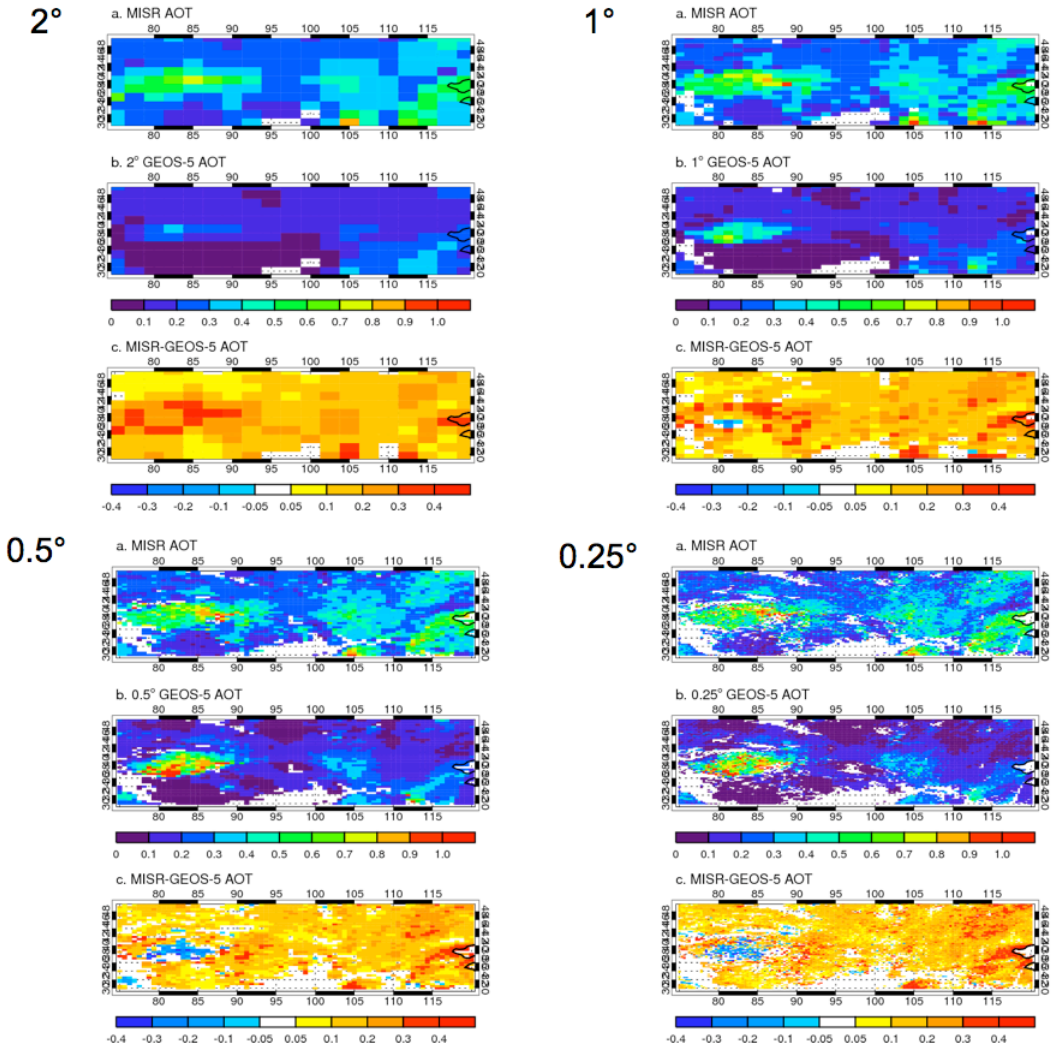

Figure 4.22. MISR and GOCART April 2008 AOT over Asia at 2°, 1°, 0.5°, and 0.25° resolution.

4.4 Discussion

Perhaps the most significant result from this analysis has been that simulated dust distributions are highly sensitive to model spatial resolution. This is particularly evident over the Asian source region, where both emissions and AOT distributions are anemic at course resolutions and display non-linear increases with spatial resolution.

From Figure 4.21, GEOS-5 simulates a dust event at Zhangye on April 19 – 20 at all resolutions, though the higher resolution simulations are greater in magnitude.

Unfortunately, the SMART - COMMIT sunphotometer did not observe the event, only capturing its end (Figure 4.19). However, during April, particle number distributions were provided by APS on 14 days, including April 20. Observed particle number distributions were converted to volume distributions for comparison to GEOS-5. Figure 4.23 shows the average observed particle size distributions compared to those simulated by GOCART on April 20. As the model spatial resolution is increased, the simulated volume distributions significantly improve when compared to the observed distribution, giving credibility to the simulated dust event on April 20 (Figure 4.21).

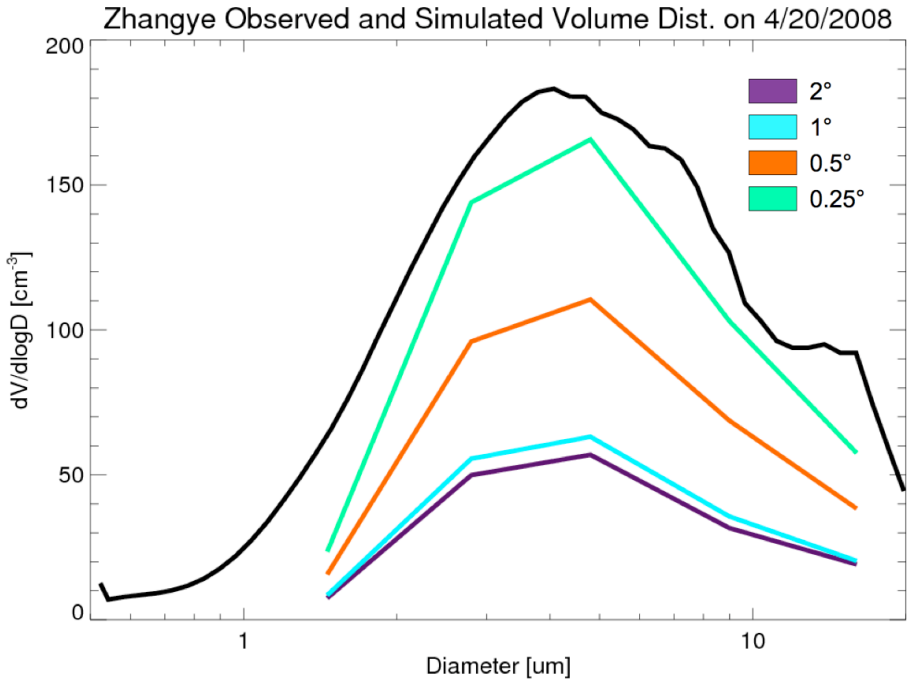

Figure 4.23. Observed and simulated volume distributions on April 20, 2008.

Asian dust events from the Taklamakan and Gobi deserts are frequently transported to China's industrial corridor, where dust mixes with industrial aerosols to form extreme pollution events. Figure 4.24 shows how a dust event simulated on April 19 – 20 evolves as it is transported over Zhangye to Beijing (Figure 4.13). On April 22,

the dust event reaches Beijing, though it is only evident in the 1°, 0.5°, and 0.25° simulations, as the dust event was transported south of Beijing in the 2° simulation. Therefore, not only does spatial resolution limit the ability of the model to reproduce the timing and magnitude of simulated dust events at coarse resolutions, but also transport.

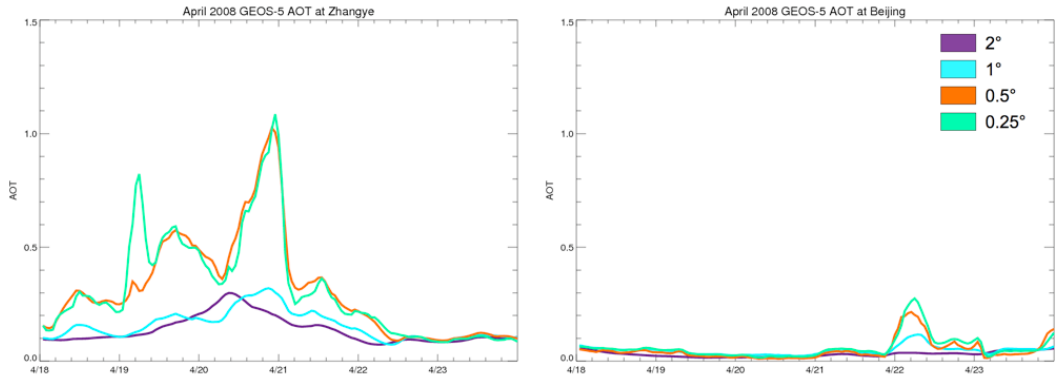

Figure 4.24. The effect of model spatial resolution on a transported dust AOT.

The Saharan desert is large and relatively flat so that dust events are easily mobilized, lifted, and transported away from the source region. The mobilization of dust events over the Taklamakan desert is more complex, as mountains on its southern, western, and northern sides surround it. Mountain winds swirl within the Taklamakan valley, occasionally transporting dust out of its eastern edge. Therefore, the effect of model spatial resolution might affect the model topography, which in turn could influence the dynamics used to parameterize dust emission in the model. As a proxy for elevation, Figure 4.25 shows the April 2008 average geopotential height over Taklamakan as the model spatial resolution is increased. It is evident that the coarser resolution simulations do not resolve the Panir and Tian Shan mountains to the west and the south of the Taklamakan, respectively, potentially limiting the model from producing

sufficient circulations and wind speeds over the Taklamakan to initialize and transport dust events eastward.

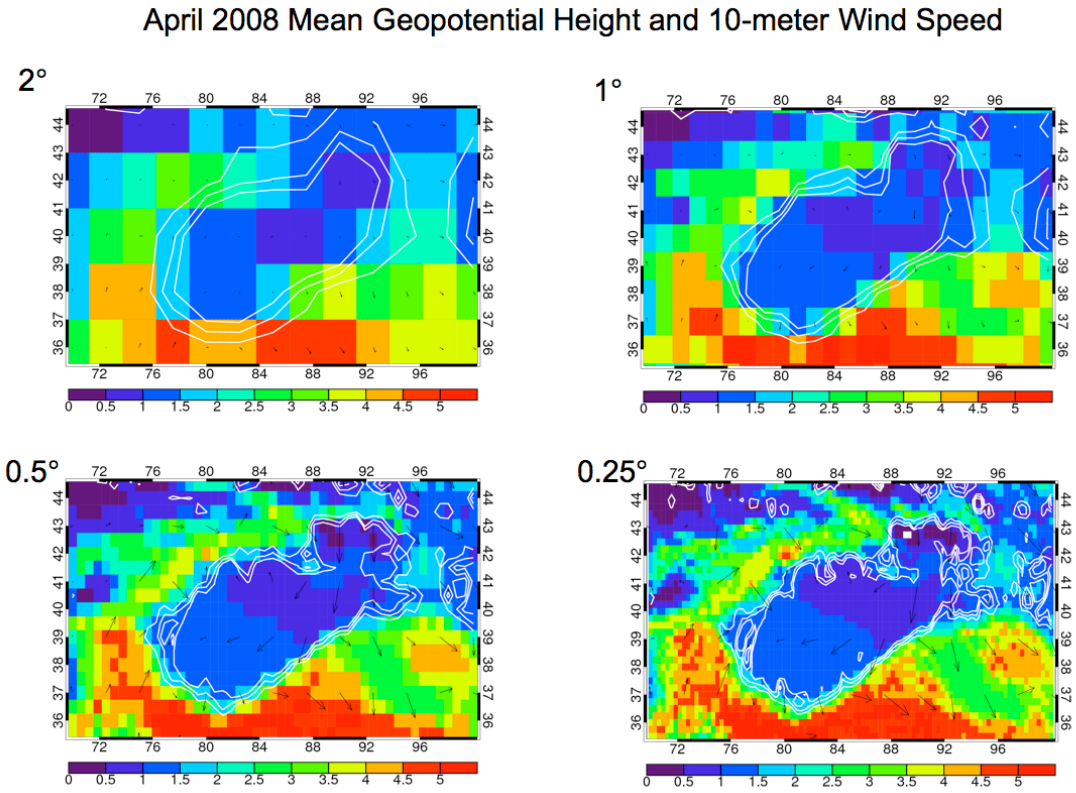

Figure 4.25. The effect of model spatial resolution on mean geopotential height [km] and 10-meter wind field over and surrounding the Taklamakan source region (white contour).

Figure 4.26 shows a cross-section at 85° W of the April 2008 mean east-west wind across the Taklamakan desert at 2° and 0.5°. As expected, the Tian Shin mountains are better resolved and the surface winds have a greater magnitude at 0.5°. At 2°, the mean wind field is westward over the Taklamakan. However, at 0.5°, while the wind field is primarily westward over the southern ¾ of the desert, an eastward component to the wind field is resolved over the northern ¼, suggesting that model spatial resolution influences both the magnitude and direction of Taklamakan wind circulation.

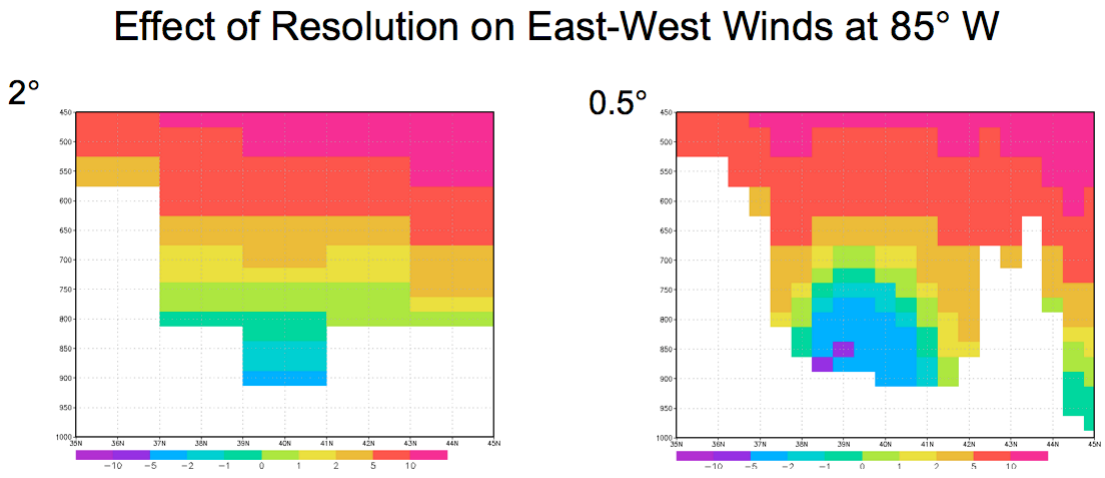

Figure 4.26. April 2008 east-west wind field at 85° W at 2° and 0.5° resolution.

In an attempt to overcome this potential limitation, the effect of including sub-grid wind variability in a 2° simulation is explored following Gillette and Passi [1988], Cakmur [2004] and Su et al. [2009]. Justus et al. [1978] found that the observed variability in the 10-meter wind speed can be approximated using a Weibull distribution:

$$f(x) = \frac{k}{c}\left(\frac{x}{c}\right)^{k-1} e^{-(\frac{x}{c})^k} \quad x \geq 0 \qquad \text{Eq. 4.3}$$

where f(x) is the wind speed PDF and c and k are the size and shape parameters estimated by Justus et al. [1978] and Grini et al. [2005]:

$$c = U_{10m}\left[\Gamma(1+1/k)\right]^{-1} \qquad \text{Eq. 4.4}$$

$$k = 0.94\sqrt{U_{10m}} \qquad \text{Eq. 4.5}$$

where Γ is the gamma function and U is the mean 10-meter wind speed. Following Gillette and Passi [1988], it is assumed that the variability in the 10-meter wind speed lies between the 5^{th} and 95^{th} percentiles. By incorporating the Weibull distribution, dust emission can now occur in situations when the 10-meter wind speed does not meet the required emission threshold due to the assumed variability in the winds.

As a sensitivity test, the Weibull distribution was incorporated into the GOCART scheme for a 2° replay simulation of 2008, using the same tuning constant as the baseline GOCART scheme. Incorporating the Weibull distribution acts to significantly increase the 2° April 2008 global dust emissions to from 217 Tg to 330 Tg and are very comparable to higher resolution simulated emissions. Over Africa and Asia, dust emissions increase to 242 Tg and 10 Tg, compared to 163 and 6 Tg, respectively. Over the Asian source region, the magnitude of the diurnal emission cycle increases and is more comparable to that of higher resolutions (Figure 4.18).

Figure 4.27 shows the April 2008 total AOT from MISR and the 2° GOCART – Weibull simulation over the Asian source region. Incorporating the effects of sub-grid wind variability significantly reduces the low bias in simulated AOT magnitude over the Taklamakan and Gobi deserts when compared to MISR. However, over the Saharan, incorporating sub-grid wind variability leads to a high bias (Figure 4.28), though the magnitude and location of transported AOT has good agreement with MISR, suggesting once again that removal processes over the Saharan source region are too strong in GEOS-5. Interestingly, while incorporating sub-grid wind variability influences the

magnitude of dust events, the timing of simulated dust events is minimally impacted (Figure 4.29).

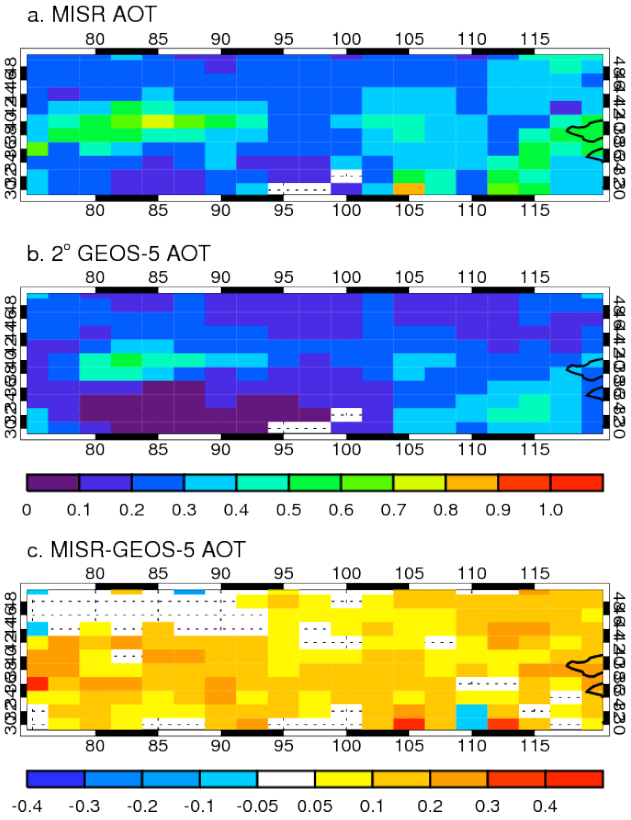

Figure 4.27. MISR and GOCART-Weibull April 2008 AOT over the Asian source region at 2°.

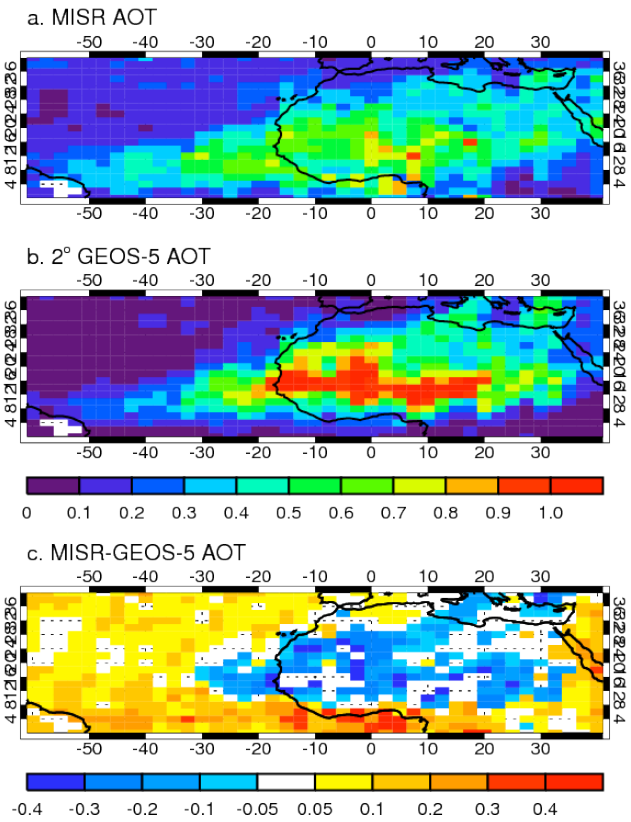

Figure 4.28. MISR and GOCART-Weibull April 2008 AOT over the African source region at 2°.

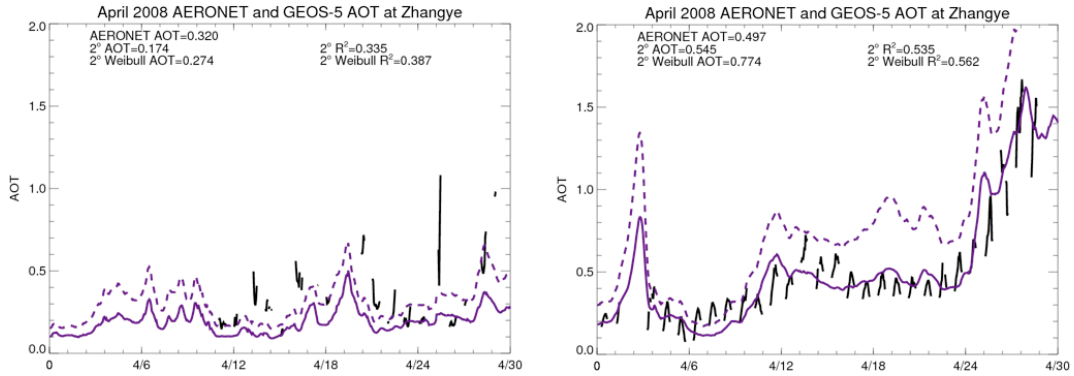

Figure 4.29. GOCART (solid, purple) and GOCART-Weibull (dashed, purple) AOT at Zhange (left) and Tamanrasset-INM (right).

Overall, the improvements to the simulated AOT over the Asian source region suggest that sub-grid wind variability should be included in coarse resolution simulations.

However, further validation is required, specifically evaluating the effects of sub-grid wind variability on longer time scales and its effect on 1° simulations.

4.5 Summary and Conclusions

This study explored the sensitivity of simulated dust emissions, lifetimes, and AOT distributions to the spatial resolution in GEOS-5. In particular, various treatments of the mobilizing physics, as well as the dust source function were considered. In one sensitivity study, a set of simulations that used a high-resolution version of the dust source function was compared to an equivalent set of simulations that used a coarse, fixed version. After comparing the two sets of simulations, it was found that the resolution of the source function does not have a significant impact on dust emissions.

Three different treatments of the physical parameterizations of dust emission were considered: GOCART, DEAD, and a version of the mobilization process that extrapolates the minimum threshold speed required for particle mobilization in DEAD to 10 meters (GOCART-threshold). Model spatial resolution has a significant impact on simulated dust distributions, as increasing the model spatial resolution resulted higher wind speeds. Because simulated dust emissions have a cubic dependence on the wind speed, model spatial resolution effects on the simulated wind speeds acted to significantly increase the emitted mass. This effect is particularly evident over Asia, where dust emissions were virtually non-existent at coarse resolutions, but increased significantly with model spatial resolution.

Of the different treatments of the dust emission process, the DEAD scheme simulated the longest dust aerosol lifetime at 2°. This result follows from Chapter 3,

where it was found that the DEAD scheme emits a greater fraction of submicron particles than GOCART based schemes, which will act to increase the dust aerosol lifetime. The dust aerosol lifetime also showed sensitivity to model spatial resolutions. As model spatial resolution increased, the dust aerosol lifetime decreased, implying that removal rates are more sensitive to model spatial resolution than emission rates.

Simulated AOT distributions exhibited a strong sensitivity to model spatial resolution as well. Over Africa, increasing the spatial resolution lead to a high bias in AOT magnitude when compared to MISR, though higher resolution simulations better captured the diurnal variability observed the Tamanrasset-INM AERONET site. Because the simulated aerosol lifetime was found to decrease with model spatial resolution, AOT magnitudes downwind of the source region were relatively insensitive to the effects of model resolution, despite greater emissions. Over the Asian source region, the model had a significantly low bias at coarse resolutions that improved with model spatial resolution. Additionally, similar to over the African source region, the timing of simulated dust events improved with model resolution at Zhangye. Investigation into the effect of spatial resolution on the topography that surrounds the Asian source region suggested that resolutions has impacts for dynamical circulations that initiate Taklamakan dust events.

In an attempt to improve the representation of simulated dust distributions over the Asian source region at coarse resolution, Weibull wind distributions were incorporated into the GOCART scheme to represent the sub-grid variability of wind speeds. This led to significant improvement when compared to MISR AOT over the Asian source region and increased an already high bias over the African source region, but did not influence the timing of simulated dust events at Tamanrasset-INM and

Zhangye. This effect is the result of using threshold wind speeds for aerosol-sized particles to parameterize dust emission in the GOCART scheme. Incorporating the effects of sub-grid wind variability may have a greater impact for GOCART-threshold based simulations, as the threshold is the same order of magnitude as the driving winds and should act to initiate more dust events when compared to the GOCART scheme. This may act to improve the timing of dust events in addition to AOT magnitude. Regardless, due to the improvement to the AOT magnitude over the Asian source region, this sensitivity study suggests that the effects of sub-grid wind variability should be considered in future implementations of the model after further investigation.

Ultimately, tuning constants will be determined by evaluating simulated AOT distributions using satellite and ground-based observations. The results of this analysis show that simulated dust distributions are highly sensitive to model spatial resolution, and therefore, tuning constants should be a function of model resolution. Additionally, this work highlights the need for regional tuning constants in global models, as the biases and sensitivity to model spatial resolution were different between the African and Asian source regions. Tuning constants will be unique to every global aerosol transport model as each model will resolve the parameters that control dust emission differently, but are necessary as the aerosol modeling community moves from performing long term climate simulations to high-resolution aerosol forecasts. Finally, while this work was focused specifically on dust aerosols, similar analyses should be extended to other aerosol species treated in the model, particularly those parameterized in terms of model derived fields (e.g. sea-salt).

Chapter 5: Investigation of Dust Transport and Loss Processes

5.1 Introduction

The previous chapter investigated the parameterization of dust source processes in the NASA GEOS modeling system. Here, the other components of the simulated dust aerosol lifecycle, namely transport and loss processes are evaluated while exploring their contribution to a real world phenomenon: the Central American dust barrier.

During boreal summer, Saharan dust is transported to the Caribbean and northern South America by the prevailing tropical easterly winds [Karyampudi et al., 1999; Carlson and Prospero, 1972]. Satellite observations show an apparent barrier that inhibits dust transport from the Caribbean into the eastern Pacific (Figure 5.2). This barrier is also apparent in airborne observations from the recent NASA Tropical Composition Cloud and Climate Coupling (TC^4) field campaign (July – August, 2007) [Toon et al., 2010]. The presence of this barrier likely has geochemical implications, insofar as it inhibits transport of iron containing Saharan dust to aquatic and terrestrial ecosystems west of 80° W.

While numerous studies have focused on the broader patterns of dust transport and deposition into the Caribbean [Kaufman et al., 2005; Mahowald et al., 1999, Tegen and Fung, 1995; Duce et al., 1991], none have focused on the mechanisms for the observed barrier to dust transport into the Pacific and its representation in global dust transport models. The relative roles of dust transport and loss processes are uncertain in establishing and maintaining this barrier. Furthermore, while dust removal processes

such as precipitation scavenging certainly are significant, there are insufficient data to fully constrain the representation of these processes in aerosol transport models. Perhaps better constrained are dynamical features, insofar as they are well represented in meteorological analyses, to ascertain the relative importance of meteorology in tracer transport studies.

Here, the roles of transport and loss processes in establishing and maintaining the Central American dust barrier are explored by running GEOS-5 for July 2007 in order to exploit aircraft observations made during the NASA TC^4 field campaign. For this study, a 0.5° baseline GEOS-5 replay simulation using the GOCART dust emission scheme was performed. Chapter 4 illustrated that while mobilization scheme choice and model spatial resolution is significant for dust distributions near the source region, their effects become insignificant with distance from the source region.

5.2 Evidence of the Central American Dust Barrier

In this section observational evidence that suggests there is a persistent barrier to dust transport along the Central American coastline is presented. Additionally, the representation of the barrier in GEOS-5 is presented and a transported dust event during TC^4 is used to evaluated dust transport in GEOS-5.

5.2.1 Moderate Resolution Imaging Spectroradiometer Climatology

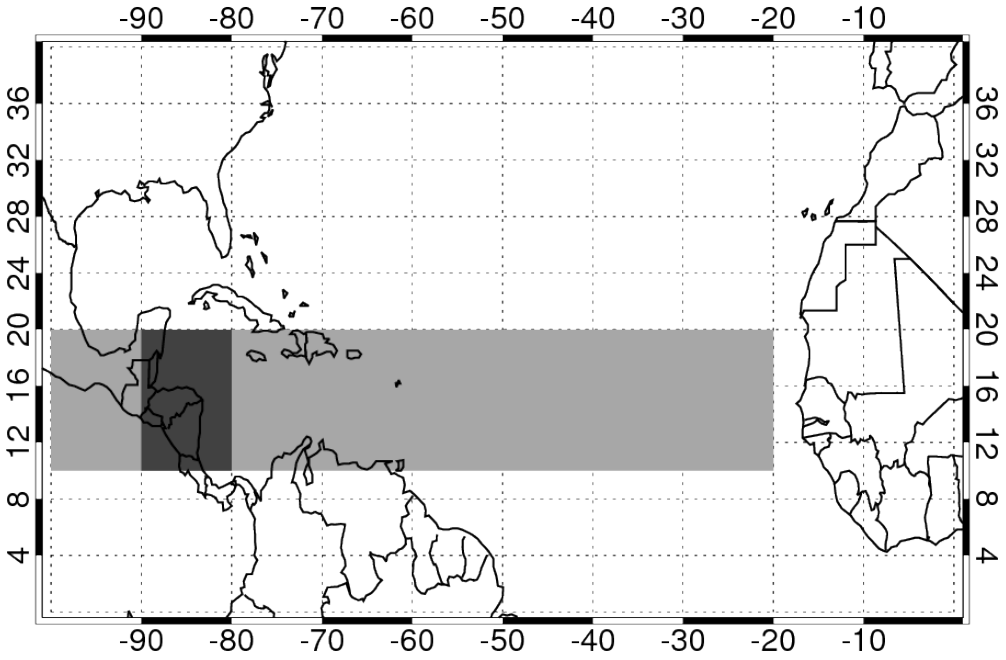

Figure 5.1. Dust barrier-averaging regions (shaded).

Figure 5.2 shows the climatology of July MODIS-Aqua (2003-2010) and MODIS-Terra (2000-2010) land and ocean AOT averaged over the latitudes of peak Caribbean dust AOT (10° N - 20° N, see Figure 5.1). There is a sharp drop in the observed AOT west of 80° W. This strong gradient in AOT between about 80° and 90° W is referred to as the Central American dust barrier, and from the climatology of satellite observations, it is a persistent feature in the northern summer. In what follows the is narrowed to July 2007 to utilize observations made during the TC^4 field campaign. Figure 5.2 also shows the MODIS-Terra AOT specifically for July 2007. There is

evidence of the Central American dust barrier during this period, as the mean MODIS-Terra AOT drops from 0.375 at 80° W down to 0.2 at 90° W.

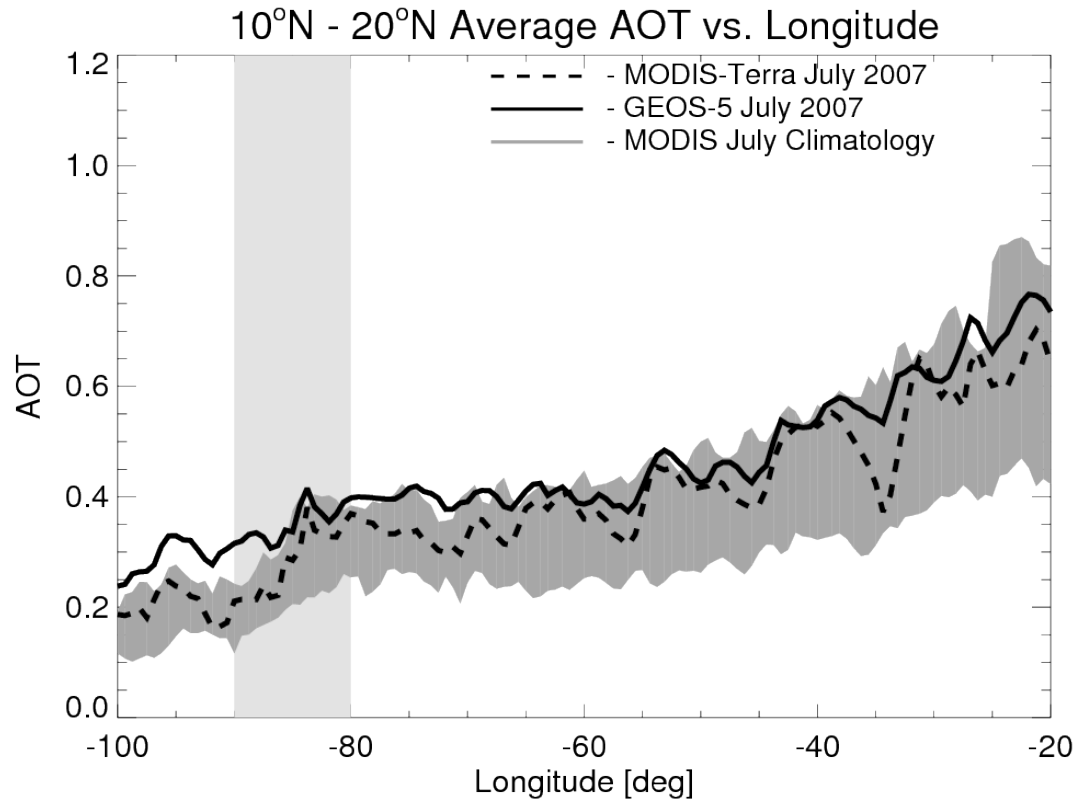

Figure 5.2. MODIS-Terra/Aqua July climatological (2002-2010) AOT (shading), MODIS-Terra July 2007 AOT (dashed) and GEOS-5 sampled (solid) July 2007 AOT averaged from 10º-20º N.

Figure 5.2 also shows the July 2007 AOT from the GEOS-5 model averaged over the same region. For this comparison the modeled AOT has been sampled at the times and locations of the MODIS observations. Over the Caribbean (west of 60° W), the model AOT is comparable to MODIS-Terra. Near the Central American coastline, the model shows evidence of a barrier to dust transport, although not as strong as observed, decreasing from 0.4 at 80° W to 0.3 at 90° W (Figure 5.2).

For a spatial illustration of the Central American dust barrier, Figure 5.3 shows July 2007 monthly means of total AOT from MODIS-Aqua and our simulation (sampled

at MODIS-Aqua observations points as described above). Off the west coast of North Africa, the model has the peak AOT in the same location as the sensor, but at a greater magnitude. Moving west across the tropical North Atlantic, the model matches the observed dust plume location and width, and the magnitude of AOT becomes more comparable with observations. Owing to improvements in the model physics and the MERRA analyses, GEOS-5 does better transporting dust from the Saharan source region to the Caribbean relative to previous versions of the model [Colarco et al., 2010; Nowottnick et al., 2010]. However, consistent with Figure 5.2, the model extends its dust plume somewhat into the eastern Pacific (90° – 95° W), while MODIS-Aqua AOT values are constrained to the Caribbean. This feature is also seen in Figure 5.2, where the model representation of the Central American dust barrier is not as pronounced as observed by MODIS-Terra. Despite not being as pronounced as observed by MODIS, the model shows evidence for a barrier to dust transport that corresponds with the Central American coastline.

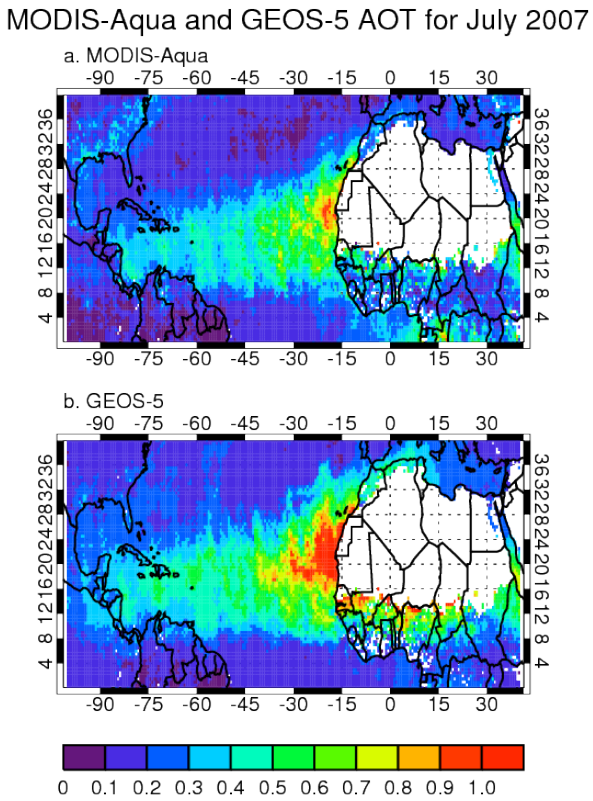

Figure 5.3. MODIS-Aqua (a) and GEOS-5 sampled (b) July 2007 AOT.

5.2.2 Central American Dust Barrier Case Study: 19 July 2007

During the TC^4 field campaign, a Saharan dust plume was observed over the Caribbean on 19 July with the CPL flying on the NASA ER-2 aircraft. Using CALIOP, this dust event was tracked from the Saharan source region (14 July) to the Caribbean (19 July) to evaluate simulated vertical dust distributions during transport (Figure 5.4). For an accurate comparison, GEOS-5 was along the CALIPSO track at the model synoptic time nearest to the daytime CALIOP measurement.

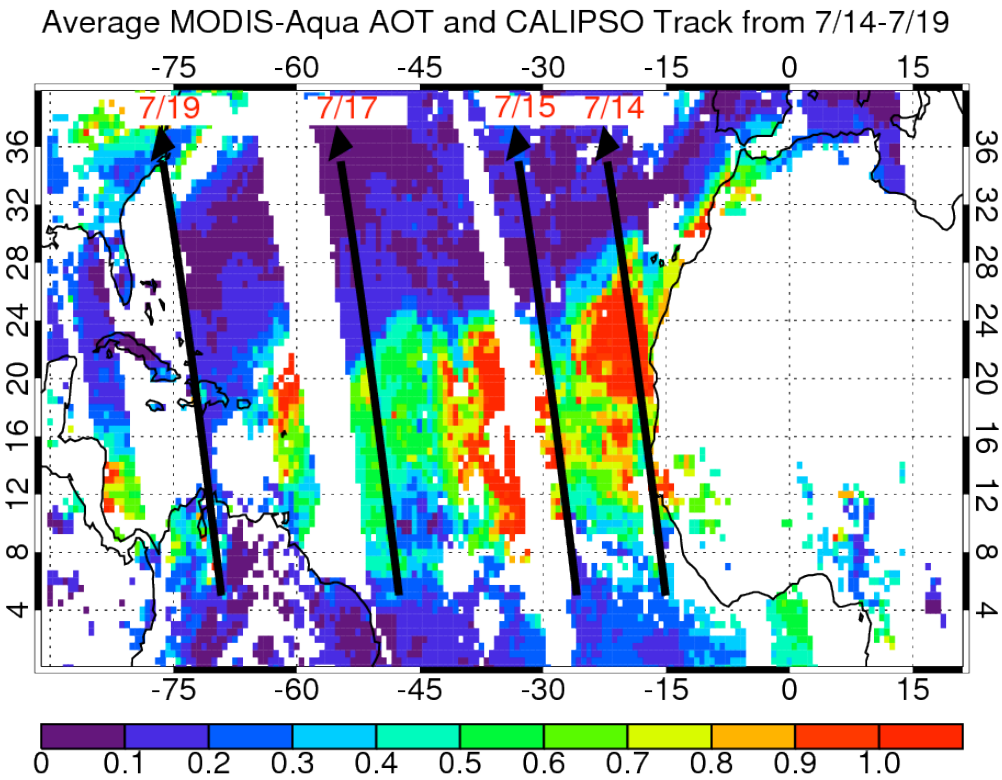

Figure 5.4. Average MODIS-Aqua AOT and CALIPSO track from 7/14-7/19.

Shown in Figure 5.5 are GEOS-5 comparisons to CALIOP 532 nm total attenuated backscatter and feature mask from 14 July to 19 July. On 14 July, CALIOP observes a thick, elevated dust plume located from 2-5.5 km that extends from 10° - 26° N. The model captures the latitude extent of the dust plume observed by CALIOP, but is lower in altitude ranging from 1-5.5 km. A limitation of CALIOP is that its signal becomes attenuated towards the surface when it encounters thick aerosol plumes. On this day, the CALIOP signal might be partially attenuated at low altitudes, so the CALIOP data may suggest the lowest edge of the dust plume is at a higher altitude than it actually was. In the CALIOP layer identification product, low-level marine clouds are observed north of 15° N below 1 km. While only extinction from aerosols is shown, the influence

of these clouds can be seen in the aerosol total extinction where the aerosols in this region have swelled in the marine boundary layer and are marked by high extinction values. Moving farther from the Saharan source region, the edge of a dust event is observed on 15 July. CALIOP observes an elevated, thick layer of dust that extends from 2-5 km between 11° - 24° N, which is well represented in the model. Further downwind on 17 July, the model matches the observed horizontal extent and altitude of the observed dust plume. The simulated dust plume extends down to the surface into a region where CALIOP identifies a thin layer of maritime clouds, making it difficult to determine whether the lower extent of the simulated plume is correct. On 19 July, the model captures the narrow north-south width and low-altitude dust plume observed below 3 km by CALIOP, although clearly the observations are impacted by the presence of mid- and low-level clouds. For this case, GEOS-5 captures similar dust plume features to the CALIOP observations during this time period.

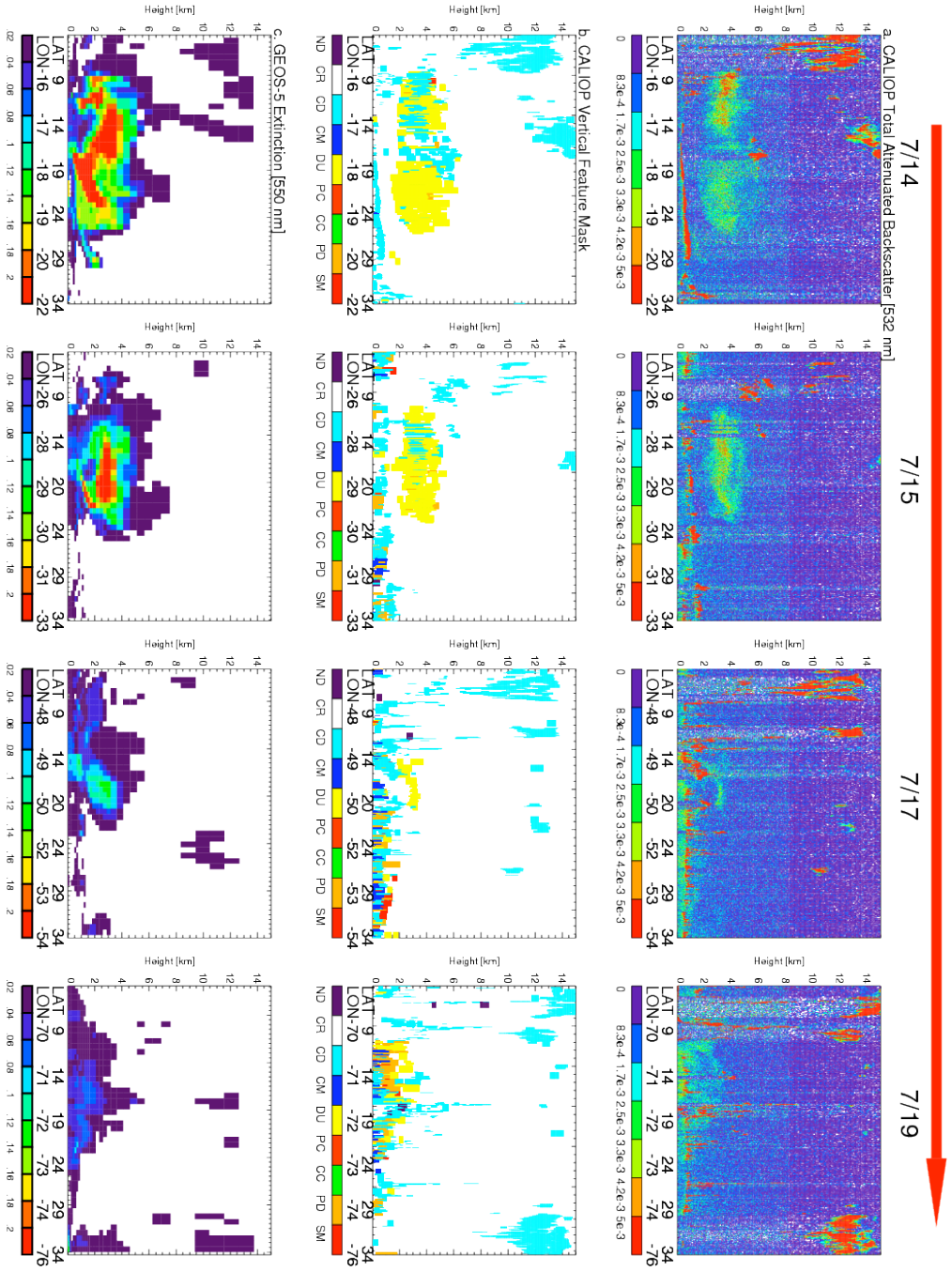

Figure 5.5. CALIOP total attenuated backscatter [km^{-1} sr^{-1}] (a), CALIOP vertical feature mask (b), and GEOS-5 extinction [km^{-1}] (c) for a dust event tracked from Africa (7/14) to the Caribbean (7/17).

Figure 5.6 shows the composite MODIS-Terra/Aqua and GEOS-5 550nm AOT at 18Z, with the ER-2 flight track overlaid on 7/19. On this day, the ER-2 aircraft originated from Costa Rica, heading southwest over the Pacific Ocean to 90° W, then turned around and headed northeast back towards Costa Rica. The aircraft continued past Central America over the Caribbean Sea to 75° W and then headed southwest back to Costa Rica. During the flight, CPL provided an approximately east-west transect of total attenuated backscatter that extends from the Pacific Ocean into the Caribbean. Comparing the model to MODIS on this day, the model matches the observed AOT location and magnitude over the Caribbean. Over the Pacific Ocean MODIS is partially obscured by precipitating clouds. Also displayed in Figure 5.6 are the observed daily precipitation (mm day^{-1}) from the Global Precipitation Climatology Project (GPCP) [Huffman et al., 2009; Adler et al., 2003] and the simulated daily precipitation from GEOS-5 with the 700 mb wind field at 18Z overlaid. GPCP provides precipitation data at 1º x 1º resolution using rain gauges, microwave satellite observations from the Special Sensor Microwave Imager (SSM/I), and infrared satellites observations from many global geostationary satellites [Adler et al., 2003]. The model shows a majority of the simulated AOT confined to the Caribbean and Central America and also simulates precipitation over the Pacific Ocean. Additionally, the simulated 700 mb wind field suggests that the direction of dust transport might shift northward over the Central American coastline.

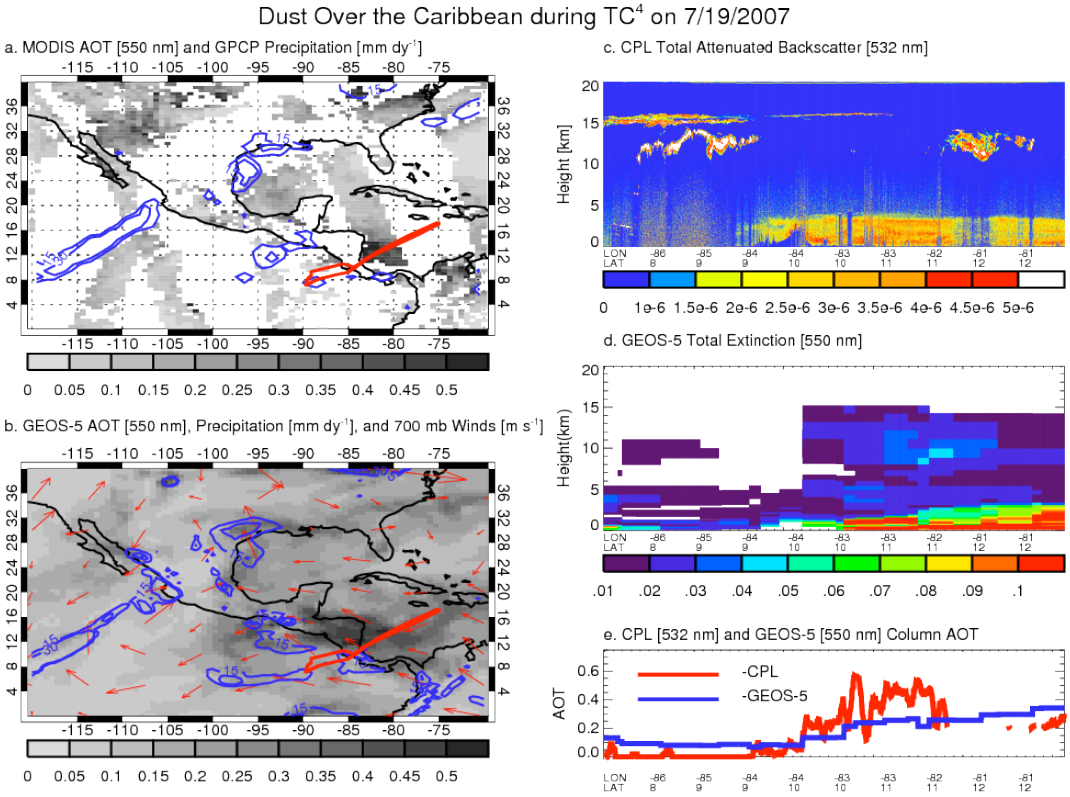

Figure 5.6. MODIS Aqua AOT, GPCP precipitation (blue contour), and ER-2 flight track (red) (a), GEOS-5 AOT, precipitation (blue contour), 700 mb wind field (red arrows), and ER-2 flight track (red) (b), CPL total attenuated backscatter [km^{-1} sr^{-1}] (c), GEOS-5 extinction [km^{-1}] (d), CPL AOT below 5 km (red) and GEOS-5 AOT below 5 km (blue) (e) on 7/19/2007.

The dust barrier is more clearly seen in the CPL profile of the 532 nm total attenuated backscatter and column AOT when compared to GEOS-5 profiles of extinction and AOT at 550 nm that have been sampled along the ER-2 track at the nearest model synoptic time on 7/19 (Figure 5.6). Although the CPL signal is frequently attenuated by clouds over the Pacific and only occasionally over the Caribbean, both CPL and GEOS-5 provide an illustration of the Central American dust barrier along the eastern coastline of Costa Rica (9° N, 84° W, marked by a mountain). To avoid cloud contributions to the AOT, the column AOT from 5 km to the surface is compared for CPL and GEOS-5 (Figure 5.6). CPL observes high AOT values over the Caribbean, and

a sharp decrease in AOT that corresponds with the Central American coastline. A similar feature is seen in the simulated AOT, but at a lower magnitude. Despite this, it is clear that GEOS-5 provides a representation of the Central American dust barrier on this day and suggests two processes that may contribute its cause: removal by precipitation in the tropical environment and a directional shift in the wind field near the Central American coastline.

5.3 Controls on Saharan Dust During Transport

To understand the cause of the Central American dust barrier, the roles of the controls on dust distributions during transport must be understood. During the journey from the Sahara to the Caribbean, dust distributions are controlled by both dynamical and loss processes. Atmospheric dynamics controls the direction and magnitude of the transported dust mass flux or flow, while loss processes control the overall dust burden. Therefore, as suggested by Figure 5.6, it is expected that the Central American dust barrier is caused by increases in wet removal, a change in transport direction resulting from a shift in the prevailing atmospheric dynamics, or some combination of both.

Ideally, airborne measurements that tracked several dust plumes would help in understanding the cause of the Central American dust barrier. Unfortunately, measurements of this sort are extremely limited. However, from comparisons to observations of mean dust plume position and vertical distributions near and downwind of the Saharan source region, GEOS-5 provides a reasonable representation of dust distributions during the TC^4 timeframe, while simulating the aforementioned processes that are not easily measured. The accuracy of the simulated wet removal processes are

directly linked to our ability to accurately simulate the timing and intensity of precipitation events. Figure 5.7 shows the July 2007 mean precipitation from GPCP (mm day^{-1}) and GEOS-5. The precipitation patterns in GEOS-5 are generally consistent with GPCP, matching peak values located over Central and South America. However, GEOS-5 produces a broad area of convective precipitation over the Caribbean that is not seen in the GPCP data. Over the Caribbean, the average GEOS-5 precipitation rate is 5 mm day^{-1} while the average GPCP precipitation rate is 1.5 mm day^{-1}. This presents an interesting feature of the model. Figure 5.2 suggests that the removal rates are not aggressive enough in removing dust, particularly in the region of the Central American dust barrier. However, on average, simulated precipitation rate is greater by a factor of three (Figure 5.7). This quandary suggests that the relationship between precipitation and wet removal is not strong enough in GEOS-5. We could, alternatively, simply rescale the dust emissions lower, which would remove most of the bias seen in Figure 5.2, but this would not produce the abrupt dust barrier evident in the data at approximately 90° W.

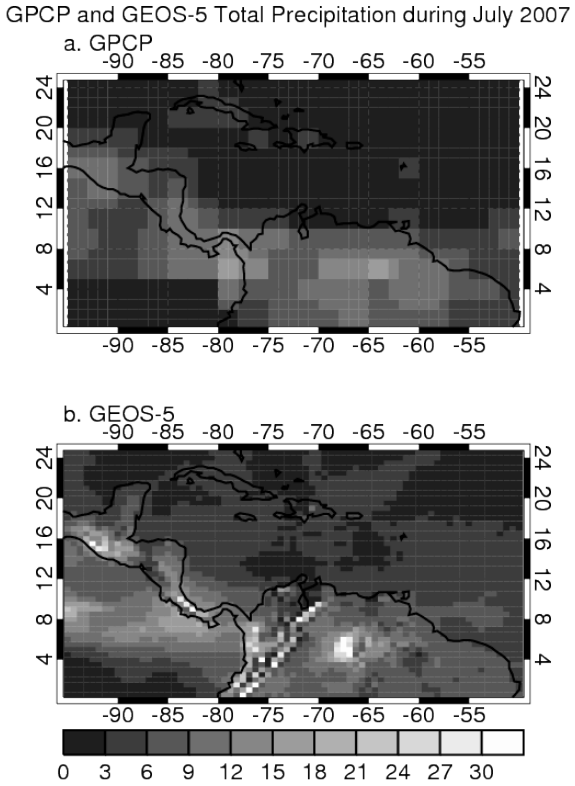

Figure 5.7. July 2007 monthly mean GPCP (a) and GEOS-5 (b) total precipitation [mm dy^{-1}].

In addition to possible errors in the representation of loss processes, the simulated dust distributions are sensitive to atmospheric dynamics. By using a replay simulation, the model is provided with assimilated winds, so that it will be forced with actual dynamics at each synoptic time. The estimation of dust transport is therefore sensitive to the ability to reproduce the actual dynamical state and will be limited by errors in the representations of advection, planetary boundary layer mixing, and convective mixing. In addition to sensitivities to the internal dynamical processes, simulated dust distributions will also be sensitive to the accuracy of observations used in the analysis. Despite these potential sources of error, however, the July 2007 simulated dust loading over the Caribbean is comparable to observations by MODIS (Figure 5.3). Therefore,

dust distributions from GEOS-5 are used to understand the relative roles of the processes that contribute to the Central American dust barrier.

To investigate the controls on the Central American dust barrier, the vertically integrated mass divergence form of the continuity equation for mean values from July 2007 is employed:

$$\frac{\partial q}{\partial t} = (P - L) + \nabla \cdot \vec{Q} \qquad \text{Eq. 5.1}$$

where q is the column dust loading defined:

$$q = \sum_{z=0}^{z=top} \gamma * \rho_a * dz \qquad \text{Eq. 5.2}$$

and $\vec{Q}$ is the vertically integrated dust mass flux:

$$\vec{Q} = \sum_{z=0}^{z=top} \gamma \cdot \rho_a \cdot u \cdot dz \cdot \hat{i} + \sum_{z=0}^{z=top} \gamma \cdot \rho_a \cdot v \cdot dz \cdot \hat{j} \qquad \text{Eq. 5.3}$$

Here, γ is the dust mass mixing ratio (kg kg^{-1}), ρ_a is the atmospheric air density (kg m^{-3}), u and v are the east-west and north-south components of the wind field (m s^{-1}), and dz is the thickness (m) of each model layer in the vertical column.

After integrating in the vertical, Equation 1 has three terms: the storage term ($\frac{\partial q}{\partial t}$), the production-loss (P – L) term, and the divergence, or transport, term ($\nabla \cdot \vec{Q}$). The storage term represents the net local change in the dust column loading, the P – L term is defined as the sum of the column emission fluxes minus fluxes due to dry and wet removal, and the transport term represents any dust column convergence and divergence resulting from transport. All terms in Equation 5.1 are in flux form and have the units (kg

m^{-2} s^{-1}). Equation 5.1 can be interpreted as any accumulation of dust mass within an atmospheric column results from the sum of the net production minus loss and dust import/export via transport.

To relate the contribution of transport to Equation 5.1, the vertically integrated dust mass flux $\vec{Q}$ (kg m^{-1} s^{-1}) is used again (Equation 5.3). Because dust is typically located at low altitudes, $\vec{Q}$ will be weighted toward the mass concentration and the near-surface wind direction and magnitude.

Consider the Helmholtz decomposition [Brown, 1991]:

$$\vec{Q} = \vec{Q}_{rot} + \vec{Q}_{div} \qquad \text{Eq. 5.4}$$

where $\vec{Q}_{rot}$ and $\vec{Q}_{div}$ are the rotational and divergent components of the vertically integrated mass flux vector $\vec{Q}$, with $\nabla \cdot \vec{Q}_{rot} = 0$ and $\nabla \times \vec{Q}_{div} = 0$ by definition. The corresponding mass flux streamfunction ψ and velocity potential χ can be obtained by solving Poisson's equations [Brown, 1991]:

$$\nabla^2 \Psi = \nabla \cdot \vec{Q}_{div} \qquad \text{Eq. 5.5}$$

$$\nabla^2 \chi = \hat{k} \cdot \nabla \times \vec{Q}_{rot} \qquad \text{Eq. 5.6}$$

from which the divergent and rotational components of $\vec{Q}$ may be obtained:

$$\vec{Q}_{rot} = -\frac{\partial \Psi}{\partial y}\hat{i} + \frac{\partial \Psi}{\partial x}\hat{j} \qquad \text{Eq. 5.7}$$

$$\vec{Q}_{div} = \frac{\partial \chi}{\partial x}\hat{i} + \frac{\partial \chi}{\partial y}\hat{j} \qquad \text{Eq. 5.8}$$

The rotational component depicts the recirculation of dust in the atmosphere, while the divergent component of the vertically integrated mass flux is associated with the P – L process ($\nabla \cdot \vec{Q}_{div} = \nabla \cdot \vec{Q}$) (Equation 5.1).

5.3.1 Dust Mass Budget

In this section, the July 2007 monthly mean storage, P – L, and transport terms are analyzed. Each term is analyzed separately to understand their respective influence on the simulated dust distributions over the Caribbean. Equation 5.1 uses instantaneous model output at every 3 hours to determine the monthly mean dust mass fluxes; thus, the fields examined include both the mean flow and the contribution from transient eddies.

5.3.1.1 Storage Term

At each grid cell, the storage term represents the mean local change in the column dust loading q (kg m^{-2}) (Equation 5.2). During July 2007, the largest variations in the dust column loading occur away from regions of semi-persistent dust flow (Figure 5.8). This can be seen north of 20° N off the west coast of North Africa during July 2007, where removal rates are small (Figure 5.8). Eventually, this dust will be removed from the atmosphere via loss processes or transport. Over the Caribbean, the storage term is significantly less than the P – L and transport terms, indicating that the other terms are in near-balance over this region. Over longer time periods, the storage term is expected to approach zero, as deviations in the mean dust flow will become less significant and averaged out. In this case, the P – L term will balance the transport term.

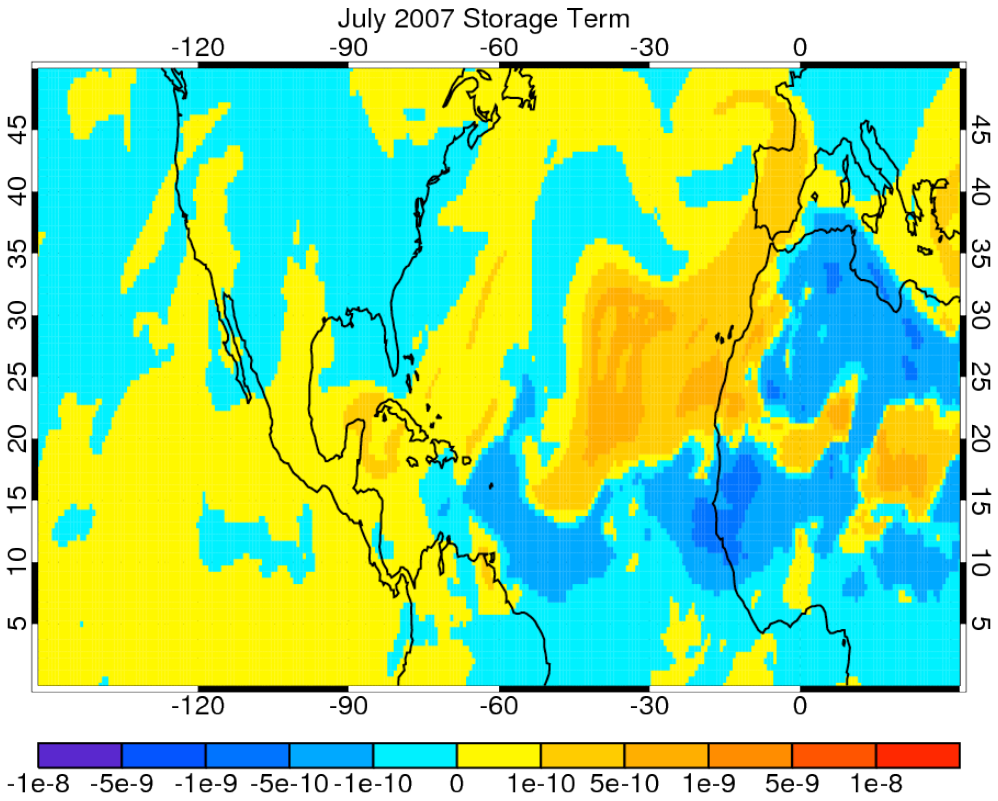

Figure 5.8. July 2007 storage term (kg m^{-2} s^{-1}) .

5.3.1.2 Production Minus Loss Term

The mean P – L term for July 2007 shows positive values over the global source region and negative values downwind, corresponding to regions where emissions and losses prevail, respectively (Figure 5.9). Once dust is emitted from the source region, the total atmospheric burden is controlled by losses through dry and wet removal processes. In the Atlantic, losses peak immediately downstream of the source region, although a broad area of high dust losses carries into the Caribbean.

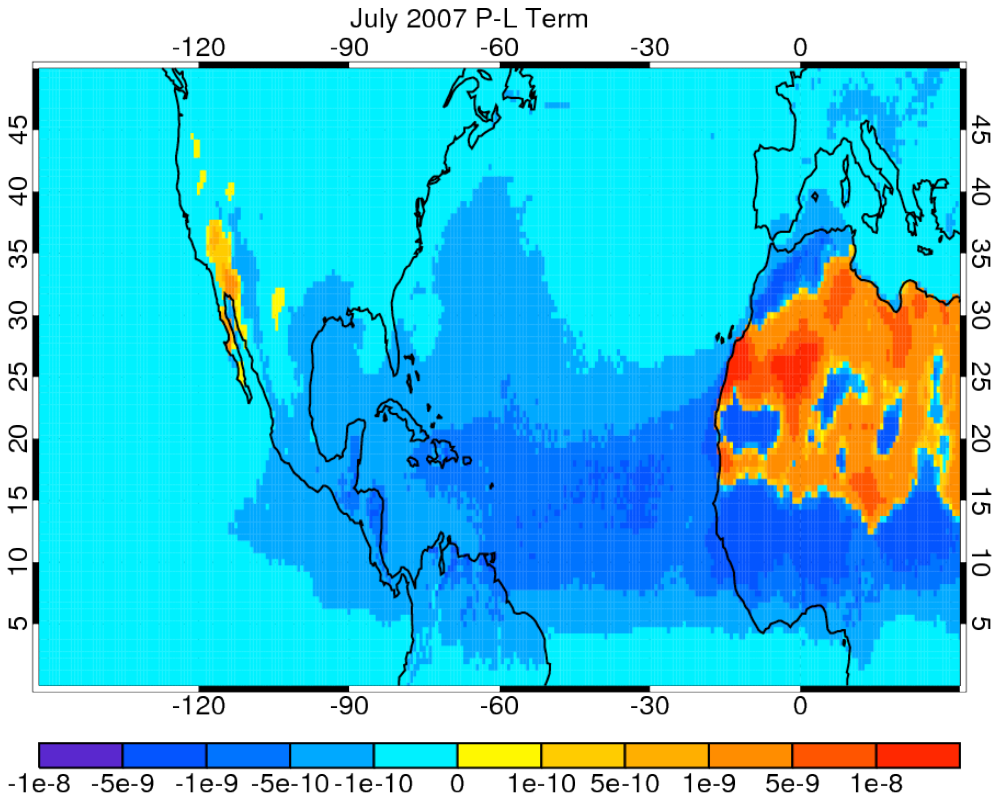

Figure 5.9. July 2007 production minus loss (P – L) term (kg m^{-2} s^{-1}).

Figure 5.10 shows the relative contributions from modeled dust loss processes during transport from the source region. Dry removal (dry deposition + sedimentation) is the dominant removal process near the Saharan source region, as the largest, most massive dust particles fall quickly from the atmosphere. Dry removal becomes less significant further downwind as the largest particles are removed. Wet removal becomes the dominant loss process, first via large-scale precipitation immediately west of the source region and then through convective precipitation in the western Caribbean and near Central America. This region where convective removal dominates coincides with the location of the Central American dust barrier.

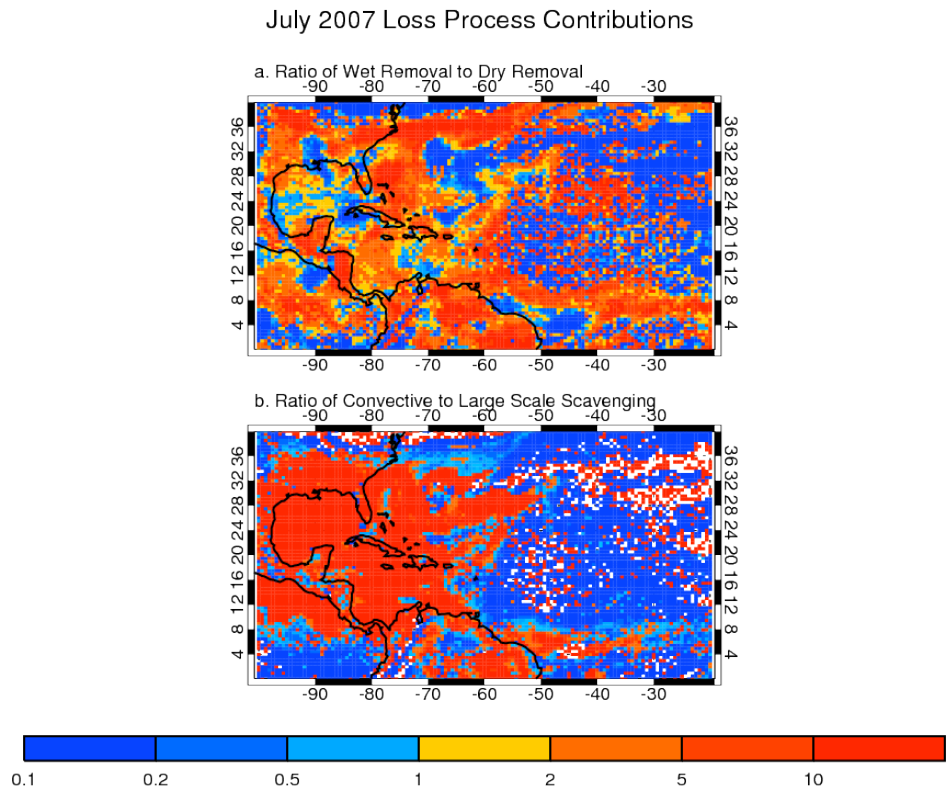

Figure 5.10. (a) July 2007 ratio of wet removal to dry removal and (b) ratio of convective to large scale scavenging.

5.3.1.3 Transport Term

Shown in Figure 5.11 are the July 2007 mean streamfunction and velocity potential contours with the rotational and divergent dust flow vectors overlaid. Recall that the rotational component of the dust flow is proportional to the curl of the streamfunction; therefore, rotational flow will be strongest where streamlines are closest. By definition, the rotational flow will be cyclonic surrounding relative minima of the streamfunction, and anti-cyclonic surrounding the relative maxima. There is strong rotational dust flow leaving the Sahara as part of the SAL and riding on the northern side (15° – 25° N) of the AEJ across the Atlantic Ocean. In this region, the rotational component of the dust flow is strong for two reasons: 1) dust concentrations are high

within the SAL and 2) strong, non-divergent easterlies within the AEJ persist. The effect is a narrow band (15° – 25° N) of strong rotational flow that transports dust from the Sahara to the Caribbean. Upon reaching the Caribbean, the rotational flow weakens because: 1) dust loss processes have reduced the overall dust load during transport and 2) easterly wind speeds are reduced. Additionally, the flow direction shifts from primarily westward to north-westward over the Caribbean due to a channeling of the dust flow by the topography of northeastern Brazil and the clockwise rotation of the Azores subtropical high-pressure system that exists of the Atlantic Ocean. The rotational dust flow eventually turns eastward and returns dust back to the Saharan source region. Thus, when following a constant streamline, the rotational component of Saharan dust flow is an anti-cyclonic recirculation, where dust leaves the source region as part of the AEJ and returns with the westerlies as part of the Azores High. A similar—but weaker—cyclonic feature is seen south of 15° N, transporting dust to South America.

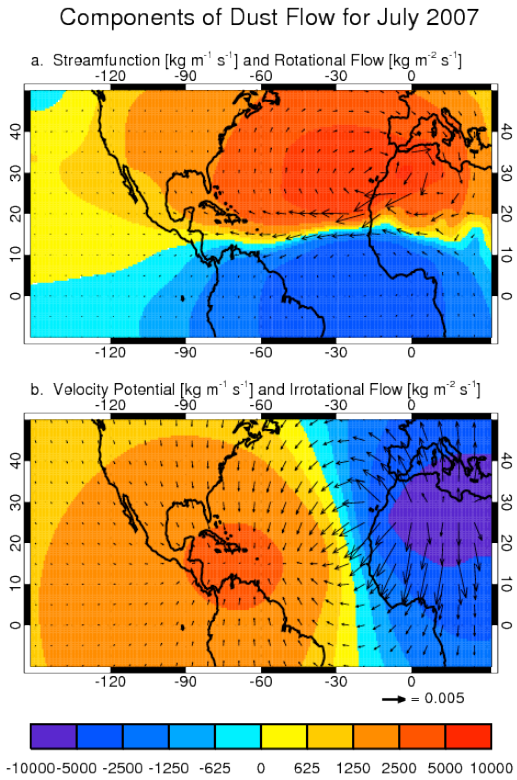

Figure 5.11. July 2007 mean streamfunction (a) and velocity potential (b). Rotational (top) and irrotational (bottom) flows are indicated by vectors.

The divergent component of the flow is proportional to the gradient of the velocity potential. Therefore, regions of divergence correspond to relative minima of the velocity potential correspond, while regions of convergence correspond to relative maxima. In Figure 5.11, there is a dipole in the divergent flow field between the Saharan source region and the Caribbean. Over the source region strong divergent flow persists, as a divergent component to the dust flow is required for dust to leave the source region. During transport, the divergent flow is significantly reduced and there is a broad, region of convergence over the Caribbean where loss processes prevail. The significant reduction in the divergent flow can be the result of a weakening of the wind field or a reduction in the dust burden caused by the various loss processes during transport. As

previously mentioned, the divergence of the divergent flow ($\nabla \cdot \vec{Q}_{div}$) is the transport term in Equation 5.1. In Figure 5.12, as expected, the July 2007 transport term is positive (divergent) over the source regions, as dust is transported outward from the sources. Downwind of the Saharan source region, the transport term is negative (convergent), which corresponds with the convergent flow field in Figure 5.11. One striking feature of the divergence field is that it aligns with the P – L term in regions where production and loss occur. Because these regions have a semi-persistent flow of dust for this month and the storage term is small, there is a near-balance between the transport and P – L terms. Thus, over these regions, regions of dust emission (P – L > 0) correspond with divergent outflow (positive transport term) and regions of dust loss (P – L < 0) correspond with convergent inflow (negative transport term). It is expected that convergent flow increases dust loss rates in two ways. First, the convergent flow will accumulate dust within the atmospheric column. This accumulation will increase the potential for removal in regions where the storage term is small. Second, there is vertical motion over convergent regions (not shown), which is associated with convection. This second process is more relevant for wet removal as it is related to greater wet deposition and scavenging rates in the presence of precipitation and clouds.

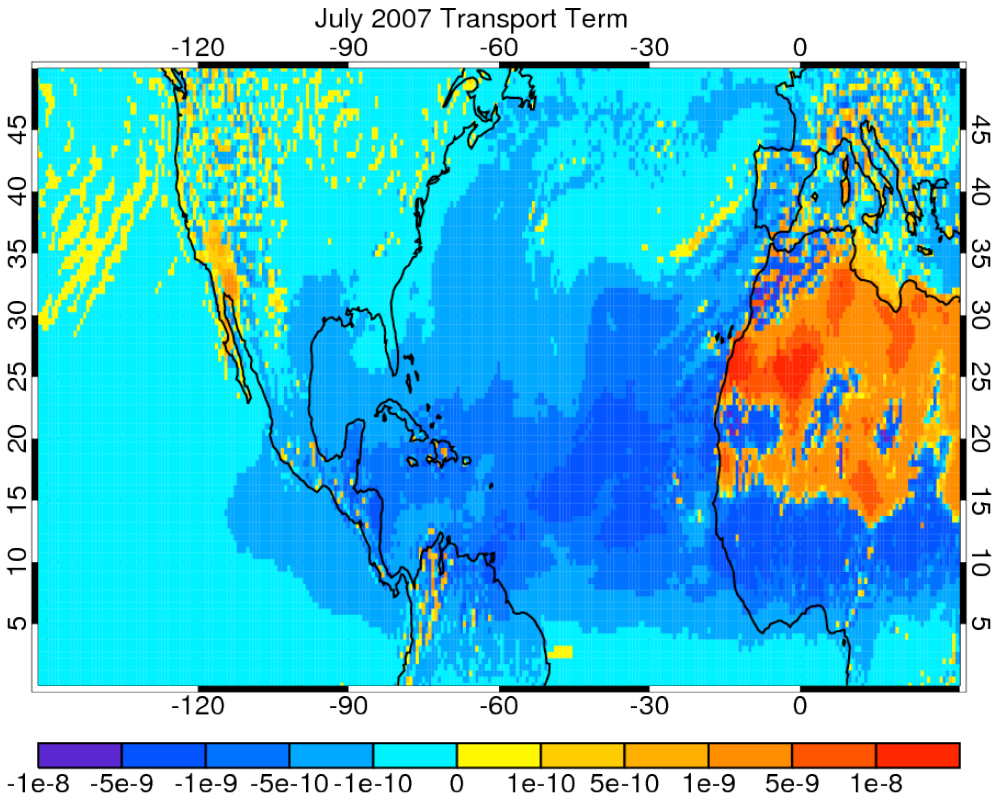

Figure 5.12. July 2007 transport term (kg m^{-2} s^{-1}).

Despite the link between P – L and divergent flow, it is clear that rotational flow has a greater magnitude and is in a different direction (predominantly westward) than the divergent flow (predominantly eastward). However, this alone does not lend much insight into any influences that transport might have on the Central American dust barrier. In addition to the effects of loss processes, the dust barrier could be influenced by a slight change to the flow field over the Caribbean or a combination of the rotational and divergent components. To better understand this, the rotational and divergent components are further broken into their east-west and north-south components. Figure

5.13 shows the east-west and north-south total, rotational, and divergent flow components. Over the Caribbean, the rotational component of the east-west flow is strongly westward while the divergent component is weakly eastward. Despite cancellation between the two components near the coast of Costa Rica, the net east-west flow is westward and acts to transport dust across Central America. The north-south flow for the rotational component shifts from southward to northward near 12.5° N over the Caribbean, while the divergent flow shifts from northward to southward flow at 17.5° N. However, the net north-south flow is northward over the entire Caribbean. Thus, there is a northward turning of the dust flow as it enters the Caribbean, which when combined with the net westward flow causes a northwestern migration of the overall dust flow and serves as a possible explanation of the Central American dust barrier.

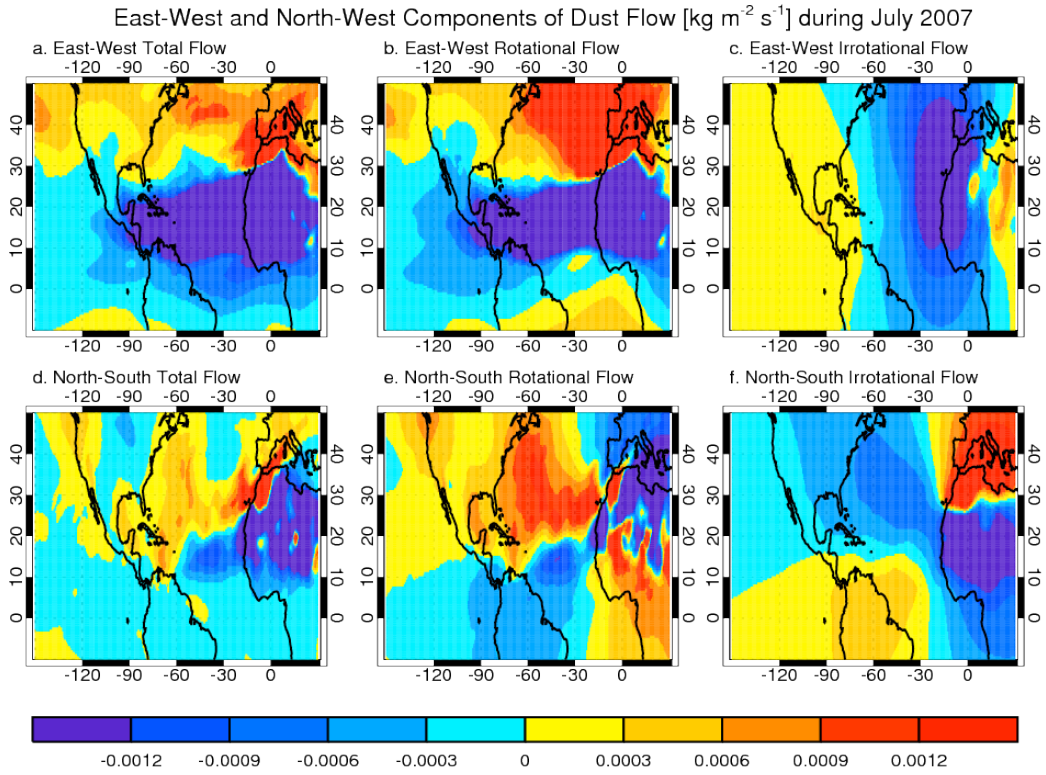

Figure 5.13. East-west (top) and north-south components (bottom) of the total (left), rotational (center), and divergent (right) flow.

5.3.2 Loss Processes vs. Transport

The dust mass budget is investigated over the latitude band of peak dust AOT (10° – 20° N) to understand the relative roles of dust loss processes and transport in the Central American dust barrier. Figure 5.14 shows the mass of dust removed from loss processes, from transport out of the northern (20° N) and southern (10° N) sides of the latitude band, and the change in the east-west mass flux (flux in minus flux out) as a function of longitude. To obtain the amount of dust lost via removal, the P – L rates are integrated spatially and temporally and sum over the latitude band at each longitude (black curves in Figure 5.14). To quantify the net north-south dust mass flux out of the band, the net spatially and temporally integrated north-south dust flux at 20° N is

subtracted from that at 10° N at each longitude (Figure 5.14). To obtain the change in the east-west mass flux, the net east-west component of the dust flow is first integrated spatially and temporally at each grid box. The change in the east-west mass flux is then determined by differencing the east-west flow in the westward direction and then summing along all latitudes (Figure 5.14). Negative mass values in Figure 5.14 correspond with net loss via removal processes or transport out of the latitude band, or a reduction in the westward mass flux. It should be noted that the sum of the net north-south mass flux and the change in the westward mass flux is the divergence term in Equation 5.1. This sum is approximately equal to the mass of dust removed by loss processes, with any residual related to the storage term.

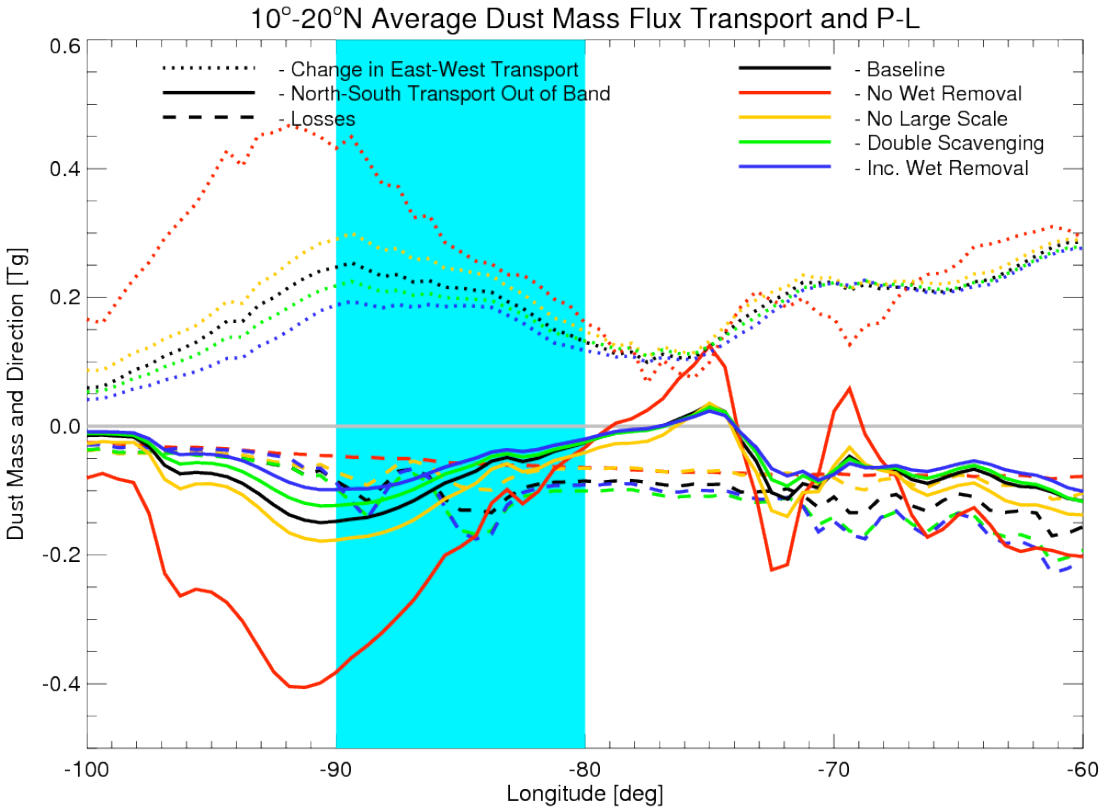

Figure 5.14. 10º-20º N July 2007 mass budget for our baseline (black), no wet removal (red), no large-scale scavenging (orange), doubled scavenging (green), wet removal treated as other aerosols (blue) sensitivity tests. Shaded region indicates integration region for the Central American dust barrier.

Over the Caribbean, removal from loss processes and northward transport were shown to serve as possible causes of the Central American dust barrier. In Figure 5.14, the longitudes of the Central American dust barrier (80° - 90° W) correspond with increases in dust mass loss and northward transport. To quantify their relative contributions, the production-loss and north-south transport curves in Figure 5.14 are integrated over the region of the Central American dust barrier. From this, it is estimated that loss processes remove 1.67 Tg of dust while the north-south dust flow transports 1.46 Tg of dust out of the Central American dust barrier region during July 2007.

Based on these estimations, it is clear that both loss processes and atmospheric dynamics have a contribution to the Central American dust barrier. Of the two processes, dust loss from removal processes has a slightly greater contribution (53%) to the Central American dust barrier than northward transport (47%).

5.4 Discussion

Loss processes have a greater contribution towards the Central American dust barrier than northward transport for July 2007. From Figure 5.10, it is clear that wet removal by large scale and convective scavenging dominate the loss processes downwind of the Saharan source region between 10° – 20° N and serve as the major pathways for dust removal over the Caribbean. However, as discussed in Section 5.2, it was suggested that the GEOS-5 wet removal rates are not aggressive enough over the Caribbean and serves as the cause of our weaker representation of the Central American dust barrier in Figure 5.2. To explore the controls of wet removal on our transported dust distributions,

additional simulations of July 2007 were performed where the parameterization of wet removal processes was modified relative to our baseline simulation setup.

Table 5.1 presents a budget analysis for our baseline simulation and the sensitivity experiments. Included are the dust mass removal by loss processes, north-south transport, and their contribution to the Central American dust barrier. Also shown are the 10° – 20° N net east-west mass transported across the planes at 80° W and 90° W and their difference. This difference, when combined with the north-south transport is the mass divergence and should approximately balance the mass removed by loss processes, with any residual attributable to the storage term in Equation 5.1. Table 5.1 lists a dust mass barrier efficiency of the Central American dust barrier defined as the difference between the 10° – 20° N net east-west transported dust mass at 80° W (flow in) from that at 90° W (flow out) divided by the transported dust mass at 80° W (flow in). Additionally, after sampling consistently with MODIS-Terra, Table 5.1 lists a total AOT barrier efficiency and a coarse mode (dust plus sea salt) AOT efficiency that can be compared to the MODIS coarse mode AOT after averaging from 10° – 20° N.

Experiment/Satellite	Net Northward Mass Transport (Tg) and Barrier Contribution (%)	Net Mass Loss from Removal (Tg) and Barrier Contribution (%)	80° W, 90° W, and Net Change in Westward Transport (Tg)	Barrier Efficiency		
				Mass	Total AOT	Coarse Mode AOT
1. Baseline	-1.46 | 47%	-1.67 | 53%	-7.58 | -4.21 | 3.37	0.36	0.21	0.17
2. Doubled Convective Scavenging	-1.24 | 39%	-1.90 | 61%	-6.51 | -3.40 | 3.11	0.48	0.25	0.21
3. Wet Removal Treated As Other Aerosols	-1.02 | 34%	-1.97 | 66%	-5.42 | -2.60 | 2.82	0.52	0.28	0.22
4. No Large Scale Scavenging	-1.85 | 59%	-0.95 | 41%	-9.76 | -6.88 | 3.87	0.33	0.19	0.16
5. No Wet Removal	-3.35 | 78%	-1.28 | 22%	-18.73 | -13.96 | 4.77	0.25	0.17	0.13
6. MODIS-Terra					0.37	0.30

Table 5.1. Net northward mass transport and mass loss from removal and relative contribution, westward mass transport at entrance and exit of barrier region, and mass, total AOT, and coarse mode barrier efficiencies for all simulations and MODIS-Terra.

The baseline simulation has a dust mass barrier efficiency of 0.36, meaning that the Central American dust barrier removes 36% of the dust mass between 80° W to 90° W (Table 5.1). The baseline simulation has a total AOT barrier efficiency of 0.21 and a coarse AOT efficiency of 0.17. Comparisons to MODIS-Terra show that the removal rates are not aggressive enough, as MODIS-Terra has a total AOT barrier efficiency of 0.37 and coarse AOT barrier efficiency of 0.30 (Table 5.1).

Because GEOS-5 does not include a detailed representation of aerosol-cloud-precipitation interactions, aerosol wet removal is parameterized in terms of the model grid box convective updraft mass flux (for convective scavenging) and precipitation rate (for large scale wet removal). An efficiency factor is assigned to each aerosol species

that represents its susceptibility to wet removal (i.e., its hygroscopicity) [Colarco et al. 2010]. For the baseline simulation, the dust wet removal efficiency is assumed to be approximately half the efficiency as for hydrophilic carbonaceous and sulfate aerosols. In the first sensitivity test, the dust convective scavenging efficiency was doubled so that it is equivalent to that for hydrophilic aerosols. In Figure 5.14, doubling the convective scavenging rate increases the mass of dust lost to removal while reducing the north-south and east-west dust flow. After integrating along the longitudes of the Central American dust barrier, doubling the convective scavenging rate increases the loss contribution to 61% (1.90 Tg) and reduces the contribution by northward transport to 39% (1.24 Tg), increasing the mass barrier efficiency to 0.48 (Table 5.1). Figure 5.15 shows the MODIS-Terra sampled AOT from the baseline and sensitivity experiments, the ratio of the MODIS-Terra and simulated AOT, and the slope of the AOT ($\Delta\tau/\Delta x$). After doubling the convective scavenging rate, there is a reduction in the high AOT bias in the model and improvement in the slope of AOT as a function of longitude (Figure 5.15). This corresponds with a significant improvement in the representation of the Central American dust barrier as the simulated AOT reduces from 0.34 at 80° W to 0.25 at 90° W (Figure 15). This corresponds to greater AOT barrier efficiencies of the total (0.25) and coarse (0.21) representations of the Central American dust barrier.

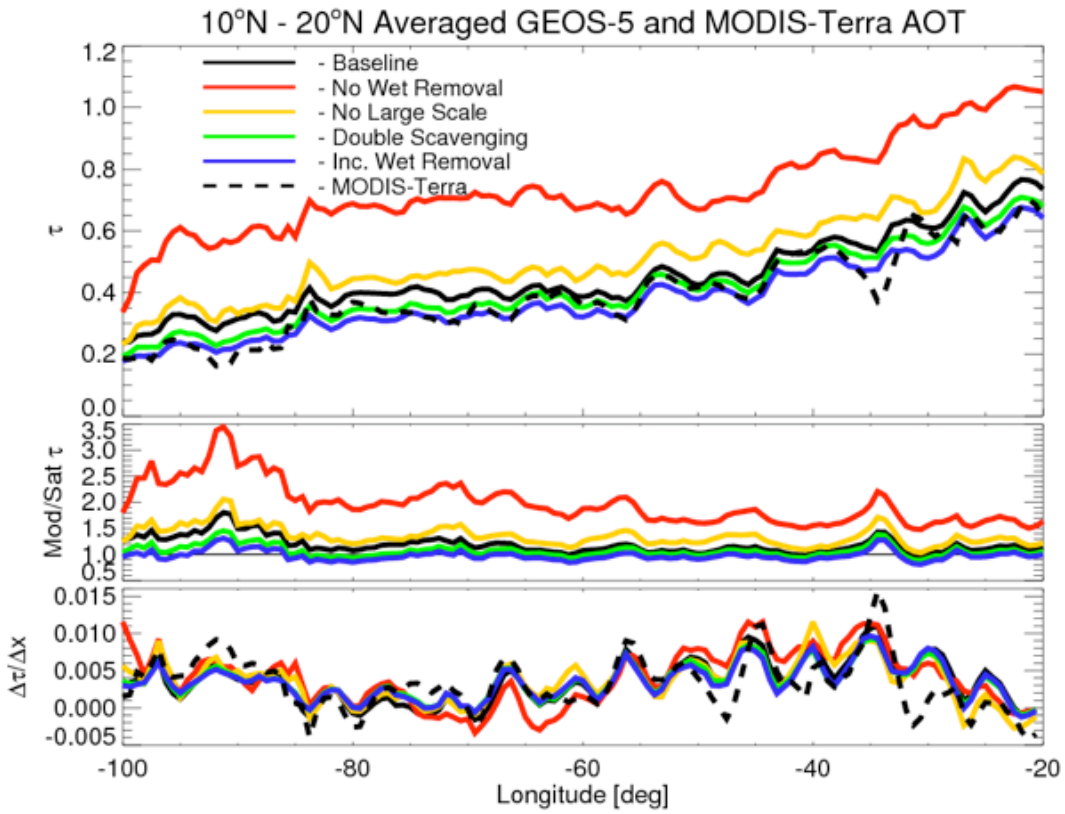

Figure 5.15. 10° N - 20° N averaged AOT, model to satellite AOT ratio, and AOT slope for MODIS-Terra (black-dashed) and sampled baseline (black-solid), no wet removal (red), no large-scale scavenging (orange), doubled scavenging (green), and wet removal treated as other aerosols (blue) sensitivity tests. The thin black line indicates the one-to-one line for ratio plots.

A second sensitivity test was performed where in addition to doubling the dust convective scavenging rate, large-scale scavenging rate was increased so that dust wet removal is treated the same as for hydrophilic aerosols. While this further increases the mass of dust lost to removal and reduces the north-south and east-west flow (Figure 5.14), it is evident that simulated dust distributions are more sensitive to modifications to convective scavenging than large-scale scavenging in this region. However, the combined effect of increasing the large-scale and convective scavenging rates consistent with other aerosol types corresponds with an increased contribution from loss processes (66%, 1.97 Tg), a reduced contribution (34%, 1.02 Tg) from northward transport, and an

increase in the barrier mass efficiency (0.52) of the Central American dust barrier (Table 5.1). Treating the wet removal of dust the same as other aerosols yields further improvement in the representation of the AOT magnitude and slope when compared to MODIS-Terra (Figure 5.15). Over the region of the Central American dust barrier, the simulated AOT reduces from 0.31 at 80° W to 0.23 at 90° W (Figure 5.15), corresponding with an improved total AOT barrier efficiency of 0.28 and a coarse AOT barrier efficiency of 0.22 (Table 5.1). Although still not as efficient as indicated by MODIS-Terra, this result suggests that the baseline dust wet removal rates in GEOS-5 are too slow and treating the wet removal of dust in a fashion similar to other (more ostensibly hygroscopic) aerosol types yields better comparisons to observations in regions where wet removal is dominant. Because the representation of the dust barrier improves with increases to the wet removal rates, the contribution from loss processes to the Central American dust barrier is likely greater (66%) than originally estimated from our baseline simulation (53%).

Two additional sensitivity tests were performed, aimed at understanding whether the Central American dust barrier persists when the effects of convective and large-scale scavenging are not simulated. In the first sensitivity test, wet removal from the large-scale scavenging of dust was not simulated, leaving only convective scavenging as a source of wet removal. As shown in Figure 5.14, large-scale scavenging over the Caribbean has a small effect on the dust load, as the northward and westward flows are slightly increased and losses are reduced when the effects of large-scale scavenging are not simulated. After integrating over the longitudes of the Central American dust barrier, there is a shift in the relative significance of northward transport and loss. Northward

flow transports 1.85 Tg of dust out of the region (59% of the total removal) while dust losses remove 0.95 Tg of dust (41% of the total removal), corresponding with a barrier mass efficiency of 0.33 (Table 5.1). When the AOT is sampled consistent with MODIS-Terra, there is a small increase in the magnitude of the AOT and slope from the coast of North Africa (20° W) to Central America (80° W), but there is still evidence of a Central American dust barrier (Figure 5.15). When the effects of large scale scavenging are not simulated, the total AOT efficiency and coarse AOT efficiency decrease to 0.19 and 0.16, respectively (Table 5.1). This result is consistent with the simulations already discussed and suggests that large-scale convective scavenging has a small effect to the Central American dust barrier.

In a final sensitivity test, a simulation was conducted where the effects of all wet removal (convective scavenging and large-scale scavenging) were not simulated. In Figure 5.14, there is a large increase in the northward and westward dust flows and a significant reduction in the dust loss. Over the Central American dust barrier region, northward transport accounts for 78% (3.35 Tg) of dust removal from the atmospheric column, while loss processes account for 22% (1.28 Tg), corresponding with a mass barrier efficiency of 0.25 (Table 5.1). When compared to MODIS-Terra, there is a nearly constant increase in the AOT from the coast of North Africa (20° W) to the beginning of the Caribbean (60° W) (Figure 5.15). However, over the Caribbean where convective scavenging has the largest contribution to the overall removal (Figure 5.10), the model AOT relative to MODIS-Terra increases non-linearly (Figure 5.15) and reduces the total and dust AOT barrier efficiency to 0.17 and 0.13, respectively (Table 5.1). Finally, when all wet removal processes are not included, there is no evidence of the Central American

dust barrier (Figure 5.15). Therefore, it can be determined that the Central American dust barrier could not exist without convective scavenging. In practice, however, the Central American dust barrier is the result of two processes working in tandem: 1) Loss processes significantly reducing the dust loading during transport and 2) Atmospheric dynamics redirecting the reduced dust flow northward near the Central American coastline.

5.6 Conclusions

GEOS-5 was used to understand the processes that contribute to the Central American dust barrier during transport from the Saharan source region to the Caribbean for the period of the NASA TC^4 field campaign (July – August, 2007). Near the Saharan source region, GEOS-5 has a similar plume shape to the MODIS observations, but the baseline simulation overestimated the AOT. Over the Caribbean, our GEOS-5 AOT magnitude is comparable to MODIS, but provided a weaker representation of the Central American dust barrier. This result suggested that loss processes be explored and possibly adjusted in future implementations of the model.

In a series of sensitivity analyses with GEOS-5, the relationship between wet removal parameterization and transport was explored in defining the Central American dust transport barrier. The best agreement between GEOS-5 and the observations was obtained when dust wet removal was treated as the removal of hydrophilic aerosol species. This result is supported by observations of negatively charged silicates [Yu et al., 1997] in unprocessed dust aerosols attracting hydrogen in water [Koretsky et al., 1997] to readily serve as a CCN [Kumar et al., 2009]. Additionally, this result is supported by observations of dust aerosols mixing with other hydrophilic aerosol species

such as sulfates, sea-salt, and black carbon [Chen et al., 2010, Clarke et al. 2004]. This analysis shows that both wet removal and transport play a role in creating a semi-permeable barrier to dust transport across Central America into the Pacific. Of the two processes, for the best-case simulation, wet removal has a factor of two greater contribution toward defining the barrier than northward transport. Moreover, of the wet removal processes, the Central American dust barrier is more sensitive to removal by convective scavenging and is not evident when convective scavenging is not simulated.

These results should be taken with a few caveats. First, the component analysis is valid for July 2007. While it was shown that the Central American dust barrier is a persistent feature in July (Figure 5.2), it can be expected that the barrier will be somewhat sensitive to the variability of inter-annual meteorological conditions over the Central American region. Transported dust distributions will be sensitive to variability in Saharan dust emissions, AEJ strength, and Inter-Tropical Convergence Zone (ITCZ) position. Prospero and Lamb [2003] showed that dust transported from the Sahara to the Caribbean is linked to Sahel precipitation from the previous year. Additionally, Pfister [2010] found that the La Nina conditions in 2007 caused an increase in westward flow and a significant reduction in Caribbean cold clouds and corresponding increase in Pacific cold clouds during the TC^4 field campaign. This suggests that under normal conditions, transported dust would be more confined the Caribbean and the Central American dust barrier would have a greater presence. Inter-annual variability in the Central American dust barrier has implications for equatorial aquatic ecosystems located to the west of the Central American coastline. In this region, low phytoplankton growth inferred from chlorophyll concentration observations during July [Falkowski et al.,

1998], suggest that the Central American dust barrier serves as a natural inhibitor of carbon sequestration in the Pacific. Additionally, the Central American dust barrier is expected to exist only in summer months. The AEJ forms during northern hemisphere summer and corresponds with peak dust transport from the Sahara to the Caribbean. Analysis of the MODIS-Terra 2000 – 2010 monthly climatology suggests that transported dust loadings are too low to see evidence of a Central American dust barrier during non-summer months.

Another caveat is that the role of dry removal processes in establishing the Central American dust barrier were not explored, though similar to wet removal, dry removal rates are not well constrained by data. Additionally, compensating effects in removal rates were neglected when removal processes were modified in the sensitivity studies. However, by mass, dry removal becomes less important with distance from the source region. Offline analysis confirmed this, as dry removal rates from the no wet removal simulation increased by a factor of 1.3 when compared to our baseline simulation over the region of the Central American dust barrier.

One final caveat is that the strength of the results is limited by how well transport and loss processes are represented in the model. The effect of transport on the Central American dust barrier will be sensitive to the accuracy of the meteorology used to drive transport (i.e. MERRA reanalyses), as well as the internal dynamics of the model that advect dust in-between analyses. Therefore, the role of transport towards the Central American dust barrier may be different in another global aerosol transport model. This analysis also relies heavily on the ability of the model to provide a realistic representation of convection, which subsequently influences wet removal over the Caribbean. Because

wet removal rates are not typically measured in the field, it is difficult to determine whether our parameterization of wet removal is accurate and therefore we are limited to relying on proxies, such as column AOT. As previously discussed, the baseline simulation provided a weak representation of the Central American dust barrier when compared to MODIS-Terra, suggesting that the wet removal rates were too relaxed in the model (Figure 5.2). However, when compared to the GPCP observations, the July 2007 mean GEOS-5 precipitation was slightly greater over most of the Caribbean (Figure 5.7). These results suggest that the connection between wet removal and precipitation should be strengthened in GEOS-5, in particular that the simulation which best captured this dust barrier was the one that treated dust the same as hygroscopic aerosol species with respect to wet removal processes, suggesting that the best representation of dust in our model is one which allows that dust has mixed or been processed so as to be more hydrophilic.

Chapter 6: Conclusions and Future Work

6.1 Conclusions

In this work, the effects of source, transport, and removal processes on the dust aerosol lifecycle were investigated. Using the NASA GEOS modeling system as a tool, simulations were performed to understand the sensitivity of simulated dust aerosol lifecycle to various treatments of dust mobilization and removal, as well as model spatial resolution. Several results from this analysis have brought insight into the treatment of dust aerosols within a global modeling framework and are relevant to the global aerosol modeling community as it transitions from coarse, multi-year climate simulations toward including aerosols as part of high resolution forecasting efforts.

One of the first issues addressed in this work pertained to the treatment of the dust mobilization process, specifically testing the implications of using a more physically based mobilization parameterization in a global aerosol transport model. A major result from that analysis was that despite using different meteorology to parameterize dust emission, the mobilization scheme choice is significant for considerations of the emitted dust mass and particle size distribution. This result was found by comparing simulated Saharan dust distributions driven by versions of the GOCART and DEAD mobilization schemes. Due to the lack of global observations of dust emissions, the simulations were tuned to achieve the same dust AOT over the Saharan source region during the NAMMA field campaign. It was therefore not surprising that simulated dust AOT magnitudes were comparable, however, different meteorology used to parameterize dust emissions did not significantly influence the timing of simulated dust events. For the time period

considered, both schemes were more comparable to one another when compared to observations and had better agreement with observations with distance from the Saharan source region. Because the simulations were tuned to have the same dust AOT, differences in the treatment of the emitted particle size distributions led to differences in the emitted dust mass and particle size distributions.

One of the major limitations of the GOCART scheme is that it parameterizes dust emission by comparing 10-meter wind speed to threshold wind speeds that have been determined for dust aerosols, rather than soil particles. Because the 10-meter wind speed is an order of magnitude greater than the threshold wind speeds, it freely emits dust over regions permitted by the source function. The mobilizing physics of the DEAD scheme is more physically satisfying by comparing the surface friction speed to a threshold for soil-sized particles for computing a saltating mass flux, but is limited by neglecting variability in the parent soil particle bed. Both schemes are limited by how well the model determines surface wind speeds used to parameterize dust emission. Neither the 10-meter wind speed nor the surface friction speed are directly assimilated, but rather are computed by the land surface model constrained by the dynamical state provided by the analysis. Future work entails exploring the sensitivity of the results of Chapter 4.2 to different meteorological analyses, as discussed further in the next section.

While exploring the effects of model spatial resolution on parameterizations of dust mobilization, a third scheme was introduced that blended aspects of the GOCART and DEAD schemes. Emissions were parameterized by comparing the 10-meter wind speed (similar to GOCART) to a soil particle threshold extrapolated to 10-meters (similar to DEAD) so that the driving winds and threshold are the same order of magnitude.

While this parameterization does not consider the stability of the atmosphere when determining the mobilization threshold, it produces a seasonal cycle of dust emissions that is similar to DEAD (i.e. more variability) by using winds that are better constrained (10-meter wind speed). However, until observations of dust emission are available to constrain simulated dust distributions in terms of both mass and optical properties, simulated dust emissions are limited to being tuned in terms of AOT, making it difficult to determine which scheme provides a better parameterization of dust emission physics.

Another major result was that simulated dust distributions are highly sensitive to model spatial resolutions and should be considered when tuning dust emissions. Surface wind speeds used to parameterize dust emission were shown to increase with model spatial resolution, though there was evidence of convergence at higher spatial resolutions. The cubic dependence of dust mobilization on the surface wind speed led to significant increases in dust emissions and corresponding AOT magnitudes that were substantially greater than those caused by different treatments of the mobilization process. Conversely, the resolution of the dust source function was shown to have only a minor effect on simulated dust emissions. Over major dust source regions, increasing the model spatial resolution improved the timing of simulated dust events. However, the effect of model spatial resolution did not significantly influence dust distributions downwind of the source region as the simulated dust aerosol lifetime decreased with increases in resolution.

A third major result was that dust emissions should be tuned regionally in global aerosol transport models. Simulated dust distributions exhibited different biases and responses to increases to model spatial resolution over the African and Asian source

regions for April 2008. Over the African source region, simulated AOT values were comparable to observations at coarse resolutions and increased almost linearly with spatial resolution, obtaining a high bias. Over the Asian source region, AOT values were biased low at coarse resolution, and exhibited a non-linear response at higher resolutions that became more comparable with observations. To improve the representation of dust emission at coarse resolutions, the effect of incorporating sub-grid wind variability was explored. This led to improved comparisons with AOT magnitude, though the timing of simulated dust events was unaffected. Because this analysis was only conducted for one month, future work involves exploring the sensitivities of dust emissions over different regions and various resolutions for longer periods of time.

Two major results arose while exploring the role of transport and loss processes in defining the summertime Central American dust barrier. Compared to observations, the model reproduced the observed location and magnitude of dust transport, but the baseline simulation provided a weaker representation of Central American dust barrier, suggesting that the parameterization of wet removal be explored in the model. Through a series of sensitivity studies, a better representation of the barrier was achieved when the wet removal of dust aerosols was treated as other hydrophilic aerosols. Analysis of the dust transport dynamics and loss processes suggest that while both mechanisms play a role in defining the dust transport barrier, loss processes by wet removal of dust are about twice as important as transport for July 2007. Perhaps more significant, the Central American dust barrier would not exist without removal by convective scavenging over the Caribbean, though this analysis should be extended for additional years to explore any inter-annual variability in the roles of transport and loss processes related to the barrier.

Finally, this work has made several contributions to the NASA GEOS modeling system. The NASA GEOS modeling system is now equipped to simulate dust emission using the DEAD scheme in addition to the native GOCART scheme. Additionally, this work will be used to update the current method of dust emission tuning. Rather than using a global tuning constant for all resolutions, this analysis will be used to homogenize dust emissions by determining tuning constants that are a function of both spatial resolution and source region. From the investigation of the Central American dust barrier, the wet removal of dust is now treated as other hydrophilic aerosols in order to capture observed dust transport downwind of the Saharan source region.

6.2 Future Work

Future work involved with exploring the dust aerosol lifecycle in the GEOS modeling system will continue on many fronts. First, a thorough evaluation of the GOCART-threshold emission parameterization is required. The GOCART-threshold setup exhibited intra-annual variability similar to DEAD emissions while using the more constrained 10-meter wind speed to parameterize dust emission similar to GOCART relative to soil-sized particles, extrapolated to 10 meters. However, dust distributions simulated by the GOCART-threshold simulation need to be evaluated in terms of observed dust distributions in order to evaluate its performance relative to the GOCART and DEAD schemes. Additionally, the effect of incorporating sub-grid wind variability in GOCART-threshold based emissions will be explored for coarse resolution simulations. Imposing a wind PDF in the GOCART-threshold formulation may impact

the timing of dust events in addition to the magnitude, as the driving wind speed and threshold speed are the same order of magnitude, which may act to initiate dust events that would not occur when using box-averaged wind speeds resolved by the model.

Continued efforts will also be made to further investigate the effects of model spatial resolution on the simulated dust aerosol lifecycle. Specifically, the analysis of Chapter 4.3 will be applied to different months and regions in order to gain a more complete understanding of the effects of resolution on the simulated dust distributions. From this analysis, tuning constants that are a function of both region and resolution will be determined to replace the current global and resolution independent tuning constant used in the NASA GEOS modeling system.

Next, the effect of driving meteorology on the simulated dust aerosol lifecycle will be explored by forcing the model with additional meteorological datasets, such as the European Center for Medium-Range Weather Forecasts (ECMWF) reanalyses. For this work, a set of simulations using the GOCART and DEAD emission schemes will be conducted to test the sensitivity of the results of Chapter 4.2 to the dynamical state provided by the reanalysis. This simulation may also be used to test the sensitivity of the role of dust transport toward the Central American dust barrier to driving meteorology. Also related to the Central American dust barrier, a long-term 0.5° resolution simulation will be analyzed to determine any inter-annual variability in the roles of transport and removal in establishing the Central American dust barrier.

Throughout this work, a constant it was suggested that sedimentation rates were too aggressive over the Saharan source region. This was particularly evident in GEOS-5 comparisons with MISR, where the gradient in AOT between the source region and

downwind was much greater in the model than observed. To explore sedimentation rates, several case studies of Saharan dust events identified by MODIS will be compared to CALIOP to evaluate the vertical placement, regional transport, and timing of dust plumes simulated by the 0.25° GEOS-5 operational 5-day forecasting system. Discrepancies (e.g., transport to the wrong altitude) will be used to construct sensitivity experiments where sedimentation rates will be explored over the Saharan source region.

Additionally, the effects of dust absorption on vertical dust distributions will be explored over the Saharan source region by varying the single scattering albedo of dust at visible wavelengths. Single scattering albedo is a measure of the contribution of scattering to the total extinction and can influence the local thermodynamics of the atmosphere. A more absorbing dust aerosol (smaller SSA) will increase the buoyancy of the surrounding air parcel and is favorable for lifting, thereby having implications for the lifetime and vertical distribution of the aerosol.

Bibliography

Abdou, W. A., D. J. Diner, J. V. Martonchik, C. J. Bruegge, R. A. Kahn, B. J. Gaitley, K. A. Crean, L. A. Remer, and B. Holben (2005), Comparison of coincident MISR and MODIS aerosol optical depths over land and ocean scenes containing AERONET sites, *J. Geophs. Res.*, *110*(D10), D02109, doi:10.1029/2008JD010754.

Adler, R. F., et al. (2003), The Version-2 Global Precipitation Climatology Project (GPCP) Monthly Precipitation Analysis (1979–Present). *J. Hydrometeor*, *4*, 1147–1167.

Alley, R., et al. (2007), *Climate Change 2007: The Physical Science Basis*, *Summary for Policymakers*, IPCC Secretariat, c/o WMO, 7bias, Avenue de la Paix, C. P. N ^{o} 2300, 1211 Geneva 2, Switzerland.

Anderson, R. S., and P. K. Haff (1988), Simulation of eolian saltation, *Science*, 241, 820 – 823.

Balkanski, Y. J., D. J. Jacob, G. M. Gardner, W. C. Graustein, and K. K. Turekian, 1993: Transport and residence times of tropospheric aerosols inferred from a global three-dimensional simulation of 210Ph. *J. Geophys. Res., 98***,** 20 573–20 586. *Res.,* **106,** 12 067–12 098.

Bloom, S., et al. (2005), Documentation and validation of the Goddard Earth Observing System (GEOS) data assimilation system – version 4, *Technical Report Series on Global Modeling and Data Assimilation*, *26*(104606).

Bonan, G. B., K. W. Oleson, M. Vertenstein, S. Levis, X. B. Zeng, Y. J. Dai, R. E Dickinson, and Z. L. Yang (2002), The land surface climatology of the

Community Land Model coupled to the NCAR Community Climate Model, *J. Clim.*, *15*, 3123-3149.

Bosilovich, M., (2008), NASA's Modern Era Retrospective-analysis for Research and Applications: Integrating Earth Observations, *Earthzine*, 26 September 2008.

Browell, E. V., W. B. Grant, and S. Ismail (2005), Airborne Lidar Systems, in *Laser Remote Sensing*, edited by Takashi Fujii and Tetsuo Fukuchi, 723-779, Taylor & Francis, NY.

Brown, R. A., *Fluid Mechanics of the Atmosphere*, Academic Press Inc., San Diego, CA.

Cakmur, R. V., et al. (2007), Constraining the magnitude of the global dust cycle by minimizing the difference between model and observations, *J. Geophys. Res.*, *111*(D6), D06207, doi: 10.1029/2005JD005791.

Cakmur, R. V., R. L. Miller, and O. Torres (2004), Incorporating the effect of small-scale circulations upon dust emission in an atmospheric general circulation *model, J. Geophys. Res., 109*, D07201, doi:10.1029/2003JD004067.

Carlson, T. N., and J. M. Prospero (1972), The large-scale movement of Saharan air outbreaks over the northern equatorial Atlantic, *J. Appl. Meteorol.*, *11*, 283-297.

Chen, G., et al. (2010), Observations of Saharan dust microphysical and optical properties from the eastern Atlantic during NAMMA airborne field campaign, *Atmos. Chem. Phys. Discuss.*, *10*, 13,445-13,493, doi:10.5194/acpd-10-13445-2010.

Chin, M., et al. (2002), Tropospheric aerosol optical thickness from the GOCART model and comparisons with satellite and sun photometer measurements, *J. Atmos. Sci.*, *59*(3), 461-483.

Chou, M.-D., and M. J. Suarez, A solar radiation parameterization for atmospheric studies, NASA/TM-1999-104606, vol. 15, NASA Goddard Space Flight Center, Greenbelt, Md., 1999.

Clarke, A. D., et al. (2004), Size distributions and mixtures of dust and black carbon aerosol in Asian outflow: Physiochemistry and optical properties, J. Geophys. Res., 109, D15S09, doi:10.1029/2003JD004378.

Clarke A., et al. (2007), Biomass burning and pollution aerosol over North America: Organic components and their influence on spectral optical properties and humidification response, *J. Geophys. Res.*, *112*(D12), D12S18, doi:10.1029/2006JD007777.

Colarco, P., A. da Silva, M. Chin, and T. Diehl (2010), Online simulations of global aerosol distributions in the NASA GEOS-4 model and comparisons to satellite and ground-based aerosol optical depth, *J. Geophys. Res.*, *115*, D14207, doi:10.1029/2009JD012820.

Colarco, P. R., O. B. Toon, and B. N. Holben (2003a), Saharan dust transport to the Caribbean during PRIDE: 1. Influence of dust sources and removal mechanisms on the timing and magnitude of downwind aerosol optical depth events from simulations of in situ and remote sensing observations, *J. Geophys. Res.*, *108*(D19), 8589, doi: 10.1029/2002JD002658.

Cook, K. H., (1999) Generation of the African Easterly jet and its role in determining West African precipitation. *J. Climate*, *12*, 1165-1184.

D'Almeida, G. A. (1987), On the variability of desert aerosol radiative characteristics, *J. Geophys. Res.*, *92*(D3), 3017-3026.

DeFries, R. S., and J. R. G. Townshend (1994), NDVI-Derived land-cover classifications at a global-scale, *International Journal of Remote Sensing*, *15*(17), 3567-3586.

DeMott, P. J., K. Sassen, M. R. Poellot, D. Baumgardner, D. C. Rogers, S. D. Brooks, A. J. Prenni, and S. M. Kreidenweis (2003), African dust aerosols as atmospheric ice nuclei, *Geophys. Res. Lett.*, *30*(14), 1732, doi:10.1029/2003GL017410.

Desboeufs, K.V., R. Losno, and J. Colin (2001), Factors influencing aerosol solubility during cloud processes, *Atmos. Environ.*, *35*, 3529-3527, doi:10.1016/S1352-2310(00)00472-6.

Diner, D. J., et al. (1998), Multi-angle Imaging SpectroRadiometer (MISR) – Instrument description and experiment overview, *IEEE Trans. Geosci. Remote Sens.*, *36*(4), 1072-1087, doi:10.1109/36.700992.

Dubovik, O., and M. D. King (2000), A flexible inversion algorithm for retrieval of aerosol optical properties from sun and sky radiance measurements, *J. Geophys. Res.*, *105*(D16), 20673-20696.

Dubovik, O., et al. (2002), Variability in absorption and optical properties of key aerosol types observed in worldwide locations. *J. Atmos. Sci., 59*, 590-608, doi:10.1175/1520-0469(2002)059<0590:VOAAOP>2.0.CO;2.

Duce, R. A., N. W. Tindale, Atmospheric transport of iron and its deposition in the ocean, *Limnol. Oceanogr.*, *36*, 1715–1726, 1991.

Dunion, J. P., and C. S. Velden (2004), The impact of the Saharan air layer on Atlantic tropical cyclone activity, *Bull. Am. Meteorol. Soc.*, *85*(3), 353 – 365.

Falkowski, P. G., R. T. Barber, and V. Smetacek (1998), Biogeochemical controls and feedbacks on primary production, *Science*, *281*, 200-206.

Fe´can, F., B. Marticorena, and G. Bergametti (1999), Parameterization of the increase of the aeolian erosion threshold wind friction velocity due to soil moisture for arid and semi-arid areas, *Ann. Geophys.*, *17*(1), 149-157.

Ferrare, R. A., et al. (2000a), Comparison of aerosol optical properties and water vapor among ground and airborne lidars and sun photometers during TARFOX, *J. Geophys. Res.*, *105*(D8), 9917-9933.

Ferrare, R. A., et al. (2000b), Comparison of LASE, aircraft, and satellite measurements of aerosol optical properties and water vapor during TARFOX, *J. Geophys. Res.*, *105*(D8), 9935-9947.

Gillette, D. A., B. Marticorena, and G. Bergametti (1998), Change in the aerodynamic roughness height by saltating grains: Experiments assessment, test of theory, and operational parameterization, *J. Geophys. Res.*, *103*(D6), 6203-6209.

Gillette, D. A., and R. Passi, Modeling dust emission caused by wind erosion, *J. Geophys. Res.*, *93*(D11), 14,233–14,242, 1988.

Ginoux, P., M. Chin, I. Tegen, J. M. Prospero, B. Holben, O. Dubovik, and S.-J. Lin (2001), Sources and distributions of dust aerosols simulated with the GOCART model, *J. Geophys. Res.*, *106*(D17), 20255-20273.

Gomes, L., G. Bergametti, G. Coud´e-Gaussen, and P. Rognon (1990), Submicron desert dusts: A sandblasting process, *J. Geophys. Res.*, *95*(D9), 13927-13935.

Greeley, R., and J. D. Iversen (1985), Wind as a Geological Process on Earth, Mars, Venus, and Titan, Cambridge Univ. Press, New York.

Grini, A., C. S. Zender (2004), Roles of saltation, sandblasting, and wind speed variability on mineral dust aerosol size distribution during the Puerto Rican Dust

Experiment (PRIDE), *J. Geophys. Res.*, *109*(D7), D07202, doi: 10.1029/2003JD004233.

Grini, A., G. Myhre, C. S. Zender, and I. S. A. Isaksen (2005), Model simulations of dust sources and transport in the global atmosphere: Effects of soil erodibility and wind speed variability, *J. Geophys. Res., 110*, D02205, doi:10.1029/2004JD005037.

Haywood, J., P. Francis, S. Osborne, M. Glew, N. Loeb, E. Highwood, D. Tanré, G. Myhre, P. Formenti, and E. Hirst (2003), Radiative properties and direct radiative effect of Saharan dust measured by the C-130 aircraft during SHADE: 1. Solar spectrum, *J. Geophys. Res*., *108*(D18), 8577, doi:10.1029/2002JD002687.

Hand, J., N. Mahowald, Y. Chen, R. Siefert, C. Lou, A. Subramaniam, and I. Fung (2004), Estimates of soluble iron from observations and a global mineral aerosol model: Biogeochemical implications, *J. Geophys. Res.*, *109*, D17205, doi:10.1029/2004JD004574.

Hill, C., C. DeLuca, V. Balaji, M. Suarez, A. da Silva, and the ESMF Joint Specification Team (2004), The Architecture of the Earth System Modeling Framework, *Computing in Sci. and Eng.*, *6*, 1-6.

Hillel, D. (1982), *Introduction to Soil Physics*, Academic, San Diego, California, USA.

Holben, B. N., et al. (2001), An emerging ground-based aerosol climatology: Aerosol optical depth from AERONET, *J. Geophys. Res.*, *106*(D11), 12067-12097.

Huebert, B. J., et al. (2004). PELTI: Measuring the Passing Efficiency of an Airborne Low Turbulence Aerosol Inlet, *Aerosol Sci. Technol.* 38, 803–826, doi:10.1080/027868290500823.

Huffman, G. J., R. F. Adler, M. Morrissey, D. Bolvin, S.Curtis, R. Joyce, B. McGavock,

and J.Susskind (2001), Global Precipitation at One-Degree Daily Resolution from Multisatellite Observations. *J. Hydrometeor*, *2*, 36–50.

Huneeus, N., et al. (2010), Global dust model intercomparison in AeroCom phase 1, *Atmos. Chem. Phys.*, *10*, 23781-23864, doi:10.5194/acpd-10-23781-2010.

Ismail, S., et al. (2008), LASE measurements of water vapor, aerosol, and cloud distributions in Saharan air layers and tropical disturbances, *Proce. 24th Int. Laser Radar Conf*., Boulder, CO, July 21-26.

Ismail, S. et al. (2009), LASE measurements of water vapor, aerosol, and cloud distributions in Saharan air layers and tropical disturbances (submitted to *J. Atmos. Sci.*).

Ivesen, J. D., and B. R. White (1982), Saltation threshold on Earth, Mars, and Venus, *Sedimentology*, *29*(1), 111-119.

Jickells, T. D., et al. (2005), Global iron connections between deseret dust, ocean biogeochemistry, and climate, *Science*, *308*(5718), 67-71.

Justus, C., W. Hargraves, A. Mikhail, and D. Graber (1978), Methods for estimating wind speed frequency distributions, *J. Appl. Meteorol.*, *17*, 350 – 353.

Kahn, R., et al. (2005), MISR calibration and implications for low-light-level aerosol retrieval over dark water, *J. Atmos. Sci.*, *62*(4), 1032-1052.

Karyampudi, V. M., et al. (1999), Validation of the Saharan dust plume conceptual model using lidar, Meteosat, and ECMWF data, *Bull. Am. Meteorol. Soc.*, *80*, 1045-1075.

Kaufman, Y. J., I. Koren, L. A. Remer, D. Tanré, P. Ginoux, and S. Fan (2005), Dust transport and deposition observed from the Terra-Moderate Resolution Imaging

Spectroradiometer (MODIS) spacecraft over the Atlantic Ocean, *J. Geophys. Res.*, *110*, D10S12, doi:10.1029/2003JD004436.

Kieber, R. J., J. D. Willey, and G. B. Avery Jr. (2003), Temporal variability of rainwater iron speciation at the Bermuda Atlantic Time Series Station, *J. Geophys. Res.*, *108*(C8), 3277, doi:10.1029/2001JC001031.

Kiehl, J. T., J. J. Hack, G. B. Bonan, B. A. Boville, B. P. Briegleb, D. L. Williamson, and P. J. Rasch, Description of the NCAR Community Climate Model (CCM3), *NCAR Tech. Note NCAR/TN-420+STR*, 152 pp., Natl. Cent. for Atmos. Res., Boulder, CO., 1996.

Kok, J. F. (2011), A scaling theory for the size distribution of emitted dust aerosols suggests climate models underestimate the size of the global dust cycle, *Proceedings of the National Academy of Sciences (PNAS)*, *108*(3), 1016-1021, doi:10.1073/pnas.1014798108.

Köpke, P., M. Hess, I. Schult, and E. P. Shettle (1997), The Global Aerosol Data Set (GADS), *MPI-Rep., 243*, 44 pp., Max-Planck-Inst., Hamburg, Germany.

Koretsky, C., D. Sverjensky, J. Salisbury, and D. D'Aria (1997), Detection of surface hydroxyl species on quartz, gamm-alumina, and feldspar using diffuse reflectance infrared spectroscopy, *Geochim. Cosmochim. Acta*, *61*, 2193-2210.

Kumar, P., A. Nenes, and I. N. Sokolik (2009), The importance of absorption for CCN activity and hygroscopic properties of mineral dust aerosols, *Geophys. Res. Lett.*, *36*, L24804, doi:10.1029/2009GL040827.

Lau, W. K.M., and K.-M. Kim (2007), How Nature Foiled the 2006 Hurricane Forecasts, *Eos Trans. AGU*, *88*(9), doi:10.1029/2007EO090002.

Levy, R. C., L. A. Remer, R. G. Kleidman, S. Mattoo, C. Ichoku, R. Kahn, and T. F. Eck, (2010), Global evaluation of the Collection 5 MODIS dark-target aerosol products over land, *Atmos. Chem. Phys*., *10*, 10399-10420, doi:10.5194/acp-10-10399-2010.

Li, C., et al. (2010), Anthropogenic air pollution observed near dust source regions in northwestern China during springtime 2008, J. Geophys. Res., 115, D00K22, doi:10.1029/2009JD013659.

Li, Z., et al. (2007), Preface to special section on East Asian Studies of Tropospheric Aerosols: An International Regional Experiment (EAST-AIRE), J. Geophys. Res., 112, D22S00, doi:10.1029/2007JD008853.

Lin, S.-J. (2004), A vertically Lagrangian finite-volume dynamical core for global models, *Mon. Weather Rev.*, *132*, 2293-2307.

Luo, C., N. M. Mahowald, J. del Corral (2003), Sensitivity study of meteorological parameters on mineral aerosol mobilization, transport, and distribution, *J. Geophys. Res.*, *108*(D15), 4447, doi: 10.1029/2003JD003483.

Mahowald, N. M., A. R. Baker, G. Bergametti, N. Brooks, R. A. Duce, T. D. Jickells, N. Kubilay, J. M. Prospero, and I. Tegen (2005), Atmospheric global dust cycle and iron inputs to the ocean, *Global Biogeochem. Cycles*, *19*, GB4025, doi:10.1029/2004GB002402.

Mahowald, N. M., K. Kohfeld, M. Hansson, Y. Balkanski, S. P. Harrison, I. C. Prentice, M. Schulz, and H. Rodhe (1999), Dust sources and deposition during the Last Glacial Maximum and current climate: A comparison of model results with paleodata from ice cores and marine sediments, *J. Geophys. Res., 104*(D13), 15,895-15,916, doi:10.1029/1999JD900084.

Mahowald, N. M., and C. Luo (2003), A less dusty future? *Geophys. Res. Lett., 30*(17), 1903, doi:10.1029/2002JD002775.

Marticorena, B., and G. Bergametti (1995), Modeling the atmospheric dust cycle. 1. Design of a soil-derived dust emission scheme, *J. Geophys. Res.*, *100*(D8), 16415-16430.

McGill, M. J., D. L. Hlavka, W. D. Hart, V. S. Scott, J. D. Spinhirne, and B. Schmid (2002), The cloud physics lidar: Instrument description and initial measurement results, *Appl. Opt.*, *41*, 3725 – 3734.

McGill, M. J., D. L. Hlavka, W. D. Hart, E. J. Welton, and J. R. Campbell (2003), Airborne lidar measurements of aerosol optical properties during SAFARI-2000, *J. Geophys. Res.*, *108*(D13), 8493, doi:10.1029/2002JD002370.

McGill, M. J., L. Li, W. D. Hart, G. M. Heymsfield, D. L. Hlavka, P. E. Racette, L. Tian, M. A. Vaughan, and D. M. Winker (2004), Combined lidar-radar remote sensing: Initial results from CRYSTAL-FACE, *J. Geophys. Res.*, *109*, D07203, doi:10.1029/2003JD004030.

McNaughton, C. S., et al. (2007), Results from the DC-8 Inlet Characterization Experiment (DICE): Airborne versus surface sampling of mineral dust and sea salt aerosols, *Aerosol Science and Techonology*, *41*(2), 136, doi:10.1080/02786820601118406.

Miller, R. L., I. Tegen, and J. Perlwitz (2004), Surface radiative forcing of soil dust aerosols and the hydrologic cycle, *J. Geophys. Res.*, *109*, D04203, doi:10.1029/2003JD004085.

Moorthi, S., and M. J. Suarez (1992), Relaxed Arakawa-Schubert: A parameterization of

moist convection for general circulation models, *Mon. Wea. Rev., 120*, 978-1002.

Nowottnick, E., P. Colarco, R. Ferrare, G. Chen, S. Ismail, B. Anderson, and E. Browell (2010), Online simulations of mineral dust aerosol distributions: Comparison to NAMMA observations and sensitivity to dust emission parameterization, *J. Geophys. Res.*, *115*, D03202, doi:10.1029/2009JD012692.

Petit, R. H., M. Legrand, I. Jankowiak, J. Molinié, C. Asselin de Beauville, G. Marion, and J. L. Mansot (2005), Transport of Saharan dust over the Caribbean Islands: Study of an event, *J. Geophys. Res.*, *110*, D18S09, doi:10.1029/2004JD004748.

Pfister, L., H. B. Selkirk, D. O. Starr, K. Rosenlof, and P. A. Newman (2010), A meteorological overview of the TC4 mission, *J. Geophys. Res.*, *115*, D00J12, doi:10.1029/2009JD013316.

Prospero, J. M., P. Ginoux, O. Torres, S. E. Nicholson, and T. E. Gill (2002), Environmental characterization of global sources of atmospheric soil dust identified with the Nimbus 7 Total Ozone Mapping Spectrometer (TOMS) absorbing aerosol product, *Reviews of Geophysics*, *40*(1), 1002, doi:10.1029/2000RG000095.

Prospero, J., and P. Lamb (2003), African droughts and dust transport to the Caribbean: climate change implications, *Science*, *302*, 1024 – 1027.

Putman, W., and L. Shian-Jiann, 2007: Finite-volume transport on various cubed-sphere grids. *J. Comput. Phys.*, 227, 55–78.

Rienecker, M. M., et al., 2008:The GEOS- 5 Data Assimilation System -Documentation of Versions 5.0.1, 5.1.0, and 5.2.0. *Technical Report Series on Global Modeling and Data Assimilation 104606*, *27*.

Remer, L. A., et al. (2005), The MODIS aerosol algorithm, products, and validation, *J. Atmos. Sci.*, *62*(4), 947-973.

Rosenfeld, D., Y. Rudich, and R. Lahav (2001), Desert dust suppressing precipication: A possible desertification loop, *Proceedings of the National Academy of Sciences*, *98*(11), 5975-5980.

Shao, Y., M. R. Raupach (1993), Effect of saltation bombardment on the entrainment of dust by wind, *J. Geophys. Res.*, *98*(D7), 12719-12726.

Smirnov, A, B. N. Holben, T. F. Eck, O. Dubovik, and I. Slutsker (2000), Cloud-screening and quality control algorithms for the AERONET database, *Remote Sens. Environ.*, *73*(3), 337-349.

Sokolik, I. N., and O. B. Toon (1996), Direct radiative forcing by anthropogenic airborne mineral aerosols, *Nature*, *381*(6584), 681-683.

Su, L., and O. B. Toon (2009), Numerical simulations of Asian dust storms using a coupled climate-aerosol microphysical model, *J. Geophys. Res., 114*, D14202, doi:10.1029/2008JD010956.

Tegen, I., and I. Fung (1994), Modeling of mineral dust in the atmospherere-sources, transport, and optical-thickness, *J. Geophys. Res.*, *99*(D11), 22897-22914.

Tegen, I., and A. A. Lacis (1996), Modeling of particle size distribution and its influence on the radiative properties of mineral dust aerosol, *J. Geophys. Res.*, *101*(D14), 19237-19244.

Tegen, I., and R. Miller (1998), A general circulation model study on the interannual variability of soil dust aerosol, *J. Geophys. Res.*, *103*(D20), 25975-25995.

Textor et al., (2006), Analysis and quantification of the diversities of aerosol life cycles

with AeroCom, *Atmos. Chem. Phys., 6*, 1777-1813.

Toon, O. B., et al. (2010), Planning, implementation, and first results of the Tropical Composition, Cloud and Climate Coupling Experiment (TC4), *J. Geophys. Res.*, *115*, D00J04, doi:10.1029/2009JD013073.

Torres, O., A. Tanskanen, B. Veihelmann, C. Ahn, R. Braak, P. K. Bhartia, P. Veefkind, and P. Levelt (2007), Aerosols and surface UV products from Ozone Monitoring Instrument observations: An overview, *J. Geophys. Res.*, *112*(D24), D24S47, doi:10.1029/2007JD008809.

Twohy, C. H., et al. (2009), Saharan dust particles nucleate droplets in eastern Atlantic clouds, *Geophys. Res. Lett., 36*, L01807, doi:10.1029/2008GL035846.

Vaughan, M. A. , S. Young, D. Winker, K. Powell, A. Omar, Z. Liu, Y. Hu, and C. Hostetler (2005), Fully automated analysis of space-based lidar data: An overview of the CALIPSO retrieval algorithms and data products, *Proc. SPIE Int. Soc. Opt. Eng.*, *5575*, 16-30.

Wong, S., A. E. Dessler, N. M. Mahowald, P. Yang, and Q. Feng (2009), Maintenance of lower tropospheric temperature inversion in the Saharan air layer by dust and dry anomaly, *J. Clim.*, in press.

Yoshioka, M., N. M. Mahowald, A. J. Conley, W. D. Collins, D. W. Fillmore, C. S. Zender, and D. B. Coleman (2007), Impact of desert dust radiative forcing on Sahel precipitation: Relative importance of dust compared to sea surface temperature variations, vegetation changes, and greenhouse gas warming, *J. Clim.*, *20*(8), 1445-1467.

Yu, T. R. (1997). Chemistry of Variable Charge Soils. Oxford University Press, New

York.

Zender, C. S., H. S. Bian, and D. Newman (2003), Mineral Dust Entrainment and Deposition (DEAD) model: Description and 1990s dust climatology, *J. Geophys. Res.*, *108*(D14), 4416, doi:10.1029/2002JD002775

Zender, C. S., R. Miller, and I. Tegen (2004), Quantifying mineral dust mass budgets: Terminology, constraints, and current estimates, *Eos Trans. AGU*, *85*(48), 509-512.

Zhu, X. R., J. M. Prospero, and F. J. Millero (1997), Diel variability of soluble Fe(II) and soluble total Fe in North African dust in the trade winds at Barbados, *J. Geophys. Res.*, *102*(D17), 21,297–21,305, doi:10.1029/97JD01313.

Zhu, A., V. Ramanathan, F. Li, and D. Kim (2007), Dust plumes over the Pacific, Indian, and Atlantic oceans: Climatology and radiative impact, *J. Geophys. Res.*, *112*(D16), D16208, doi:10.1029/2007JD008427.